Imperial College London

Peptide Mediated Nanoparticle Assembly investigated using Small Angle X-ray Scattering

Piotr Gryko

Thesis submitted for degree of

Doctor of Philosophy

Supervisors:
Dr Mary Ryan
Professor Molly Stevens

Department of Materials

Imperial College London

12th March 2012

Piotr Gryko: *Peptide Mediated Nanoparticle Assembly investigated using Small Angle X-ray Scattering,* Doctor of Philosophy, 12th March 2012

A good traveler has no fixed plans
and is not intent on arriving

— Lao Tzu

To *love* is to recognize yourself in another

— Eckhart Tolle

ABSTRACT

Nanoparticle systems arranged through bio-chemical self-assembly mechanisms display novel electronic and optical characteristics applicable to biosensing, tissue engineering, therapeutics and drug delivery. Metallic Nanoparticles such as those composed of gold or CdSe are expected to replace standard chemical fluorophore due to their high optical scattering cross-section. The colloidal nature of nanoparticles necessitates the engineering of NPs surface chemistry to control particle stability and assembly order. The high intensity of modern synchrotron sources, combined with the high electron density contrast of metallic NPs, allows for fast, sensitive, in-situ synchrotron measurements. Here Small Angle X-ray scattering is used to observe nanoscale structural changes and relate them to changes in polypeptide mediated interaction potential, particle surface charge and mobility within aggregates. These results enable strategies for optimising the structure and the optical characteristics of NP assemblies, which are vital for their performance as colourimetric sensors. Here three NP systems are investigated and characterised:

(1) Gold nanoparticles assembled using de novo designed polypeptides developed by D. Aili (Chapter 3). The assembly is achieved by the folding dependent bridging of the particles induced by the heteroassociation of immobilised helix-loop-helix polypeptides and a complementary non-linear polypeptide found in solution. Changes in the optical properties of the assembly as a function of particle size and linker concentration are observed, with SAXS used to obtain in-situ structural information on the aggregates. The particles are found to assemble into highly ordered close packed structures with an interparticle spacing of 4.8±0.4nm, corresponding to the length of a folded polypeptide. Changes in particle ordering, aggregation dynamics and mass fractal dimension are observed as a function of linker concentration and particle size. These transitions are related to changes in linker mediated interaction potential, particle surface charge and mobility within the aggregates.

(2) Interaction of BSA with AuNP aggregates (Chapter 4). Bovine serum albumin (BSA) is a vital component of standard immunological assays and it is often extended for use in de-novo assays based on peptide modified metallic nanoparticles. Whilst a wide range of plasma proteins such as BSA and HSA have been shown to associate with nanoparticles, there is little work done on the effect of BSA on NP assemblies, which are highly dependent on particle stability. Here the effect of BSA on AuNP aggregates is characterised, using stability assays, DLS, UV-VIS and SAXS. Far from being an inert component, the introduction of BSA directly alters the structure and interaction of AuNP aggregates. Temperature is observed to be a factor in these interactions with a specific affinity for hydrophobic systems.

(3) A Quantum Dot - Gold Nanoparticle conjugate assay for the detection of urokinase plasminogen activator (uPA) (Chapter 5). Proteolytic enzymes are used as disease biomarkers for several forms of cancer. The surface assembly of gold nanoparticles onto the surface of quantum dots is demonstrated, with the growth in conjugate size

May you live in interesting times
-Ancient Chinese proverb

characterised using in-situ SAXS. Complete conjugate disassembly is observed upon the addition of the enzyme uPA, however QDs luminescence does not fully recover. This indicates that other effects may result in the permanent quenching of quantum dots.

The work presented here is designed to guide in the synthesis of general principles for assembly of NPs by biomolecular mediated bridging, whilst contributing to the fundamental understanding of the assembly process.

PUBLICATIONS

The work described in Chapter 3 has been published in Nanoletters:

Polypeptide Folding-Mediated Tuning of the Optical and Structural Properties of Gold Nanoparticle Assemblies - D Aili, P Gryko, B Sepulveda, J Dick, N Kirby, Richard Heenan, Lars Baltzer, Bo Liedberg, Mary P. Ryan and Molly M. Stevens - Nano Letters, 2011 - ACS Publications

The work presented in later chapters is currently (as of submission) in the process of being prepared for publishing in research journals.

Accept the fact that nothing is certain and no law is fixed,
be as fluid and formless as water,
never bet on stability or lasting order.
Everything changes.

— Robert Greene [71]

ACKNOWLEDGMENTS

I am extremely grateful for the extensive support and cheerful enthusiasm of Dr Mary Ryan during the past four years. Without your support I would have dropped out of the PhD; it has been an honour to work with you. I would like to thank Imperial College and Professor Molly Stevens for the support and opportunity to study for a PhD and the EPSRC for funding. The multidisciplinary biochemistry aspects of my work were based on the experimental systems developed by Dr Daniel Aili and Mr John Dick. Much of this thesis came from collaborative work with them and I am grateful of their support.

The opportunity to travel during my PhD provided experiences for personal growth and was immensely enriching. I would like to thank the Japanese Society for the promotion of science (JSPS) for the opportunity to travel to Japan and Dr Tamotsu Zako and Prof Maeda for their hospitality and excellent scientific support at the Riken Institute (Tokyo).

All of the synchrotron measurements in this thesis were possible due to the high performance SAXS/WAXS beamline at the Australian synchrotron. The beamline scientists provided outstanding support, often working into the early hours of the morning. Without their help this thesis could not have been written.

I would like to thank Prof Ian Robinson for his extensive supervision during my masters project and summer research internship. Your support encouraged me to pursue a PhD.

My close family and friends have provided kind support over these years; thank you Kristina for your patience and love.

Finally I would like to thank my parents for their strength, love and support over the decades. My achievements have grown out of your strengths.

CONTENTS

1 LITERATURE REVIEW 1
- 1.1 The material society 1
- 1.2 The promise of the nanoscale 1
  - 1.2.1 The medical need 2
  - 1.2.2 Characteristics of the nano dimension 3
  - 1.2.3 Quantum dots (QDs) 3
  - 1.2.4 Gold nanoparticles (AuNPs) 5
- 1.3 Nanoparticle surface - shaping the interface 6
  - 1.3.1 Surface functionalisation as a necessity for colloidal control 6
  - 1.3.2 The bio-nano interface 8
  - 1.3.3 Biomolecular mediated nanomaterial assembly 8
  - 1.3.4 Crosslinking and non-crosslinking approaches to programable nanoparticle assembly 9
  - 1.3.5 Nanoparticle assembly structure 11
- 1.4 Scope of Thesis 13

2 EXPERIMENTAL METHODS 15
- 2.1 Measuring at the nanoscale 15
- 2.2 Dynamic Light Scattering (DLS) and Zeta potential (ZP) 16
  - 2.2.1 Dynamic Light Scattering 16
  - 2.2.2 Zeta potential measurements (ZP) 17
- 2.3 Ultraviolet–Visible Absorption Spectroscopy (UV-VIS) 18
  - 2.3.1 Surface Plasmon Resonance 19
  - 2.3.2 Concentration Estimation (Beer-Lambert Law) 22
  - 2.3.3 Quantification of aggregation 23
- 2.4 Transmission Electron Microscopy (TEM) 25
- 2.5 Small Angle X-ray Scattering (SAXS) 26
  - 2.5.1 The Fourier relation of structure to scattered X-ray intensity 28
  - 2.5.2 Experimental setup at the Australian synchrotron 29
  - 2.5.3 Scattering from a colloidal system 30
  - 2.5.4 Guinier and Porod fits 31
  - 2.5.5 Kratky 34
  - 2.5.6 Pair distribution function 34
  - 2.5.7 Scattering from polydisperse populations of particles 35
  - 2.5.8 Structure factor S(q) 39
  - 2.5.9 Structure factor models 40

3 POLYPEPTIDE FOLDING-MEDIATED NANOPARTICLE ASSEMBLY 45
- 3.1 Introduction 45
- 3.2 Polypeptide mediated assembly of AuNPs 46
  - 3.2.1 Materials and methods 46
  - 3.2.2 Characterisation of particle size and concentration 47
  - 3.2.3 Characterisation of synthetic polypeptides using SAXS 48
- 3.3 Optical characterisation 50
- 3.4 Synchrotron characterisation 53

3.5 Discussion 58
3.6 Conclusion 60
3.6.1 Possible future work 61
3.7 Chapter Appendix 62
3.7.1 UV-VIS spectra 63
3.7.2 SAXS data 64
4 INTERACTION OF GOLD NANOPARTICLE AGGREGATES WITH BSA 67
4.1 Introduction 67
4.1.1 Role and structure of BSA 67
4.1.2 Rationale for work 68
4.2 Materials and methods 71
4.2.1 Characterisation using TEM, UV-VIS, DLS and SAXS 71
4.2.2 Sample preparation protocols 71
4.3 Association of BSA onto AuNP surface 72
4.3.1 Characterisation of BSA 72
4.3.2 Dynamic light scattering of BSA adsorption 73
4.4 Stability of AuNPs to salt concentration 74
4.4.1 UV-VIS measurements 74
4.4.2 SAXS measurements 76
4.5 Effect of BSA on AuNP stability 78
4.5.1 UV-VIS measurements 78
4.5.2 SAXS measurements 79
4.6 Conclusion 80
5 PEPTIDE MEDIATED ASSEMBLY AND ENZYME TRIGGERED DISPERSION OF A COMPOSITE QUANTUM DOT GOLD NANOPARTICLE SYSTEM 83
5.1 Introduction 83
5.1.1 Optical properties of quantum dots 84
5.1.2 Quenching of quantum dots by proximal AuNPs 85
5.2 Materials and synthesis 86
5.2.1 Peptide synthesis 86
5.2.2 Quantum dot phase transfer from organic to aqueous solvent 86
5.2.3 Gold nanoparticle peptide conjugation 87
5.2.4 Quantum dot conjugation with Pep-Au 87
5.2.5 Enzymatic dispersion of conjugates 87
5.2.6 Inhibitor control 88
5.2.7 Imidazole induced conjugate dispersion 88
5.2.8 High Resolution TEM 88
5.2.9 SAXS at the Australian Synchrotron 88
5.3 Characterisation of stock materials 88
5.3.1 Quantum dots 89
5.3.2 Peptide-AuNP 91
5.3.3 Non-interacting mixtures of QDs and Pep-Au 92
5.3.4 Characterization of Urokinase Plasminogen Activator 94
5.4 Peptide mediated assembly of QDs-Pep-Au conjugates 94
5.4.1 Choice of Conjugate model 95
5.4.2 Conjugate assembly at constant QD concentration 97
5.4.3 Conjugate assembly constant Peptide-AuNP concentration 98

5.4.4 Optical characterisation 99
5.4.5 Langmuir adsorption 99
5.5 Enzymatic dispersion of Pep-Au/QD conjugates 102
5.6 Control measurements 103
5.6.1 Imidazole dispersion 104
5.6.2 Pep-Au with control substrate peptide 104
5.6.3 QDs with substrate peptide 105
5.6.4 Mixture of pre-cleaved Peptide-AuNP with QDs 105
5.7 Conclusion 105
5.8 Chapter Appendix 106
5.8.1 Characterisation of CdSe/ZnS QDs by Dabbousi et al 106
5.8.2 Conjugate assembly fits 106
5.8.3 Conjugate disassembly fits 107
6 SUMMARY 113
6.1 Summary of work 113

BIBLIOGRAPHY 115

LIST OF FIGURES

Figure 1 Relative dimensions of structures found in nature 2
Figure 2 Emission spectra of CdSe/ZnS QDs 4
Figure 3 UV-VIS extinction spectra for 20nm AuNPs in a) disperse b) aggregated states 5
Figure 4 Schematic representation of colloidal stabilisation 7
Figure 5 Schematic illustration of AuNP assembly using de novo designed polypeptides 11
Figure 6 Projections of 3D NP clusters generated using off-lattice aggregation models 12
Figure 7 Accessible size ranges of different scattering techniques 15
Figure 8 Schematic representation of zeta potential 18
Figure 9 20nm AuNPs synthesised via citrate reduction of gold chloride 19
Figure 10 Schematic illustration of localised surface plasmon resonance 20
Figure 11 UV-vis absorption spectra of AuNPs with diameters of 9, 22, 48, and 99nm dispersed in water 21
Figure 12 Schematic illustration of near field coupling between metallic NPs in two different polarisations. Diagram redrawn from [146]. 22
Figure 13 Logarithm of extinction coefficients vs logarithm of nanoparticle core diameter 22
Figure 14 Schematic illustration of the A/D ratio and the influence of particle aggregation on the A/D ratio. 23
Figure 15 Illustration of A/D integration regions for 10nm, 20nm and 40nm AuNPs 24
Figure 16 Salt stability assays of 10nm AuNPs functionalized with a) citrate b) BSPP c) BSPP Fmoc-GFC. The UV-VIS absorption spectra are recorded as a function of solution NaCl concentration. 25
Figure 17 Comparison of A/D ratio with absorbance at point 25
Figure 18 Comparison of particle diameters obtained using TEM and SAXS 26
Figure 19 Essential components of a Small Angle X-ray Scattering system 27
Figure 20 Schematic representation of momentum transfer vector $\bar{q}$ 27
Figure 21 Representation of photons scattered into solid angle $d\Omega$ for scattering angle θ. Image redrawn from [77]. 28
Figure 22 Experimental facilities at the Australian SAXS/WAXS beamline 30

Figure 23 Reduction of SAXS data using beamline software 30
Figure 24 Importance of accurate background subtraction for SAXS data 31
Figure 25 Example of Porod fit applied to scattering of aggregate formed from 20nm AuNP 32
Figure 26 Illustration of mass and surface fractals 33
Figure 27 Structures of RLCA, DLCA and CC aggregates 33
Figure 28 Application of Kratky plot to protein samples 34
Figure 29 Illustration of pair distribution function P(r) for different geometrical shapes 35
Figure 30 SAXS profile of AuNPs fitted with a spherical form factor 37
Figure 31 Schematic representation of core-shell model 38
Figure 32 Effect of AuNP assembly on scattering pattern 39
Figure 33 Structure factors S(q) of 18.4nm AuNP aggregates 40
Figure 34 Illustration of direct and indirect inter-particle correlations 41
Figure 35 Square well potential used for Baxters sticky hard sphere model 43
Figure 36 Schematic representation of AuNP assembly with de novo designed polypeptides 45
Figure 37 TEM Images of AuNPs 47
Figure 38 SAXS profiles from AuNPs fitted using a spherical form factor 48
Figure 39 SAXS profiles of 0.5mM JR2EC2 and $JR2KC_2$ 49
Figure 40 Kratky plots and Pair distribution function of $JR2EC_2$ and $JR2KC_2$ 49
Figure 41 Illustration of fiber formation from polypeptides $JR2EC_2$ and $JR2KC_2$ 50
Figure 42 SAXS scattering patterns from fibers formed from $JR2EC_2$ and $JR2KC_2$ 51
Figure 43 UV-VIS spectrum of JR2EC coated AuNPs upon addition of 0.1uM $JR2KC_2$ 51
Figure 44 Optical characterisation of $JR2EC_2$ coated AuNPs, upon addition of $JR2KC_2$ 52
Figure 45 Effect of aggregation on SAXS patterns of $JR2EC_2$ functionalised AuNPs 54
Figure 46 Structure factors of JR2EC2 coated AuNPs 55
Figure 47 Structure factor of AuNPs, with the q axis scaled to q_0/q_n 56
Figure 48 Fractal dimension of AuNPs Particles of 9.4nm (red), 18.3nm (blue) and 37.8nm (black) in diameter 56
Figure 49 Square Well Potential and Sticky Hard Sphere models applied to AuNPs structure factors 57
Figure 50 Sticky hard sphere model applied to structure factors of JR2EC modified AuNPs 58
Figure 51 Schematic illustration of proposed assembly structure 60
Figure 52 Schematic illustration of hybrid nanoparticle liposome detection of phospholipase assay 62

Figure 53 Scattering profiles of liposomes with and without JR2KC$_2$ 62
Figure 54 UV-VIS spectra of 9.4nm AuNPs 63
Figure 55 UV-VIS spectra of 18.3nm AuNPs 63
Figure 56 UV-VIS spectra of 37.8nm AuNPs 64
Figure 57 Scattered intensities of JR2EC$_2$ modified Au NPs, 15min after addition of JR2KC$_2$. Particle diameters of 9.4nm, 18.3nm and 37.8 nm were used. 64
Figure 58 Structure factors of 9.4nm, 18.3nm and 37.8 nm AuNPs. 65
Figure 59 Structure of BSA under normal conformation, fast conformation, and extended structure 68
Figure 60 Schematic demonstrating control of biomolecular conformation and orientation by NP surface curvature 69
Figure 61 Functionalisation pathways for AuNPs 72
Figure 62 SAXS of 1mg/ml BSA in nanopure water 73
Figure 63 Dynamic light scattering measurements of citrate stabilised AuNPs incubated with BSA 74
Figure 64 Salt stability of AuNPs as a function of ligand concentration and particle size. 75
Figure 65 Salt stability assays of citrate coated AuNPs and citrate Fmoc-GFC coated AuNPs 76
Figure 66 SAXS profiles from AuNPs fitted using a spherical form factor 76
Figure 67 SAXS profiles and extracted structure factors for AuNP aggregates formed from particles with different capping ligands 77
Figure 68 Comparison of SAXS from aggregates formed from citrate and citrate Fmoc-GFC coated AuNPs 78
Figure 69 Salt stability assay performed on AuNP BSA conjugates, for AuNPs with diameters of 9.9nm and 20.3nm. 79
Figure 70 Effect of BSA concentration on aggregates formed from 9.9nm AuNPs 80
Figure 71 SAXS measurements of 8.9nm AuNP aggregates. The particles are incubated with and without 0.05mg/ml BSA 80
Figure 72 SAXS scattering from 18.3nm AuNPs functionalised with BSPP Fmoc-GFC 81
Figure 73 Peptide mediated surface assembly of Pep-Au onto QDs surface 83
Figure 74 Schematic of potential well formed in quantum dots 85
Figure 75 HR TEM image of a CdSe/ZnS Quantum dot 89
Figure 76 Comparison between Log Normal and Gaussian distributions 89
Figure 77 SAXS scattered intensity of CdSe/ZnS QDs 90
Figure 78 Photoluminescence spectra of QD and non-associating AuNPs 91
Figure 79 TEM and SAXS of Pep Au 92
Figure 80 Summated model intensity 93

Figure 81 Application of two particle population model to a mixture of non interacting QDs and AuNPs. 93
Figure 82 SAXS pattern of uPA 94
Figure 83 SAXS scattering patterns from conjugate assembly experiments 95
Figure 84 Schematic illustration of scattering length density for halo model and spherical particle approximation 96
Figure 85 Schematic illustration of Pep-Au:QD conjugate growth 97
Figure 86 Conjugate growth under constant QD concentration 98
Figure 87 Conjugate growth under constant Pep-Au concentration 99
Figure 88 Comparison of effective conjugate mean diameter for experiments performed under constant QDs and constant Pep-Au concentration. 99
Figure 89 Photoluminescence measurements of Pep-Au/QD conjugates 99
Figure 90 Langmuir adsorption equation applied to adsorption of Pep-Au onto QDs 100
Figure 91 Possible conformations of Pep-Au assembly on the QD surface. 101
Figure 92 Conjugate size and photoluminescence with and without uPA 102
Figure 93 Assessment of sample precipitation 103
Figure 94 Characterisation of CdSe/ZnS QDs reproduced from Dabbousi et al [48] 107
Figure 95 SAXS scattering curves (black) and model fits (red) to conjugate assembly under constant QD concentration. 108
Figure 96 SAXS scattering curves (black) and model fits (red) to conjugate assembly under constant Pep-Au concentration. 108

LIST OF TABLES

Table 1 Forces governing the nanoparticle interface 8
Table 2 Peak plasmon peak λ_{max} for AuNPs with various diameters 21
Table 3 The scattering length densities of water, gold, ZnS and CdSe 36
Table 4 Relative lattice positions and diffraction planes of lattice peaks for HCP, BCC and FCC lattices [86] 40
Table 5 Sticky hard sphere model fitted to AuNP aggregates functionalised with a range of capping ligands 79
Table 6 Substrate peptide sequences for Pep-Au 86

Table 7 Summary of Log-Normal and Gaussian distributions applied to CdSe QDs 89
Table 8 Summary of Spherical and Core-Shell form factor fits applied to CdSe QDs 91
Table 9 Summary of Log-Normal and Gaussian distributions applied to Pep-Au 92
Table 10 Summary of two particle population model to a mixture of non interacting QDs and AuNPs 94
Table 11 Imidazole disassembly of conjugates 104
Table 12 Conjugates formed using control substrate peptide 104
Table 13 Quantum dots and substrate peptide 105
Table 14 Control experiment of Pre-cleaved Pep-Au and QDs 105
Table 15 Summary of the QDs sizes from TEM and SAXS presented by Dabbousi et al [48] 107
Table 16 Conjugate assembly at constant QDs concentration 109
Table 17 Conjugate assembly at constant Pep-Au concentration 110
Table 18 Enzymatic dispersion of conjugates under constant QD concentration, experiment 1. 110
Table 19 Enzymatic dispersion of conjugates under constant QD concentration, experiment 2 (repeat). 111
Table 20 Enzymatic dispersion of conjugates under constant QD concentration, experiment 3 (repeat). 111
Table 21 Enzymatic dispersion of conjugates under constant Pep-Au concentration, experiment 1. 111
Table 22 Enzymatic dispersion of conjugates under constant Pep-Au concentration, experiment 2 (repeat). 112
Table 23 Enzymatic dispersion of conjugates under constant Pep-Au concentration, experiment 3 (repeat). 112

ACRONYMS

AuNPs Gold Nanoparticles

BSA Bovine serum albumin

BSPP Bis(p-sulfonatophenyl)phenylphosphine dihydrate

CdSe Cadmium Selenide

DLS Dynamic Light Scattering

DNA Deoxyribonucleic acid

ELISA Enzyme linked immunological assays

Fmoc Fluorenyl-9-methoxycarbonyl

FRET Fluorescence Resonance Energy Transfer

HSA Human serum albumin

MMP 7 Matrix Metalloproteinase 7

MW Molecular Weight

NPs Nanoparticles

NSET Nanometal surface energy transfer

Pep-Au 1.3nm Gold clusters with attached peptide

QDs Quantum Dots

SAXS Small Angle X-Ray Scattering

TEM Transmission Electron Microscopy

uPA Urokinase plasminogen activator

UV-VIS Ultraviolet-Visible Absorption Spectroscopy

ZnS Zinc Sulfide

ZP Zeta Potential

1 LITERATURE REVIEW

1.1 THE MATERIAL SOCIETY

The materials that we use, define the boundaries of our society. Early civilisations are often described in terms of their level of materials development e.g. Stone Age, Bronze Age, Iron Age. Early human civilisations were restricted to natural materials of plant and animal origin (wood, skin, bone) from which to build a society. The fragile and degradable nature of these materials limited the extent of infrastructure. Social pressures such as overpopulation and over-exploitation of natural resources demanded the development of new technologies such as agriculture, the extraction and purification of base metals from ore, eventually leading to new technologies such as carbon nanotubes. The development of techniques to mass manufacture cast iron (tensile strength 180MPa [131]) during the industrial revolution, later steel (tensile strength 450MPa [131]) and modern composite materials, have expanded the grounds for our society to grow.

Introductions tend to be dull; scientific ones tend to be rigorously so [44]

The chemical and structural patterning of materials on the nanoscale, can introduce novel optical, electronic, chemical and catalytic properties, which are not found in the materials bulk form. These radical changes in material behaviour can be translated into designing materials that respond to their environment. For example, the windows on modern skyscrapers are coated with microcrystalline titanium dioxide, designed to chemically break down dirt when illuminated with sunlight [181]. The promise of a materials revolution has brought about a renaissance in public and industrially funded research, with funding and investment estimated to total $10 billion in 2004 [88]. From 1999 to 2004, over 33,000 papers on nanotechnology were published, with the US as the largest contributor (18,000 papers) and Japan as the second largest (8,000 papers) [87].

This chapter provides an overview of current research in nanoparticle engineering with a focus on biomolecular detection. A focus is applied onto the application of polypeptides for programable nanoparticle assembly with reference to the engineering of inter-particle forces to control assembly structure and optical properties.

1.2 THE PROMISE OF THE NANOSCALE

The nanoscale is considered to describe distances between 1-100nm. Objects within this size range are assemblies containing between 10 – 10^5 atoms, lying between the sizes of individual atoms and bulk solids (Figure 1). Standard nano manufacturing techniques involve either assembly using a bottom-up approach or engraving through at top-down process.

Top-down processes such as lithography and micro-contact printing involve patterning macroscopic materials through the use of masks, electron/photon bombardment and chemical deposition (e.g. molecular-beam epitaxy). These typically are able to produce structures from micro

to nano dimensions, with lithography prototypes producing structures as small as 10nm.

The word LEGO was chosen in the 1930s from the Danish phrase "leg godt", which means "play well". Later on, it was realised that the word has the meaning "I put together" in Latin. [1]

Bottom-up approaches involve the growth of atomically precise structures from atomic or molecular components, through the used of chemical synthesis, self-assembly of molecular clusters and biological macromolecules. Structures are assembled from modular building blocks, which can be chosen to have a predetermined functionalities. An analogy can be drawn with lego bricks, where the coupling between pieces can be used to generate a responsive functional structure. Self assembly techniques are commonly used to produce nanoparticles, vesicles, micelles, polypeptides and a wide range of macromolecules. The boundaries between top up and top down approaches are not absolute, for example lithography templates can be manufactured from the assembly of colloidal nanoparticles into arrays [254].

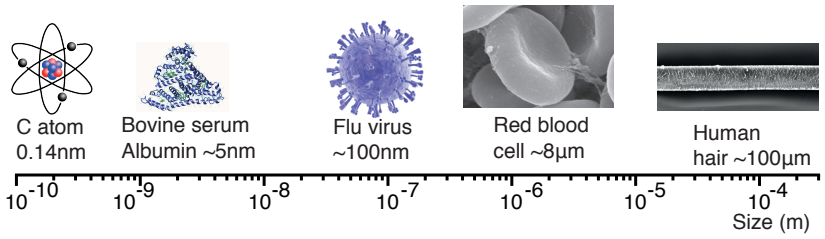


Figure 1: Relative dimensions of structures found in nature. Examples shown are a carbon atom, Bovine Serum Albumin, flu virus, red blood cell and a human hair.

The past 20 years have witnessed rapid growth in synthesising, measuring and manipulating materials on the nano-scale. Biological processes are inherently self ordering systems composed of nanoscale components. Biological structures frequently exhibit multi-functionality, self repair and strong mechanical properties (considering the softness of their component proteins), growing out of elaborate hierarchical structures [154]. Cellular organelles such as ribosomes demonstrate the potential of macromolecular self assembly. Ribosomes are efficient supramolecular machines approximately 20nm in size which self assemble from more than 50 different protein building blocks [132]. The exploration and understanding of how the basic building blocks (amino acids, lipids etc) function in biological materials opens new possibilities in engineering complex macromolecular materials.

1.2.1 *The medical need*

Efficient, sensitive biomolecule detection is a fundamental cornerstone of public healthcare, without which, modern medicine would not be possible. As a result, enzyme linked immunosorbent assays (ELISA) have become household names, playing an essential role in disease detection and fundamental biological research. Early detection is critical for the treatment of many diseases, driving the search for higher sensitivity and multiplexing in biomarker detection.

The art of medicine, consists in amusing the patient while nature takes its course –Voltaire

Whilst improvements in silicon technology have resulted in the free fall of electronics prices, the cost of healthcare has continued to rise. With the sequencing of human genetics leading to effective personalised but expensive treatment, the prospect of affordable accessible healthcare is becoming more distant. The silicon revolution grew out of

advanced engineering of hard solid-state two dimensional materials, whereas biotechnology relies on reverse engineering of 3D soft organic materials suspended in aqueous buffers. The challenge of nanotechnology comes from engineering such 3D systems from complicated subunits of polymers, polypeptides, lipids and inorganic particles.

The increasing drive for high sensitivity biomolecular detection has pushed for innovative assays using metallic nano-particle (NPs) imaging labels such as gold nanoparticles (AuNPs) and quantum dots (QDs). These metallic nano-scale materials exhibit unique physical and optical properties, with applications as novel and effective sensors for disease detection [214][12], imaging contrast agents [155] and therapeutic treatments such as drug delivery [159].

1.2.2 *Characteristics of the nano dimension*

The properties of bulk materials are often heavily dependent on their surface layers, affecting conductivity, strength, chemical susceptibility and optical characteristics. On the nano-scale, the surface dominates, for example in a 1.3nm gold nanoparticle approximately half of the gold atoms lie on the surface. These gold clusters are known to have exceptional catalytic properties [98]. The size of nanoparticles can be adjusted, through careful control of reaction conditions. This places them on a size range similar to that of proteins, laying the path for the design of complementary surfaces. The optical properties of metallic nanoparticles such as gold nanoparticles (AuNPs) and quantum dots (QDs) are of particular interest for biomolecular detection and medical diagnostics. The optical and electronic properties of a material are dictated by the kind of motion permitted for its electrons to follow [110]. Electrons bound to a material or atom, have confinement in their motion, leading to quantisation. As a result atomic and molecular orbitals have well defined energies and spectra. The more compact the confinement, the greater the gap separating permitted energy states.

1.2.3 *Quantum dots (QDs)*

The excitation of bulk semiconductor materials results in the excitation of an electron to the conduction band and the formation of a hole [110]. The smallest amount of energy required to form these is described by the band gap energy, i.e. the energy gap between the bottom of the conduction band and the top of the valence band. The recombination of the electron and hole can occur radiatively generating a photon in the process. Reducing the volume available for holes to move, confines their motion. As the physical dimensions of the semi-conductor particles approaches the nanoscale, their size becomes smaller than the Bohr radius. This increases the band gap difference, altering the band gap absorption and therefore the colour of particles [10]. Hence the emission spectrum of nano-sized semiconductor particles, called Quantum Dots, can be tailored through tight controlled of particle dimensions [10].

Semi-conductor Quantum Dots combine a broad absorption spectrum with a narrow tuneable emission spectrum placing them as a replacement for standard chemical fluorophores such as fluorescein (Figure 2). Their cores are typically composed of materials such as CdSe, PbS and InP [151], with the core diameter determining the peak emission spectrum. The tuneable emission wavelength of QDs can be

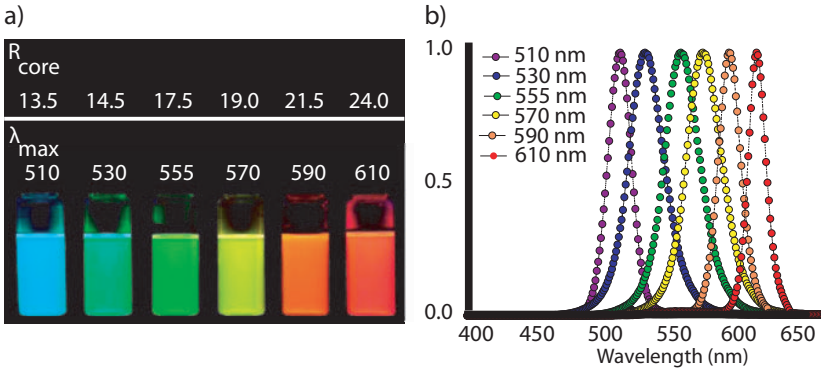


Figure 2: a) Emission spectra of CdSe/ZnS QDs excited with a near UV lamp. The particles have core radii of 13.5Å, 14.5Å, 17.5Å, 19Å, 21.5Å and 24Å with peak emission maxima of 510nm, 530nm, 555nm, 570nm, 590nm and 610nm. b) The plotted emission spectra from QDs. Images reproduced from [151].

used for concurrent excitation of a mixture of different-sized QDs, enabling their application in multiplex detection systems [37][42]. The core materials are often coated with a secondary material such as ZnS to enhance photo luminescence, prevent leaching of the core material into solution and inhibit the formation of electron or hole acceptors which can reduce photon efficiency [48][81]. Whilst thinner layers of ZnS (1-2 monolayers) generate the highest luminescent yield, thicker layers (4-7 monolayers) tend to be used for more protection in biological buffer solutions.

Quantum dots are typically synthesised in organic solvent, with particle size and shape tailored through control of reactant concentrations and ratios. Hence the QDs surface is characteristically hydrophobic, requiring surface functionalisation with molecules, such as thiol containing mercaptoacetic acid, to transfer QDs into aqueous solvent [259][252]. These surface ligands control the stability of QDs in solution, provide an anchor for biomolecular attachment and provide additional protection from degradation in biological buffers.

Biological molecules such as proteins can be conjugated to the QD surface via adsorption of histidine residue chains or thiol linkages [206]. The use of thiol containing cysteine residues enables protein anchoring via the sulphur atoms on the QD surface [102], whereas histidine residues form metal-affinity coordination bonds to the Zn surface atoms [206].

Quantum dots can behave as effective FRET donors to nearby electron rich species such as fluorophores. Fluorescence resonance energy transfer (FRET) describes a non radiative energy transfer mechanism between two adjacent fluorophores, one acting as an energy donor, the other as a receptor [66][200][205]. Hence the association of energy accepting fluorophores with QDs, quenches the QD luminescence [205]. The superior optical properties and resistance to photobleaching of QD FRET assays place them in a superior advantage compared to standard fluorophore-fluorophore FRET assays [196][41]. Gold nanoparticles can also behave as effective energy acceptors, quenching the luminescence of QDs more effectively than organic fluorophores [107]. This higher quenching efficiency promises greater assay sensitivity, with QD-AuNP conjugates demonstrated to detect proteases [107].

The optical luminescence of Quantum Dots places restrictions in dynamic characterisation using laser scattering techniques such as DLS [83]. As a result alternate techniques such as SAXS or SANS are often chosen to provide dynamic structural information [48].

1.2.4 *Gold nanoparticles (AuNPs)*

The use of gold nanoparticles as a colorant stretches as far back as the Roman Empire, although it was only until the 19th Century that Faraday hypothesised that the colour of AuNPs originated from the presence of small particles suspended in solution. Spherical monodisperse particles (i.e. ones with a coefficient of variation <10%) can be synthesised in a size range from approximately 2-200nm [108]. Other shapes have been demonstrated such as cuboid [84], prisms [215] and rodlike [73][49].

One of the most common methods of AuNP synthesis, involves the citrate reduction of $HAuCl_4$ in water, first described by Turkevitch et al [235]. Particle diameter and polydispersity is controlled through choice of reactant concentrations and pH [108]. It is also possible to synthesise AuNPs in organic solvent through the two-phase water-toluene reduction of $AuCl_4^-$ by sodium borohydride in the presence of dodecanethiol [31].

The deep ruby red colour displayed by AuNPs (Figure 3a) arrises from the collective oscillation of metal surface electrons with incident light. A theoretical description of this phenomenon was first provided by Mie in 1908 [156]. The incident light wavefront polarises the particle electron density towards one surface. As wavefronts pass across the particle, the electron density oscillates in resonance with the light frequency [137][247]. The resonance condition and hence the location of the optical absorption band is decided by particle shape, size and the dielectric constants of both the particle and the surrounding environment [78]. This enhanced optical extinction effect is commonly labelled surface plasmon resonance, due to the location of the electron plasmon oscillation on the particle surface. As a result of this effect, AuNPs are excellent scatterers and absorbers of light [59], with an optical scattering cross-section up to a million times greater than standard chemical fluorophores [12].

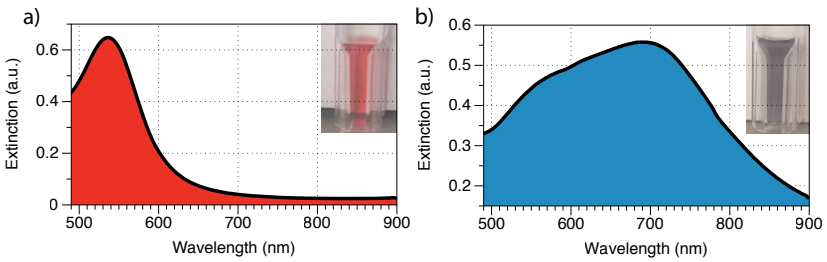


Figure 3: UV-VIS extinction spectra for 20nm AuNPs in a) disperse b) aggregated states. The inserts display the visible colour of the solution at these states.

The adsorption of surface species such as biomolecules results in a small change (~1-2nm) in peak absorption position and is too small to be observed visually. Hence most AuNP assays, rely on change in NP assembly state. The onset of aggregation results in a broadening and shift of the absorption spectrum to higher wavelengths, with a visible

solution change from red to blue/purple [222] (Figure 3b). The location and extent of this band is greatly influenced by aggregate structure and growth mechanisms [179].

Gold nanoparticles are commonly stabilised in solution through the use of surface species such as citrate, polymer coatings or thiolated compounds. The attachment of biological species onto AuNPs is possible via the thiol group on a cystine residue, opening the possibility of incorporating programable biological functionality into NP assembly state. Functionalised AuNPs have been demonstrated for use in bioimaging [219], therapeutics [159], DNA sequencing [160], detection of genetic disorders [231] and other biosensing applications [3][202].

1.3 NANOPARTICLE SURFACE - SHAPING THE INTERFACE

The assembly of nanoparticles into discrete, well defined 1D, 2D and 3D structures [64] has been demonstrated by exploiting the versatile range of interactions between nanoparticles, such as Van der Waals [188][167], hydrostatic stability [33], electrostatic interactions [99] and hydrogen bonding [201]. However it is difficult to precisely control the placement and arrangement of individual components when assembling hierarchical nanoparticle structures. Biological materials such as DNA and simple polypeptides provide specificity in interaction through the formation of complementary sequences. When conjugated to inorganic NPs, this specificity can be used to accurately control the assembly of novel hybrid nanoparticle assemblies. Particles are typically functionalized with molecular linkers containing recognition groups which are complementary to each other. The particles are then drawn to each other, to specifically assemble into NP assemblies.

1.3.1 *Surface functionalisation as a necessity for colloidal control*

Nanoparticle solutions are typically thermodynamically unstable, with kinetic stability provided by the addition of adsorbed chemical species. Particles moving under brownian motion are subject to frequent collisions. The sum of the attractive and repulsive forces acting on colliding particles dictates whether the particles remain joined or separate. The main forces that need to be considered here are Van der Waals, electrostatic interactions, osmotic, steric and biomolecular specific entropic interactions [223].

Van der Waals forces are present in all materials and are the main force responsible for the intrinsic instability of uncoated nanoparticles. They originate from the quantum mechanical fluctuations of electrons, which induce dipole moments in adjacent atoms, resulting in a net attractive force [105][158]. This intrinsic instability requires control through NP surface functionalistion by adsorbed chemical species, which can introduce kinetic stability via the use of charge and/or steric repulsion (Figure 4).

Charged particles suspended in aqueous solution, attract oppositely charged solution ions and repel those with a similar charge, forming a double layer [44]. The distribution of counter ions near the charged particle surface can be represented using Stern-Gouy-Chapman theory, where the ions are described to exist across two layers: a tightly packed inner layer and a less dense outer layer. The collision of particles results in the overlap of their diffuse layers, generating a repulsive force

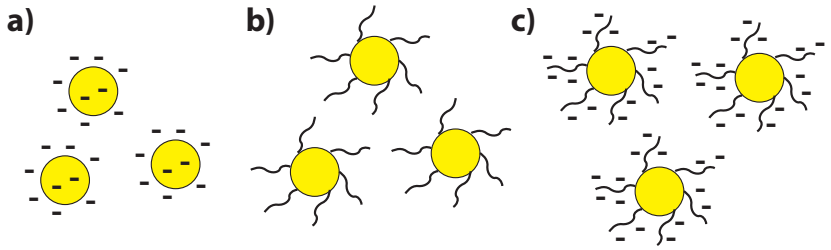


Figure 4: Schematic representation of colloidal stabilisation for a) charged particle adsorption (electrostatic stabilisation), b) adsorption of neutral polymers (steric stabilisation), and c) attachment of charged polypeptides (electrosteric stabilisation).

between particles. In solutions of high ionic strength such as physiological fluids, the double layer becomes strong enough to screen the electrostatic charge of particles negating the effect of any electrostatic stabilisation. This is the reason why citrate stabilised AuNPs aggregate upon the addition of small quantities of NaCl.

Steric stabilisation relies on adsorbed surface species acting as a physical barrier to prevent particles from touching. This form of stabilisation has a lower sensitivity to salt concentration and is commonly achieved using thiolated polymers or polypeptides. For sufficiently hydrophilic particles, water can attach strongly enough to provide a steric stabilisation layer. This is often referred to as hydrophilic repulsion or hydration pressure.

More hydrophobic particles exhibit a greater affinity for each other than to water resulting in a net attraction towards each other [166]. Simple solvation effects can be used to assemble nanoparticles into monolayers through the use of Langmuir Blodgett troughs [30][123][207]. Hydrophobic particles are deposited onto the surface of an aqueous solution and the accessible surface area reduced, forming a close-packed monolayer of the colloidal particles on the aqueous liquid surface. The nanoparticle solvent is allowed to evaporate and the particle monolayer transferred to a substrate.

Electrosteric stabilisation describes a situation where the adsorbed surface species offers a combination of both electrostatic and steric repulsion. Levy et al. have demonstrated exceptionally stable AuNPs through functionalisation with the polypeptide sequence CALNN [127]. These AuNPs are stable in a wide range of pHs and ionic strengths. The polypeptide is designed such that the thiol group in the N terminal cysteine (C) enables anchoring onto the AuNP surface, the Alanine (A) and leucine (L) have hydrophobic size chains, promoting the assembly of the peptide monolayer and the C-terminal asparagine (N) residues are hydrophilic in nature containing a slight negative charge due to the terminal carboxylic group. The polypeptide chain can be further modified to introduce molecular recognition through functionalisation with biotin or DNA [126]. Electrosteric stabilisation has also been demonstrated for nanoparticles coated in DNA [160], folding polypeptides [5] and phosphate salts [9].

Force	Origin and nature
Hydrodynamic interactions	Brownian diffusion and convective motion are often altered near interfaces
Electrodynamic interactions	Van der Waals interactions between surface and adjacent material
Electrostatic	Charged surfaces form counter ion electrostatic double layers
Solvent interactions	The hydrophobic/hydrophilic nature of a material effects its stability in aqueous solvents.
Steric interactions	Adsorbed species such as polymers, can introduce a repulsive force between particles through physical repulsion.
Bio-molecular/polymeric bridging	Adsorbed species can be used to reversibly control particle stability as a response to external stimuli (solvent, introduction of complementary biomolecule)

Table 1: Forces governing the nanoparticle interface.

1.3.2 *The bio-nano interface*

The nanoparticle solid-liquid interface is metastable by nature, with the distribution of adsorbed surface species subject to dynamic and spatial inhomogeneity. The introduction of nanoparticles to physiological fluids results in the surface coating of particles by biomolecules. This protein corona alters the surface properties of nanoparticles (e.g. stability/hydrophobicity/charge/oxidative damage) [36]. Biomolecular adsorption is a complex process, with a range of factors affecting adsorption such as particle geometry, physiochemical makeup and biomolecule composition (charge, size, stability, composition and conformation) [165]. The wrapping of proteins onto the surface of particles, may result in their conformational changes deforming the structure of biomolecules and exposing of previously hidden residues [138][143]. Bovine serum albumin and human serum albumin, both used in commercial bio-assays are known to bind and undergo conformational changes on the surface of gold nanoparticles [29][234].

Associating proteins can interact with pre-existing surface species emanating from initial particle synthesis. The association and dissociation of proteins to nanoparticles is a complex dynamic process [165]. Solution protein concentration is known to effect binding, for example nanoparticles suspended in plasma are known to be initially coated in fibrinogen and human serum albumin, but with time, these are displaced by other lower concentration but higher affinity proteins [36].

1.3.3 *Biomolecular mediated nanomaterial assembly*

Self assembly describes the fabrication and gathering of individual components into a structured entity. By taking advantage of the extensive and flexible chemistry of nature nanoparticle surfaces can be

functionalised with recognition molecules designed to react to subtle physicochemical changes. This enables the engineering of biosensors that transduce molecular changes into visual signals.

Through appropriate encoding and control of molecular subunits for selective binding, nanoparticles can be assembled into ordered hierarchical materials. The two most common methods of biomolecular nanoparticle assembly is through the use of polypeptides or DNA.

The characteristics of polypeptides can be customised through management of their amino acid positioning to emulate proteins found in nature or implement novel designer behaviour. Increasing expertise in protein chemistry and synthesis joined with advancements in comprehending the intricate relationship connecting amino acid sequence and 3D protein structure allow for the engineering of novel polypeptides. Additional flexibility is introduced from the ability to integrate chemical groups that are not found in nature. Synthetic polypeptides have been engineered that can fold and unfold in a precise manner, specifically recognise biomolecules and imitate the behaviour of enzymes [3][100][251][80][27][14].

Deoxyribonucleic acid (DNA) is the assembly guidebook of all living organisms and has been demonstrated to assemble nanoparticles such as CdSe/ZnS QDs [242] and AuNPs [178]. DNA is composed of two base complementary strands, which are able to fold into a double helix motif. The four nucleotides found in DNA are adenine (A), thymine (T), guanine (G) and cytosine (C). The nucleotides specifically cross-bind (G to C and T to A), permitting for the specific assembly of nano-materials [64]. The use of sequences of complementary base pairs, enables the rational encoding of DNA base paring interactions, to programmably assemble nanoparticles into ordered structures.

Early nanoparticle systems attempted to functionalise nanoparticles with anti-bodies, however anti-bodies are often of similar size or larger than the NPs, limiting the extent to which assembly and inter-particle spacing could be controlled. Additionally, the high surface curvature of NPs can deform the native states of adsorbed antibodies. However, antibody functionalised gold nanoparticles have been used in commercial home pregnancy kits [72][233][256]. The use of polypeptides or DNA negates the size constraints applied by large antibodies. The smaller chains of peptides or strands of DNA are less prone to aggregating particles or loosing functionality when anchored to nanoparticles.

1.3.4 *Crosslinking and non-crosslinking approaches to programable nanoparticle assembly*

Broadly speaking biomolecular nanoparticle assembly can be classified as either crosslinking or non-crosslinking. Crosslinking aggregation relies on the formation of junctions between particles where as non-crosslinking relies on the change in particle stability via the removal or addition of colloidal stabilisation effects.

Non-Crosslinking aggregation

Nanoparticle aggregation is triggered by the directed loss of steric, electrostatic or electrosteric stability, without the use of inter-particle linkers. By careful choice of surface species such as biomolecules, particle stability can be reversibly controlled as a response to external stimuli (e.g.

solvent or introduction of complementary biomolecule). For example Li and Rothberg have demonstrated an improvement in electrostatic stability in citrate coated AuNPs upon the addition of single stranded DNA (ssDNA) [129]. Hybridization of ssDNA with a complementary target forms double stranded DNA (dsDNA) which is unable to efficiently bind to citrate coated AuNPs. At elevated salt concentrations (e.g. 200mM NaCl) ssDNA is able to stabilise citrate coated AuNPs whereas dsDNA results in nanoparticle aggregation. Similar systems have been developed to detect thrombin, ATP [240], K^+ [241] and Hg^{2+} [128]. This method can be adapted for enzyme detection, for example Zhao et al have demonstrated the detection of alkaline phosphatase [255]. Alkaline phosphatase dephosphorylates highly charged ATP into neutral adenosine. ATP and adenosine adhere to the surface of AuNPs, where the charged ATP maintains AuNP stability while neutral adenosine induces AuNP aggregation.

Another non-crosslinking pathway induces loss in electrosteric stability through conformational changes of adsorbed stabilisers. The enzymatic cleavage of DNA anchored onto the surface of AuNPs has been demonstrated to detect DNase 1 and Pb^{2+} [258]. The cleavage of DNA reduces the electrosteric stability of AuNPs, resulting in their rapid aggregation and a visible colour change.

Non-crosslinking systems typically rely on barely stabilised AuNPs [258] and the use of salt modulation to achieve colourimetric changes. The systems are therefore highly sensitive to small environmental physiochemical changes such as electrolyte concentration or presence of unaccounted biomolecules. This places uncertainties in long term solution stability and the possibility of false results when working with physiological fluids. Robust non-crosslinking assays will necessitate strategies for preventing non-specific protein adsorption and non-specific NP aggregation. Never the less, the fine stability control of NPs needs to be considered in the fundamental design of any NP bioassay.

Crosslinking aggregation

The use of crosslinkers such as polypeptides or DNA, is the most commonly exploited method for assembly based nanoparticle bioassays, providing a reliable method for assembly control.

The overall charge of polypeptides can be modulated through protonating or de-protonating their constituent residues via control of pH. This enables engineered polypeptides to fold or unfold in response to pH. Aili et al have demonstrated the use of de novo designed folding polypeptides for the controlled assembly of AuNPs.

The assembly mediators are two 42 residue synthetic helix-loop-helix polypeptides, JR2EC and JR2KC, that heterodimerise in solution into four-helix bundles [56][4]. The folding is promoted by the establishment of a hydrophobic core constructed from the hydrophobic surfaces of the amphiphilic helices. At pH 7 the polypeptides JR2EC and JR2KC are negatively (-5) and positively charged (+11), with favourable electrostatic interactions inducing heterodimerisation but hindering the creation of homodimers. Both polypeptides have a cysteine residue in the loop region (position 22), enabling for the creation of fiber forming units $JR2EC_2$ and $JR2KC_2$ through linking two monomers by a disulphide bridge [4].

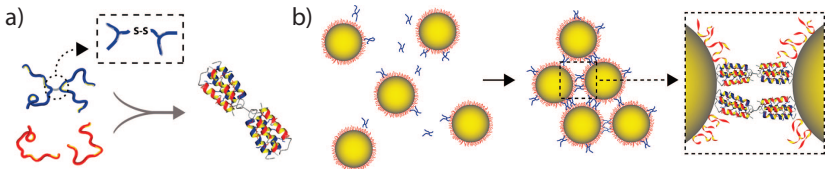


Figure 5: Schematic illustration of AuNP assembly using de novo designed polypeptides. a) Assembly of four disulphide-linked four-helix bundles, through the association of JR2KC$_2$ and two complementary JR2EC polypeptides; b) Introduction of JR2KC$_2$ to AuNPs functionalised with JR2EC induces formation of ordered nanoparticle assemblies through polypeptide bridging . Images reproduced from [6].

JR2EC is immobilised onto the surface of AuNPs via the cysteine residue, with the following introduction of JR2KC$_2$, bringing about the assembly of particles through the formation of two disulphide linked four helix bundles, composed of two JR2EC molecules linked by JR2KC$_2$ (Figure 5) [6]. The NPs assemble into ordered assemblies with an inter-particle spacing of 4.8±0.4 nm.

DNA has been widely exploited as an assembly mediator, with Mirkin et al demonstrating a detection system for DNA molecules initiated by hybridising two complementary DNA strands on AuNPs [55]. The addition of target DNA results in the assembly of the AuNPs accompanied by a visible colour change from blue to red. The assembly can be reversed by raising the sample temperature above the melting point of DNA [195][180]. This assembly strategy has been adapted to detect mercury ions [250], cysteine [124] and oligomeric hairpin DNA sequences [89].

DNA mediated assembly can also be used to precisely control the crystal structure of 3D AuNP aggregates [180]. The particle assembly structure can be cycled through face centred cubic (FCC), disordered and body centred cubic (BCC) structures through control of temperature and linker length. For shorter linker lengths a BCC structure becomes energetically favourable due to lower volume fractions [63]. For quasi-crystalline order to occur, highly monodisperse particles are required (<10%), with polydispersity reducing the entropic advantage of FCC over BCC structures [104]. More exotic structures can be made using nanorods [168], octahedrals [169], rhombic dodecahedra [169] and triangular nanoprisms [76][157]. The sensitivity of DNA functionalised AuNPs to inter-particle distances combined with thermal reversibility and controlled stability facilitates the development of responsive ordered meta-materials.

1.3.5 *Nanoparticle assembly structure*

Nanoparticle assemblies range from disordered to quasi-crystalline, with structure dictated by the interaction between particles, colloidal forces and fundamentally the needs to minimise energy and maximise entropy [63][228]. Nanoparticle aggregates typically form clusters with fractal characteristics, which are related to their aggregation mechanisms. The aggregation mechanisms and resultant fractal aggregate structures for citrate coated AuNPs have been extensively studied [147][133][94]. Fractal aggregates are typically polydisperse in distribution, but the cluster mass (M) scaling with aggregate size (Rg) has

a power-law form i.e. ($M \sim R_g^{D_f}$) [147][179]. Hence the cluster mass scaling with size provides a signature fractal dimension D_f, which correlates with the type of aggregation process.

For the irreversible kinetic aggregation of citrate coated AuNPs, two aggregation regimes have been classified, derived on the assumptions of particle diffusion, mobility and sticking probability (Figure 6). The first class, Diffusion limited cluster-cluster aggregation (DLCA) ($D_f \sim 1.8$), assumes nanoparticles affix whenever they collide resulting in fast forming branched aggregates. The second class Reaction-limited cluster-cluster aggregation (RLCA) ($D_f \sim 2.1$) introduces a barrier to sticking such that multiple collisions are needed for permanent sticking. This leads to slower forming but denser aggregates [209][94]. For aggregates where particle sticking is non-permanent, a third aggregation regime called compact clusters (CC) ($D_f \sim 3$) becomes predominant [179]. Here the NP subunits are able to dynamically rearrange into denser, more energetically favourable structures.



Figure 6: Projections of 3D NP clusters generated using off-lattice aggregation models for a) Diffusion limited cluster-cluster aggregation (DLCA), b) Reaction-limited cluster-cluster aggregation (RLCA) and c) compact clusters (CC). Images are reproduced from [150].

The biomolecular functionalisation of NPs directly effects NP assembly mechanism and therefore the resultant assembly fractal structure. The fractal dimensions and corresponding UV-VIS extinction cross-sections of AuNPs assembled using DNA have been investigated by Mirkin et al [179][174][180][178]. They numerically generate theoretical RLCA, DLCA and CC AuNP assemblies and model their extinction cross sections. These spectra are then compared with experimentally obtained UV-VIS measurements. UV-VIS absorption spectra are known to be dominated by the surface area of the aggregate, with less dense fractal structures (i.e. lower fractal dimension) displaying a larger surface area and therefore higher extinction. However increases in fractal dimension tend to red-shift the absorption spectra. The fractal dimensions and therefore optical extinction spectra for DNA coated AuNPs can be controlled by controlling the effective sticking probabilities of the DNA linker units. Bellow the melting temperature of DNA, the dissociation lifetime of the DNA duplexes is considerably longer than the aggregate formation time, forming structures consistent with RLCA dynamics [179]. As the temperature is increased towards the melting temperature of DNA, the dissociation lifetime becomes shorter, enabling particles to assemble into more compact structures such as CC [178].

1.4 SCOPE OF THESIS

The complex dynamic interface between colloidal nano-materials and biomolecules is shaped by a wide range of physiochemical interactions and forces. The nature of these interactions determines the sensitivity, stability and overall effectiveness of any NP bioassays. The strategies outlined in this review for altering the assembly state of NPs, involve the use of biomolecular crosslinkers or NP stability modulation. Reproducible control of NP optical transitions requires understanding and mastering the delicate interplay between biomolecular and colloidal forces to precisely craft NP structures.

A significant challenge remains in maintaining NP effectiveness in physiological fluid such as serum and blood for both in-vivo and in-vitro implementation. Novel methods for preventing non-specific NP aggregation and biomolecule adsorption are required. Further understanding of the contribution of each assay component to NP stability and assembly structure would enable the decoupling between analyte binding properties and stability. This would permit the rational design of more complicated systems comprised of many distinct interchangeable components (e.g. stability modulators, nanoparticles, linkers, receptors).

Such systems could offer a robust generic approach to building multiplex bioassays which can be easily adapted to detect a wide range of analytes.

This thesis focuses on the development of metallic NPs for biosensing, through the use of synchrotron imaging as a core method of investigation. Small Angle X-ray scattering is used for its ability to provide nano-scale structural information on NPs systems, dynamically, in solution and in-situ. Synchrotron measurements are complemented with UV-VIS absorption spectroscopy, dynamic light scattering (DLS), SDS gel electrophoresis and TEM to provide additional complementary information.

Chapter 4 investigates the role of bovine serum albumin in nanoparticle assays, looking at binding and stability control as a function of both NP size and NP surface chemistry. BSA is commonly used in biochemical assays and is analogous to human bovine serum albumin found in human physiological fluid. The non-specific binding of BSA to AuNPs can therefore be used as an initial model for NP-protein interactions in physiological fluid.

Chapter 3 investigates the structures of AuNPs assembled using de novo designed polypeptides developed by D. Aili [7]. Changes in particle ordering, UV-VIS extinction coefficient, aggregation dynamics and mass fractal dimension are measured as a function of linker concentration and particle size. These transitions are related to changes in linker mediated interaction potential, particle surface charge and mobility within the aggregates.

Chapter 5 investigates the peptide mediated assembly of AuNPs onto the surface of QDs for the detection of urokinase plasminogen activator (uPA). The superior optical properties and resistance to photobleaching of QDs and high quenching efficiency of AuNPs, place QD-AuNP conjugate FRET assays in a superior position compared to standard chemical fluorophore assays [196][41][107]. The optical luminescence of QDs places restrictions in dynamic characterisation using laser scattering techniques such as DLS [83]. The surface assembly of

AuNPs onto the surface of QDs is therefore characterised using in-situ SAXS. Complete conjugate disassembly is observed upon the addition of the enzyme uPA, however QDs luminescence does not fully recover indicating that other effects may result in the permanent quenching of QDs.

2 EXPERIMENTAL METHODS

2.1 MEASURING AT THE NANOSCALE

For research purposes, it is often convenient to assume steady state behaviour when working with colloidal nano materials, e.g. assuming constant surface charge, isoelectric point, protein coverage, particle and aggregate size. However, the metastable solid-liquid interface found on nanoparticles, is subjected to a transient in-homogenous dynamic environment resulting from the distribution and spatial localisation of surface species (proteins, lipids, citrate etc). Additionally samples typically display polydispersity in size and structure. Hence, when characterising nanoparticles *static, localised* and *ex-situ measurements* are *insufficient;* techniques are needed which can accommodate the metastable, polydisperse and dynamic nature of the nano-surface.

Scattering techniques are powerful tools for the characterisation of materials with structural details on the nano scale. The length scales that can be resolved in scattering experiments are set by the choice of probe used (e.g. x-rays, neutrons, electrons). For example, static light scattering measurements (SLS) are able to resolve length scales from 100 nm – 10 μm, whereas x-rays are able to reach smaller scales of 0.1 – 100 nm. For particles considerably smaller than the wavelength of incident light (i.e. d~λ/10), the light is scattered uniformly in all directions (Rayleigh scattering), while for bigger particles (d~λ), the scattered intensity becomes angle dependent (Mie scattering). As a result combining different scattering techniques, along with a selection of different probes it is possible to systematically characterise complex particulate systems across a range of scales (Figure 7).

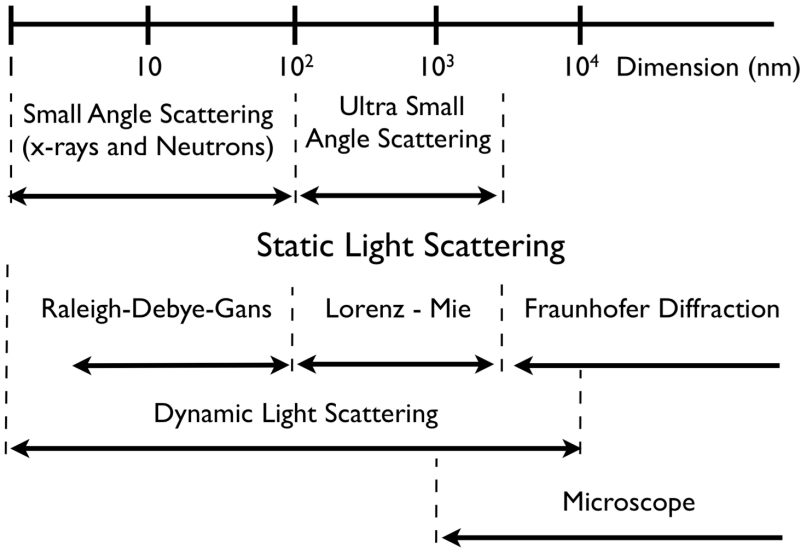


Figure 7: Accessible size ranges of different scattering techniques, adapted from [69]

Synchrotron sources provide high flux, coherent x-rays suitable for probing the microstructure and interactions in nano systems. The gen-

erated beams, typically possess a macroscopic footprint, illuminating a sample area rather than individual particles. As a result, synchrotron x-ray scattering provides ensemble averaged information such as particle size distribution and average assembly structure of analytes. This is particularly useful for colloidal materials, where suspended particles are intrinsically polydisperse exhibiting a size distribution. An added advantage is the ability to measure analytes structure while dispersed in solvent, with controlled time based measurements allowing for capture of dynamic processes. In contrast electron microscopy techniques (e.g. TEM) provide high resolution spatial images of small sample areas, restricting measurement information to single or small groups of particles. Additionally, the necessity to perform measurements in ultra high vacuum, often necessitates sample modification e.g. drying.

Fundamentally, synchrotron scattering techniques are indirect techniques, requiring assumptions to be made during data analysis. A common approach is to build structural models, calculate a theoretical scattering curve and compare it to experimentally obtained scattering data. Scattering measurements from colloidal systems generate a one dimensional low resolution data set due to the ensemble and directional averaging of the dispersed material. As a result, efficient beamline optics and accurate background subtraction is essential; often it can only be determined if a certain model supports or disagrees with obtained data, allowing for the possibility that other models may also fit. It is therefore critical to find the best model that supports the physical characteristics of the system and to be cautious to avoid over fitting the data.

This chapter provides a description of experimental techniques applied in subsequent chapters (DLS, Zeta-potential, UV-VIS spectroscopy, TEM, SAXS). The nature of each characterisation technique affects the quality and nature of the data collected. This must be taken into account when comparing measurements taken using different techniques. Detailed chemistry and sample preparation protocols are included in each relevant chapter.

2.2 DYNAMIC LIGHT SCATTERING (DLS) AND ZETA POTENTIAL (ZP)

DLS and ZP measurements where performed using a ZetaSizer nano (Malvern Instruments). The machine uses non-invasive backscattering (NIBS®) with a 633nm He-Ne laser. DLS measurements were performed using standard 1 cm path length UV-VIS semi-micro cuvettes whilst ZP measurements required the use of special zeta cuvettes. The sample absorbance at 633nm was obtained using a UV-VIS spectrometer; a refractive index of 0.47 was used for AuNPs [234]. Once the refractive index information and sample absorption at 633nm are provided, the ZetaSizer software automatically calculates the required measurement time and calculates the hydrodynamic radius (for DLS) or zeta potential.

2.2.1 *Dynamic Light Scattering*

DLS is a technique commonly used to characterised the hydrodynamic size of nano particles and colloidal materials in solution [95][28][44]. Dynamic scattering looks at the time dependence of the scattered light intensity to monitor particles moving under Brownian motion. The scattered light fluctuates due to particle movement and is recorded as an

autocorrelation function of photocurrent fluctuation. As the origins of this fluctuation are particle motion the translational diffusion constant (D_{diff}) is obtained. The hydrodynamic radius of the particles can be calculated via the Stokes-Einstein equation:

$$d_h = \frac{kT}{3\pi\eta D_{diff}} \tag{2.1}$$

Where d_h is the hydrodynamic diameter, D_{diff} is the translational diffusion constant, K is Boltzmann's constant, T is the absolute temperature and η is the medium viscosity. Most particles dispersed in an aqueous system are charged or gain surface charge, which alters the distribution of the surrounding ions, causing the layer around the particle to act differently compared to the bulk solution. When the particle moves under Brownian motion, this layer moves along with the particle. The measured hydrodynamic diameter is related to how a particle diffuses within a fluid and hence describes both the particle core and the surface layer. Particle size strongly effects the scattered intensity of light through a colloidal solution. The Rayleigh approximation, used in DLS, indicates that the scattered light intensity (I) has a dependence on particle diameter (d) (i.e. $I \sim d^6$), leading to more intense scattering from larger particles. Hence DLS typically records an intensity weighted particle size, with a transformation to a volume based size distribution possible using Mie theory provided that the particle refractive index and absorption values are known.

This intensity weighted bias limits the resolution of the technique, with DLS only able to resolve materials with at least a factor of 3 difference in size. This means that a mixture of different particle populations or an aggregate composed of particulate subunits would produce a broad single peak with the result obtained skewed by the larger particles. As a result DLS is excellent for estimating particle sizes from a single population of monodisperse particles and for identifying the presence of aggregates, but struggles to characterise the size distributions within aggregates.

Analyte concentration must also be considered when taking measurements, low analyte concentrations provide a lower scattered intensity and therefore higher noise/signal ratio. This lower limit depends on the refractive index difference between the sample material and its solvent and the optical scattering cross section of the material. High concentrations provide greater scattering, but higher particle volume fractions introduce particle-particle interactions, resulting in particle motion which is no longer purely Brownian in nature. Each sample material has its own ideal range of sample concentration for optimal measurements. For example, the protein BSA (refractive index 1.44 [234]) immersed in a water solvent (refractive index 1.33) can be detected at 0.5mg/ml, whereas 10 AuNPs (real component of refractive index 0.197 [244] at wavelength of 633nm) can be detected at concentrations as low as 6ng/ml.

2.2.2 *Zeta potential measurements (ZP)*

Charged particles in solution attract solvated ions around them resulting in a shielding of their surface charge. The distribution of counterions surrounding a charged surface displays a two layer morphology

consisting of a compact inner layer (Stern layer) and a diffuse outer layer. Inside the diffuse layer there exists a boundary inside which the ions and particles form a stable entity (surface of hydrodynamic shear). When the particle moves, ions within the surface of hydrodynamic shear move with the particle. The ions outside this boundary remain with the bulk solvent. The potential at the surface of hydrodynamic shear can be measured experimentally using electrokinetic experiments, where movement of the particle relative to its suspended solvent under the influence of an applied electric field is recorded. This measured potential, known as the zeta potential (ZP) describes the potential at the shear plane between the particle and solvent underflow (Figure 8) [44]. Measurement of the zeta potential provides an estimate of the electrostatic stability of colloids, with zeta potentials of ZP $\geqslant |30|$ normally considered stable [44][28].

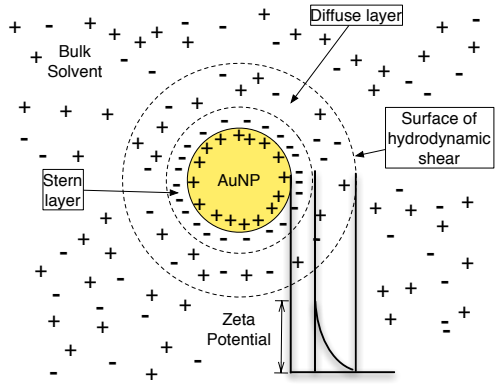


Figure 8: Schematic representation of zeta potential. Positively charged AuNPs attract a distribution of negative counter-ions surrounding the charged interface. The counter-ions can be broken down into layers: a tightly packed compact inner layer (Stern Layer) and a diffuse outer layer. For the particle and solvent under flow, a shear boundary is formed, inside which ions move with the particle. The Zeta Potential (ZP) describes the measured potential at this shear plane [44].

2.3 ULTRAVIOLET–VISIBLE ABSORPTION SPECTROSCOPY (UV-VIS)

The absorption of photons (in the UV-VIS region), by the electrons of molecules, results in their electronic transition to a higher energy state. The electronic transitions in complex molecules, are dependent on the chemical groups and bonds present in the molecule. The electron decay to its ground state, can occur through either a radiative (e.g. fluorescence) or non radiative process. [225]

Ultraviolet-visible spectroscopy (UV-VIS), is an absorbance technique, commonly used in the quantitative characterisation of solutions of metal ions, organic compounds, biological macromolecules and nanoparticles. A UV-VIS spectrometer measures the intensity of light passing through a sample (I_s) and compares it to the light intensity of light passed through an empty reference (I_0) as a function of wavelength. The absorbance (A) is defined as

$$A = \log_{10}(I_0/I_s) = \varepsilon bc \tag{2.2}$$

Where ε is the molar extinction coefficient, c is the molar concentration and b is the cell path length. UV-VIS measurements were performed using either a Perkin-Elmer Lambda or a Jasco V-630, using standard 1 cm path length UV-VIS semi-micro cuvettes. A Peltier unit combined with a temperature probe was used to maintain an elevated temperature for enzyme experiments.

2.3.1 *Surface Plasmon Resonance*

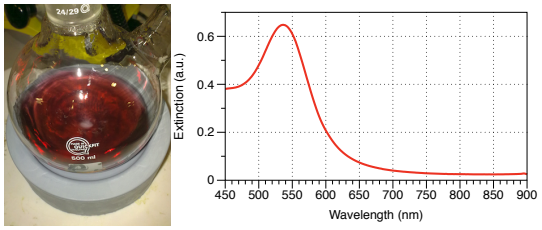


Figure 9: a) 20nm AuNPs, synthesised via citrate reduction of gold chloride [108]. Surface plasmon resonance provides AuNPs with their deep ruby red colour. b) The corresponding UV-VIS spectrum of the 20nm AuNPs; the peak plasmon absorption occurs at approximately 521nm.

The term plasmon describes the quantised collective longitudinal oscillation of valence electrons in metals. Noble and alkali metals typically display plasmon energies in the range of 5-10eV, with the reduction of material size to the nanoscale, core polarisability and changes in effective electron mass shift the plasmon energy into the visible light region (2-3eV). The illumination of Gold nanoparticles (AuNPs) with light, of wavelength much greater than the particle size, induces the collective oscillation of surface electrons in the metal. The passing light wave front's electric field polarises the electron density in the particle towards one surface (Figure 10) [137][247]. As the negative electron cloud is displaced relative to the positive metal nuclei, a coulomb based restorative force is introduced. If the frequency of incident photons matches the eigenfrequency of the collective electron oscillation, resonance occurs leading to strong oscillations for even small incident fields. Hence the resonance condition and oscillation frequency are determined by the strength of the restoring force which depends on the electron density, the effective electron mass, the shape and size of the charge distribution and the dielectric constants of both the particle and the surrounding environment [78]. As the electron plasmon oscillation is located at the particle surface, the effect is commonly described as surface plasmon resonance [58].

Mie's solution to Maxwells equations provide a method for relating the dipole plasmon frequency of spherical particles to their complex dielectric constants. Mie's theory is useful as it provides a simple and exact solution to Maxwell's equations, with important features observed experimentally. Mie's electrodynamical model assumes sharp boundaries, spatially homogeneous materials and neglects some many-body effects.

The environment that nanoparticles are used in can be a complex one, due to factors such as solvents, substrates and the proximity of other nanoparticles. This requires the modification of Mie's thoery to describe the optical properties of nanoparticles of various dimensions

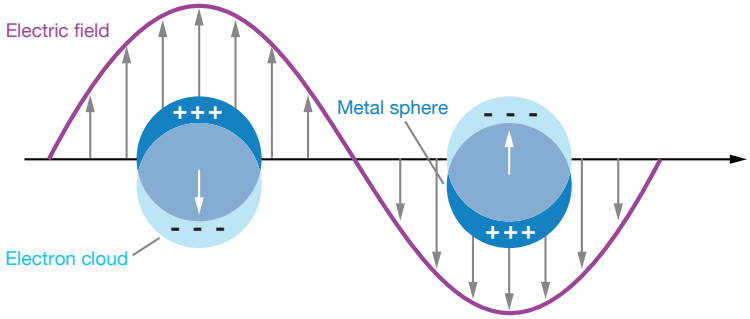


Figure 10: Schematic illustration of localised surface plasmon resonance. The electric field of incident photons induces a polarisation of the conduction electrons relative to the heavy core of the metallic particle. A charge difference is experienced at the nanoparticle surface; this difference in charge exerts a restoring force. A dipolar oscillation of the conduction electrons is generated with a frequency matching the incident light. Figure reproduced from [247].

suspended in complex external dielectric environments. The quasi-static (or dipole) approximation of the Mie equation was first introduced by Lord Rayleigh to describe plasmons for particles smaller than the wavelength (λ) of incident photons ($\lambda >> 2r$), and is valid for small nanoparticles (e.g. Gold NPs $2r < 25nm$) [118]. Here only the dipole absorption of the Mie equation contributes to the extinction cross-section ($\sigma_{ext} = \sigma_{abs} + \sigma_{sca}$) of the nanoparticles, allowing Mie theory to be reduced to the quasi-static approximation:

$$\sigma_{ext} = \frac{9V\epsilon_m^{3/2}}{c} \frac{\omega\epsilon_2(\omega)}{[\epsilon_1(\omega) + 2\epsilon_m]^2 + \epsilon_2(\omega)^2} \tag{2.3}$$

Where c is the speed of light, ω is the angular frequency of the incident photons, V is the spherical particle volume and ϵ_m is the surrounding medium dielectric constant. The extinction cross section (σ_{ext}) describes loss of energy from the incident beam due to both scattering and absorption.

The dielectric function of the the particle material is denoted as $\epsilon(\omega) = \epsilon_1(\omega) + i\epsilon_2(\omega)$, where $\epsilon_1(\omega)$ and $\epsilon_2(\omega)$ describe the real and imaginary parts of the dielectric constant. Resonance will occur when $\epsilon_1(\omega) \approx -2\epsilon_m$, provided that $\epsilon_2(\omega)$ is small. The extinction cross-section (σ_{ext}) includes a particle size dependence in intensity through the intrinsic dependency of volume on particle diameter.

The dipole approximation however, does not account for the experimentally observed dependence of plasmon bandwidth and absorption peak maxima due to particle size [118]. To account for this, Mie theory is further modified for small particles through the introduction of size dependence into the dielectric function of the metal nanoparticles ($\epsilon(\omega) \rightarrow \epsilon(\omega, r)$). This additional size dependency within the dipole approximation absorption cross-section is known as intrinsic size effect [119], and is introduced once the particle dimensions become smaller than the mean free path (MFP) of the conduction electrons [117][118]. A $1/r$ relationship for plasmon bandwidth is predicted by the Persson et al [184] and is verified experimentally [117][118][136]. Energy and charge is highly localised within the interface for surface plasmons. The

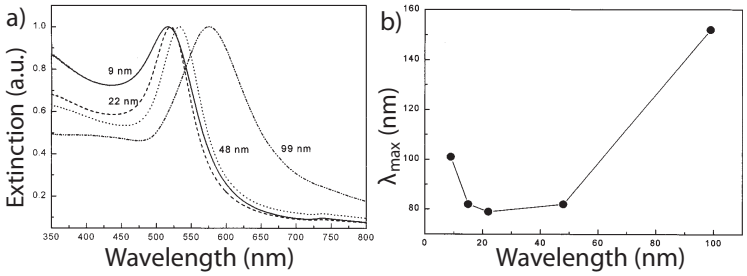


Figure 11: (a) UV-vis absorption spectra of AuNPs with diameters of 9, 22, 48, and 99nm dispersed in water. The absorption spectra are normalized at their peak maxima, 517, 521, 533, and 575 nm. (b) Plasmon bandwidth presented as a function of particle diameter. Image reproduced from [136]

binding of solvent, surfactants and ligands to the NP interface, changes the dielectric properties of the interface resulting in a change of refractive index at the interface, resulting in different surface plasmon properties.

For larger nanoparticles (e.g. for gold $2r > 25nm$) which are still smaller than the wavelength of light ($\lambda >> 2r$) higher-order multipole modes within the Mie equation become important. These higher modes of oscillation (quadrupole and octopole) directly rely on the particle size, with larger particle sizes shifting the the plasmon absorption peak (λ_{max}) to longer wavelengths and wider spectral bandwidths (Table 2). The excitation of higher order plasmon modes is attributed to inhomogenous polarisation of the NP surface as the particle size approaches the wavelength of incident photons.The overall plasmon absorption band is then described by the superposition of all multipole oscillations, each placed at distinct energies.

Diameter (nm)	Standard deviation on diameter (%)	λ_{max}(nm)
8.9	13	517
14.8	12	520
21.7	9	521
48.3	11	533
99.3	11	575

Table 2: Peak plasmon peak λ_{max} for AuNPs with various diameters. Table reproduced from [136]

For nanoparticles in assemblies additional shifts are observed due to electromagnetic coupling between particles. The interactions can be approximated as an ensemble of interacting dipoles. The electrostatic restoring force between the oscillating electrons and the positive nucleus is effected by the charge distribution of adjacent particles (Figure 12). This process leads to a red shifting and broadening of the plasmon resonance for longitudinal modes.

For AuNP aggregates, this electromagnetic coupling between particles is experimentally observed as a red-shift and broadening of the absorption peak, with the magnitude of the shift depending on the particle size,

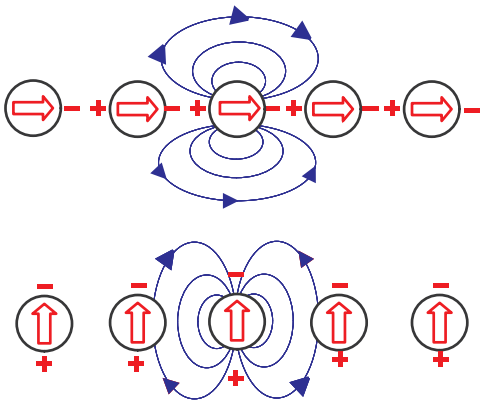


Figure 12: Schematic illustration of near field coupling between metallic NPs in two different polarisations. Diagram redrawn from [146].

aggregate density, fractal dimension, and growth mechanism [222][179] (Figure 14).

2.3.2 *Concentration Estimation (Beer-Lambert Law)*

The concentration of AuNPs can be estimated from UV-VIS spectra provided that the molar extinction coefficient and mean particle diameters are known. Our particle concentrations were estimated using a method presented by Xiong Liu et al [140].

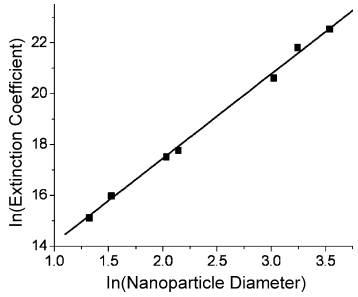


Figure 13: Experimental measurements of natural logarithm of extinction coefficients vs logarithm of average nanoparticle core diameters. Reproduced from [140].

Xiong Liu et al demonstrated a linear relationship between the logarithms of extinction coefficients (ε) and core diameters of gold particles (D):

$$\ln \varepsilon = K \ln D + a \tag{2.4}$$

where k and a are experimentally obtained constants of values 3.32 and 10.8 respectively. The extinction (ε) is obtained from the absorbance at 506nm (from a UV-VIS absorption spectra). Note that the used extinction coefficient (ε) has units of $M^{-1}cm^{-1}$, while the particle diameter (D) is measured in nanometers (Figure 13).

For their calculations, the AuNP core sizes were obtained using high resolution TEM and converted to a mean volume, the concentrations

were calculated from synthesis ingredients (the assumption was made that reduction from gold(III) to gold atoms was 100% complete) and the sample absorption was obtained using UV-VIS absorption spectroscopy. Xiong Liu et al observed this relationship to hold for gold particle stabilised using citrate, oleylamide and decanethiol and demonstrated to be independent of particle capping ligands, enabling an effective rule-of-thumb to estimate nanoparticle concentration.

2.3.3 *Quantification of aggregation*

A/D ratio

The onset of AuNP aggregation, introduces a red-shift and broadening of the absorption peak [222][179]. The most common approaches to characterising the extent of aggregation is to measure the position of the absorption peak or to take the absorption at a single wavelength [175]. Both these approaches do not reveal any information about peak broadening. Locating the precise position of the absorption peak can be tricky and the absorption at a singe wavelength is sensitive to peak shift.

The Aggregate/Dispersed ratio (A/D ratio) is defined as the ratio of the integrals of the Aggregate region (A) to the Dispersed region (D). The A/D ratio first described by Laromaine et al [122], defines the Dispersed region as 490<D<540 and the Aggregate region as 550<A<700 for 10nm AuNPs, representing the primary absorption band of the particles when dilute and dispersed (Figure 14). As it is a ratio, it is insensitive to sample concentration and has no units. The technique is similar to the B/A ratio used by Chowdhury et al, differing only in the choice of integration regions (490<A<540 and 570<B<750) [40].

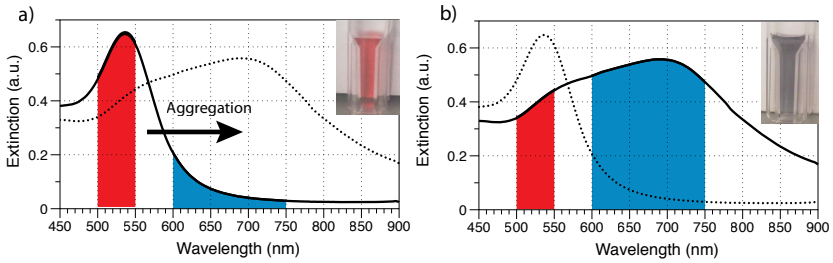


Figure 14: Schematic illustration of the A/D ratio and the influence of particle aggregation on the A/D ratio. The spectra in a) and b) show the change in the A/D ratio for dispersed and aggregated 20nm particles. The area in red is denoted D (dispersed) and corresponds to the integral under the spectrum between 500 and 550 nm. The area in blue is denoted A (aggregated) and corresponds to the integral under the spectrum between 600 and 750 nm. The top inserts display the particles in a cuvette when a) dispersed and b) aggregated.

Choice of integration regions

The magnitude and extent of red-shift and broadening of the absorption peak changes depending on particle size with larger particles displaying larger shifts. For 20 and 40nm AuNPs the integral regions for the A/D ratio were modified to reflect the absorption band locations. For 20nm AuNPs the Dispersed region was chosen as 500<D<550 and the Aggregate region as 600<A<750. For 40nm AuNPs the Dispersed region

was chosen as 500<D<550 and the Aggregate region as 700<A<850. For consistency, the integral regions for 10nm AuNPs were kept the same as described by Laromaine et al [122] (i.e. 490<D<540 and 550<A<700). These integration regions are illustrated in Figure 15.

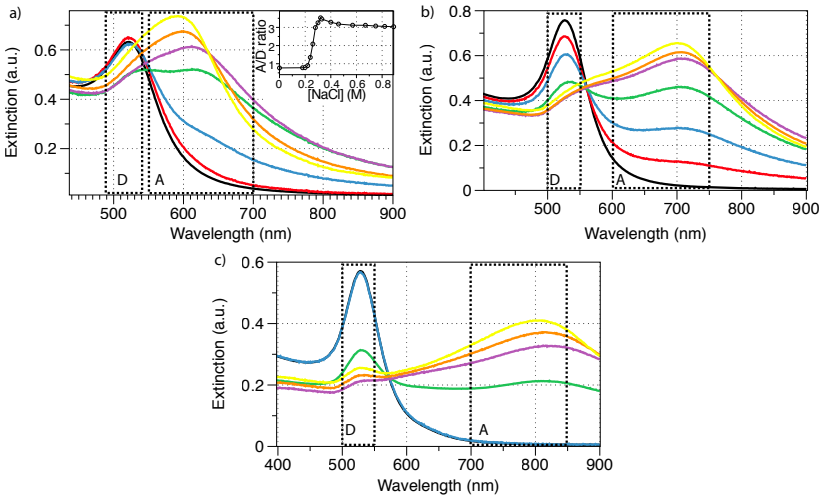


Figure 15: Illustration of A/D integration regions for a) 10nm b) 20nm and c) 40nm AuNPs functionalized with BSPP. The AuNPs are aggregated with increasing concentrations of NaCl, resulting in a range of absorption spectra. The integral regions for the A/D ratios are highlighted in dashed boxes. Insert in a) displays the calculated A/D ratio of 10nm AuNP absorption spectra as a function of NaCl concentration.

Comparison of A/D ratio with absorbance at single wavelength

The effectiveness of the A/D ratio for characterising AuNP aggregation was compared with single wavelength absorption measurements. The UV-VIS absorption spectra for NaCl stability assays performed on 10nm AuNPs are presented in Figure 16. The surface of the AuNP is functionalized with either citrate, BSPP or BSPP Fmoc-GFC (See chapter 4). The use of different surface ligand, alters the particle stability in solution with respect to salt concentration, affecting the salt concentration at which particles begin to aggregate. The A/D ratio and the absorbance at 625nm were used as methods of quantifying the extent of aggregation (Figure 17). Smoother and sharper transitions upon aggregation are observed when using the A/D ratio, compared to single wavelength absorption measurements.

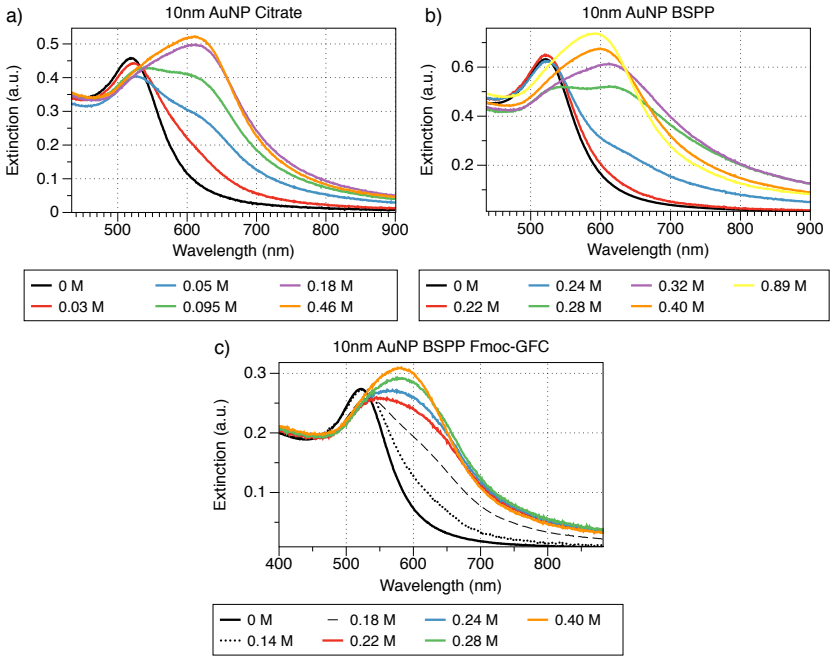


Figure 16: Salt stability assays of 10nm AuNPs functionalized with a) citrate b) BSPP c) BSPP Fmoc-GFC. The UV-VIS absorption spectra are recorded as a function of solution NaCl concentration.

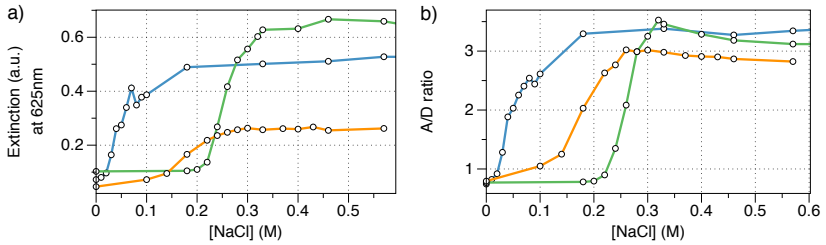


Figure 17: Salt stability assays of 10nm AuNPs functionalized with citrate (blue), BSPP (green) and BSPP Fmoc-GFC (orange) described using a) the absorbance at 625nm b) A/D ratio. The A/D ratios and absorbance at 625nm is calculated from the spectra presented in Figure 16 .

2.4 TRANSMISSION ELECTRON MICROSCOPY (TEM)

Transmission electron microscopy is a powerful technique, providing high-resolution 2D structural information on electron rich nanomaterials. As a result it is routinely used for obtaining structural information on colloidal systems (particle size, shape and assembly structure) and can often provide analysis of internal structure such as chemical composition and crystallographic information.

In TEM a focused electron beam is passed through a thin specimen, with the scattered beam focussed and magnified to form an image. The technique offers a high theoretical resolution (~0.5nm), however typically resolvable objects tend to be around ~5nm. Statistical data can be built up by counting individual particles' surface area or diameters to form particle size distributions. The main limitation of the technique is the necessity of sample drying and immobilisation for imaging. The necessity of ultra high vacuum for measurements, requires the the removal of solvent, collapsing the 3D structure of AuNP assemblies and

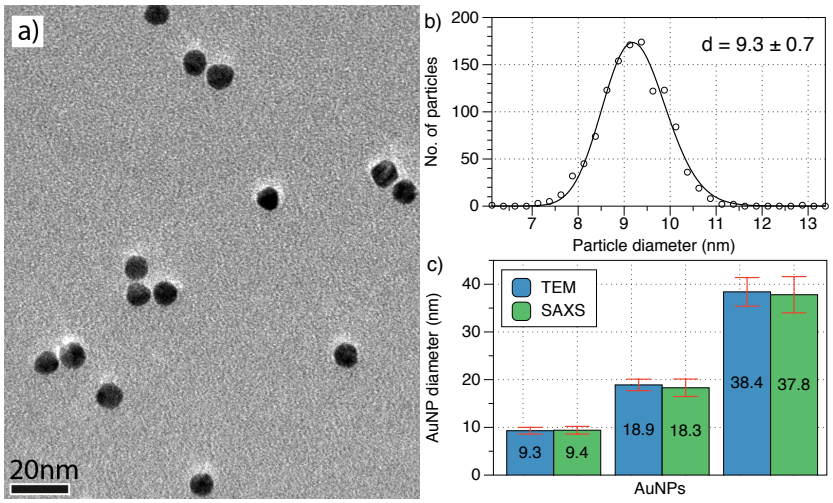


Figure 18: Comparison of particle diameters obtained using TEM and SAXS a) TEM micrograph of citrate coated AuNPs b) histogram of 500 particles from population shown in (a). The histogram is fitted with a lognormal distribution with a mean diameter of 9.3nm and standard deviation of 0.7nm. c) Comparisons of AuNP diameters measured using TEM and SAXs. Three different particle size populations of approximately 9, 18 and 38nm in diameters were characterised.

altering aggregate morphology. Additionally, materials of low electron density such as AuNP capping ligands are not visible under TEM.

Samples were prepared by placing ~10uL of colloidal solution onto Formvar carbon coated grids and leaving the solution to settle for ten minutes. Afterwards, excess fluid was removed using absorbent paper. A Joel 2010 TEM with a built in digital CCD camera was used to obtain images of AuNPs, with at least 200 particles counted to obtain sufficient statistical accuracy. ImageJ (National Institute of Health) was used to measure the particle surface area; assuming a spherical shape this was converted to mean particle diameters allowing a histogram of particle diameters to be compiled. This histogram was fitted with a Log-Normal distribution to yield a median particle size and standard deviation (Figure 18). Good agreement is observed between the particle sizes measured via TEM and SAXS; this close agreement between TEM and SAXS particle sizes has been demonstrated in literature [197][70][23].

2.5 SMALL ANGLE X-RAY SCATTERING (SAXS)

Whilst the high electron density of metallic NPs provides an advantage, SAXS can be used to study biomaterials, such as proteins, where the difference between the analyte and buffer electron density is smaller

Small Angle X-ray scattering is a powerful technique for the characterisation of particle size, shape, polydispersity and assembly structure. The high intensity of modern synchrotron sources, combined with the high electron density contrast of metallic NPs, allows for fast, sensitive, in-situ synchrotron measurements. The following section summarises important features and aspects of SAXS data analysis and model fitting, detailed derivations are readily available in many books [135][69][75][60]. A highly recommended manual for small angle scattering written by Dr Hammounda, can be found on the NIST SANS website [77].

A schematic illustration of the essential components found within a SAXS beamline is presented in Figure 19. A sample is illuminated

with a coherent monochromatic x-ray beam of wavelength (λ) and the angular dependent scattered intensity is recorded.

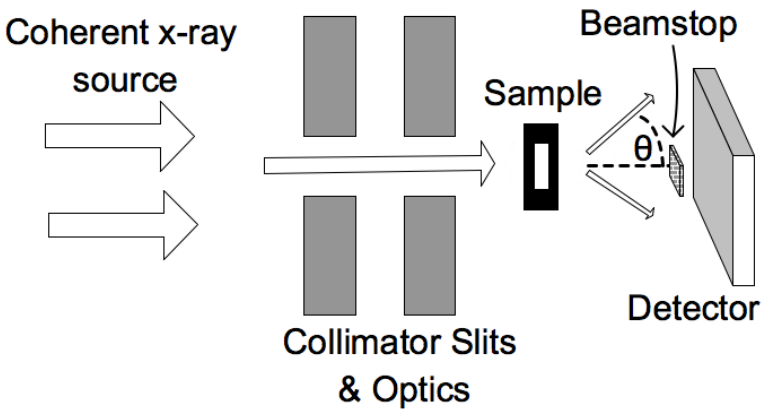


Figure 19: Essential components of a Small Angle X-ray Scattering system

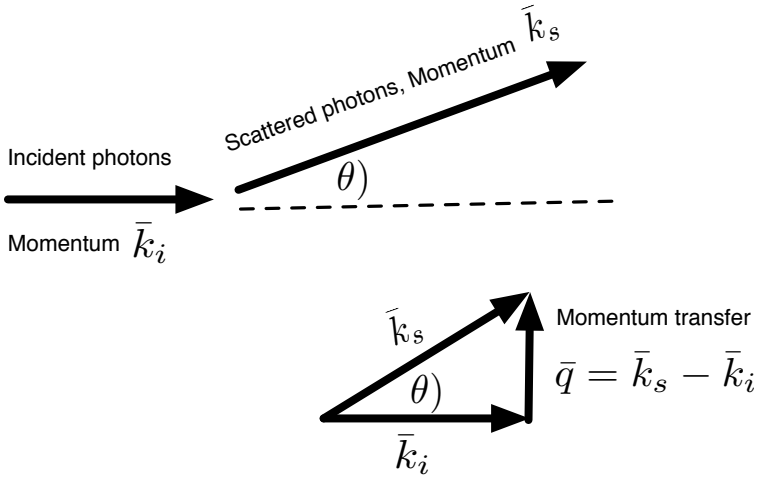


Figure 20: Schematic representation of momentum transfer vector $\bar{q}$

This angular dependent scattered intensity contains information on the spatial distribution of scatters, enabling the calculation of scatterer size, shape and structure. The scattered intensity is recorded on a 2D detector; the image is then integrated via an arc integral into a 1D plot of $I(q)$ vs q. The momentum transfer vector $\overline{q}$ describes the difference between the incident $\bar{k}_i$ and scattered $\bar{k}_s$ wave vectors $\overline{q} = \bar{k}_s - \bar{k}_i$, and has magnitude $q = |\overline{q}| = \frac{4\pi}{\lambda}\sin(\theta/2)$, where θ is the scattered angle (Figure 20). The use of the momentum transfer vector $\overline{q}$ (rather then θ) for scattering experiments enables the comparison of data taken at different beamlines.

During the process experiment, the incident beam of photons with momentum $\hbar\bar{k}_i$, is scattered by the sample within the solid angle Ω, with momentum $\hbar\bar{k}_i$ (Figure 21). The scattered photons are collected by a detector at distance $\overrightarrow{r}$ from from the sample. The detector counts all the particles arriving within a solid angle dΩ. From this the scattering differential cross-section $\frac{d\sigma}{d\Omega}$ represents number of photons scattered into a unit solid angle for distance $\overrightarrow{r}$ per second divided by the flux

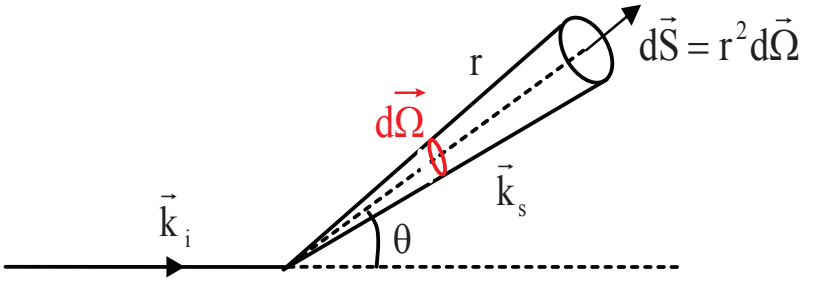


Figure 21: Representation of photons scattered into solid angle dΩ for scattering angle θ. Image redrawn from [77].

of the incident beam. The integral of this differential scattering cross-section, provides the microscopic scattering cross section $\sigma_s = \int \frac{d\sigma_s}{d\Omega} d\Omega$. SAXS data is often converted to an absolute differential cross section ($\frac{d\Sigma}{d\Omega}$), which is independent of instrumental setup and sample volume (V). This is given as $\frac{d\Sigma}{d\Omega} = \frac{1}{V}\frac{d\sigma}{d\Omega}$.

The differential scattering cross-section ($\frac{d\Sigma}{d\Omega}$) contains information describing system structure and the interactions and is often denoted as I(q). Normalisation of sample scattering to $\frac{d\Sigma}{d\Omega}$ is often required for quantitative measurements; pure water is often used as a calibrant, with $\frac{d\Sigma}{d\Omega} \sim 1.6 \times 10^{-3} mm^{-1}$ at 25°C [135].

Hence for the experiment depicted in figure 19, the scattered photon intensity per unit area per unit time I_s can be described in terms of the absolute differential cross section:

$$I_s = I_0 \varepsilon T_r \Delta\Omega A_s L_s \frac{d\Sigma}{d\Omega} \tag{2.5}$$

Where:

T_r	sample transmission
A_s	beam cross-section
L_s	sample thickness
I_0	Incident photon intensity
$\frac{d\Sigma}{d\Omega}$	Absolute differential scattering cross section
ε	detector efficiency
$\Delta\Omega$	solid angle subtending a detector element

2.5.1 *The Fourier relation of structure to scattered X-ray intensity*

The Fraunhofer approximation of scattering theory relates real space (r) and reciprocal space (q) through an integral transform known as the Fourier transform. The n dimensional Fourier transform of h(r) is defined by:

$$F_n(h)(q) = \int h(r) exp(iq.r) d^n r \tag{2.6}$$

and the inverse Fourier transform defined by:

$$F_{-n}(H)(r) = \left(\frac{1}{2\pi}\right)^n \int H(r) exp(iq.r) d^n q \tag{2.7}$$

The electron density distribution within a sample $\rho(r)$ and the scattering amplitude A(q) are related by a 3D complex Fourier transform in reciprocal space. The measured scattered intensity $\frac{d\Sigma}{d\Omega}$ is obtained through taking the square of the absolute amplitude.
$\frac{d\Sigma}{d\Omega} = \mid A(q) \mid^2$
Here A(q) describes the coherent sum of the scattering amplitudes arising from individual scatterers within an illuminated object. It is described by the Fourier transform of the electron density distribution $\rho(r)$ within the material:

$$A(q) = F(q) = \int_v \rho(r) e^{iq.r} dV \tag{2.8}$$

The measured particles are spatially and orientationally averaged, the Fourier transform (equation 2.8) can be reduced to a one dimensional form:

$$F(q) = 4\pi \int_0^\infty \Delta\rho(r) \frac{sin(qr)}{qr} r^2 dr \tag{2.9}$$

2.5.2 *Experimental setup at the Australian synchrotron*

SAXS measurements were performed at the SAXS/WAXS beamline at the Australian Synchrotron. A solid state CMOS detector (1M Pilatus detector) was used to capture the angular dependent scattered intensity (I(q)), with a beamstop used to prevent direct exposure of the detector to the x-ray beam. A 10Kev beam (λ=1.2Å) was chosen to minimise water scattering. The beam size at the specimen is approximately (FWHM) 250 - 700 µm horizontal, 40 – 500 µm vertical at full flux. Liquid samples were measured inside 1.5mm (diameter) quartz capillaries (Figure 22); the fluid was oscillated within the capillary, so as to reduce radiation damage to the sample. One second exposure times were observed to be sufficient for good scattering data; multiple exposures (~10) were acquired, checked for consistency and then averaged to reduce noise. The capillary thickness was observed to fluctuate (~5%), necessitating new background measurements upon capillary replacement or movement. The captured data were corrected for transmission, beam intensity, detector response, background scattering, exposure time and normalised to an absolute scale using Millipore water. Silver behenate was used as a q space calibrant [85].

The exceptional high flux (Beam flux up to 10^{13} photons/s), low noise experimental setup at the australian synchrotron enabled the capture of fast high quality measurements from dilute weakly scattering samples. Figure 24 demonstrates the scattered intensities and backgrounds of 9.4nm AuNPs, 18.3nm AuNPs, 5.9nm CdSe quantum dots and 1.3nm AuNPs. For strongly scattering samples such as the 9.4nm and 18.3nm AuNPs, the experimental scattered intensity is considerably larger than the background. Background subtraction reveals fine detail (oscillations)

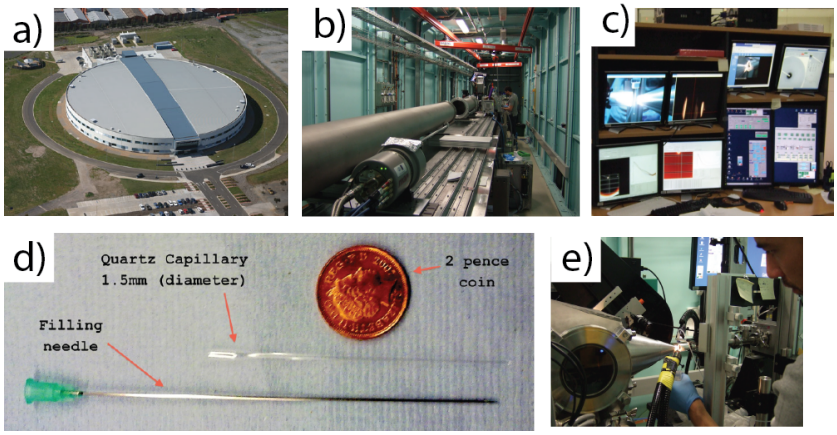


Figure 22: Experimental facilities at the Australian SAXS/WAXS beamline. a) Birds eye view of Australian synchrotron; b) view inside experimental hutch; c) external control unit; d) quartz capillary and filling needle; e) sample holder.

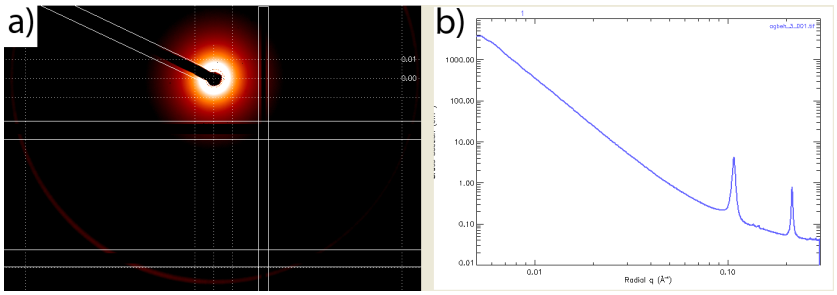


Figure 23: Reduction of SAXS data using beamline software. a) Captured scattered intensity from silver behenate, the image is masked to remove artefacts from camera setup and beamstop scattering. b) Sector integral of captured scattered intensity, the visible peaks are characteristic of silver behenate.

at high q, arising from the spherical nature of the particles. For weakly scattering samples (CdSe quantum dots and 1.3nm AuNPs) accurate background subtraction is essential. For example the spherical form factor of 1.3nm AuNPs could be measured at concentrations as low as 10.6 μg/ml (1 μM) and structural information obtained from JR2EC$_2$-KC$_2$ protein fibers at concentrations of 0.1mM (Figure 42). SAXS data reduction was performed using SAXS15ID in an IDL environment (Figure 23), with modelling and fitting carried out using the Irena macros implemented in Igor Pro [90].

2.5.3 *Scattering from a colloidal system*

Analysis of the differential scattering cross-section ($\frac{d\Sigma}{d\Omega}$) for colloidal systems, can be performed using model dependent and model independent methods. Model independent approaches (Guinier, Porod, Kratky) have the advantage of being fast to fit and require less a-priori assumptions about the nature of the system (i.e. particle shape and size). Model based approaches (form factor and structure factors), require additional assumptions about the system morphology (particle shape, material composition) but enable more characteristics to be extracted.

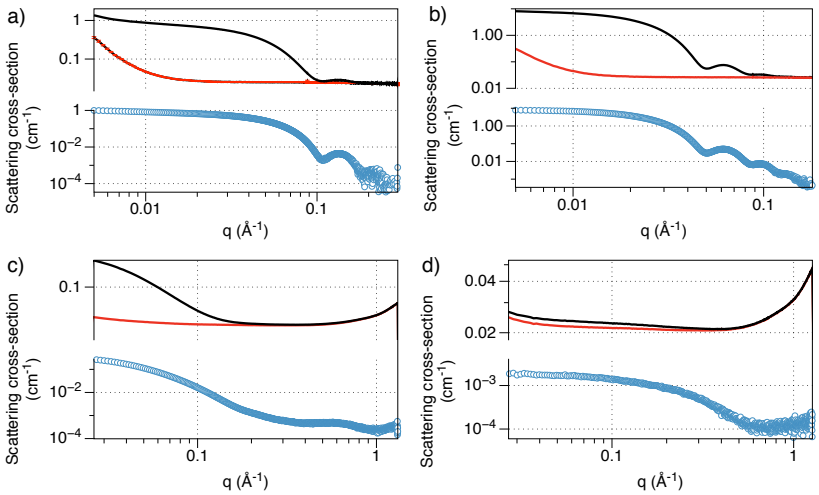


Figure 24: Importance of accurate background subtraction for SAXS data. The experimental Scattered Intensity (black), experimental background (red) and reduced differential scattering cross-section (blue) for a) 9.4nm AuNPs b) 18.3nm AuNPs c) 5.9nm CdSe quantum dots d) 1.3nm AuNPs. The differential scattering cross-section (blue) is obtained by subtracting the experimental background (red) from the measured scattered intensity (black). Accurate background subtraction is critical for dilute weakly scattering samples.

For a colloidal nanoparticle sample, Guinier fits enable a quick estimate of particle radius of gyration, whilst the fitting of a shape form factor enables the calculation of analyte size and polydispersity for a range of geometric shapes. The form factor can be made to fit the entire data set, whereas the Guinier fit is restricted to the low q regions in the data ($qR_g < 1$).

2.5.4 *Guinier and Porod fits*

SPHERICAL PARTICLES The radius of gyration describes the root mean square distance of the object's parts from its centre and is analogous to the radius of inertia. It is obtained from the second moment of $\rho(r)$:

$$R_g^2 = \frac{\int \Delta\rho(r) r^2 dr}{2\int \Delta\rho(r) dr}$$

Using the Taylor expansion of sin(x), equation 2.9 can be approximated as follows:

$$\sin(qr) = qr - \frac{(qr)^3}{3!}\ldots$$

$$\text{hence } \frac{\sin(qr)}{qr} = 1 - \frac{(qr)^2}{3!}\ldots$$

$$I(q) \sim |F(q)|^2 = 4\pi \int_0^\infty \Delta\rho(r) r^2 \left[1 - \frac{(qr)^2}{3!} + \ldots\right] dr$$

$$I(q) \sim V_p \left[1 - \frac{(qR_g)^2}{3} + \ldots\right] = V_p \exp\left(-q^2 R_g^2/3\right)$$

Hence the scattering from suspended non-interacting spherical particles, can be described using the Guinier approximation which provides an estimate of particle radius of gyration R_g.

$$I(q) \sim \exp\left(-q^2 R_g^2/3\right) \tag{2.10}$$

A plot of $Ln(I(q))$ vs q^2, yields a straight line with a gradient of $-R_g^2/3$, with the radius of gyration (R_g) related to the radius of spherical particles (R_{sphere}), by $R_g = \sqrt{3/2}R_{sphere}$. This approximation is only valid for $qR_g < 1$.

ROD SHAPED PARTICLES For Rod shaped particles and fibers, the Guinier approximation is modified to provide the radial cross-section (R_c) $I(q) \sim exp\left(-q^2R_c^2/2\right)$. Here the cross-sectional radius ($qR_c < 1$) is assumed to be much smaller then the total length of the Rod (L) ($qL > 1$) [245]. The radial cross-section is used to characterise protein fibers in section 3.2.3.

FRACTAL DIMENSION (POROD FITS) For the limit $qR_g < 1$, scattering probes the particle interface, leading to the logarithmic scattering ($I(q) \propto q^{-D_f}$) commonly observed in scattering from particulate systems and networked polymers. Fitting the slope of the linear regions on a log(I) vs log(q) plot (also called a Porod fit) provides an estimate of the fractal dimension D_f of an aggregate (Figure 25) [150][111][69][94]. Fractal dimensions (D_f) with values between $1 \leqslant D_f \leqslant 3$ indicate the formation of mass fractals, where D_f describes the aggregate mass (M) scaling with aggregate size (Rg) i.e. ($M \sim R_g^{D_f}$) [147][179]. Mass fractals typically demonstrate a branched structure which becomes more dense with higher values of D_f [209][94]. Values of $3 \leqslant D_f \leqslant 4$ indicate the presence of surface fractals, with rough surfaces exhibiting $D_f \sim 3$ and smooth surfaces higher a $D_f \sim 4$, as illustrated in Figure 26.

$$I(q) \propto q^{-D_f} \begin{cases} D_f = 4 & \text{Sharp Interface} \\ 3 < D_f < 4 & \text{Surface Fractal} \\ 1 < D_f < 3 & \text{Mass Fractal} \end{cases}$$

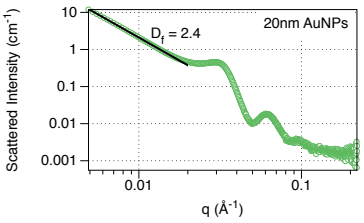


Figure 25: Example of Porod fit. Scattered intensity (green) of $JR2EC_2$ modified 18.3nm AuNPs, assembled with 0.1 μM $JR2KC_2$ (Chapter 3). The gradient of the logarithmic scattering at low q is fitted yielding a fractal dimension of D_f = 2.4

The mass distribution of aggregates is known to be intimately linked to their aggregation kinetics allowing for comparisons with colloidal models, such as diffusion limited colloidal aggregation (DLCA) ($D_f \sim 1.8$), reaction limited colloidal aggregation (RLCA) ($D_f \sim 2.1$) and compact clusters ($D_f \sim 3$).

Diffusion limited cluster-cluster aggregation (DLCA) and Reaction-limited cluster-cluster aggregation (RLCA) are two classes of irreversible (i.e. permanent) kinetic colloid aggregation derived on the assumptions of particle diffusion, mobility and sticking probability (Figure 27). For DLCA, nanoparticles are assumed to affix whenever they collide result-

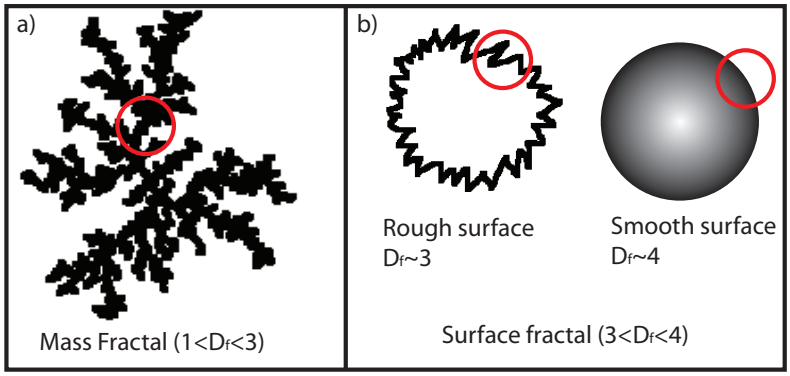


Figure 26: Illustration of mass and surface fractals

ing in fast forming branched aggregates. For RLCA, a barrier to sticking is introduced such that a multitude of collisions are needed for permanent sticking leading to slower forming but denser aggregates. Hence higher particle mobility leads to denser aggregates with higher fractal dimensions. For aggregates where particle sticking is non-permanent, the particulate subunits are able to dynamically rearrange into denser, energetically favourable structures, with higher fractal dimensions such as compact clusters [179]. Note, that for aggregates formed from particulate subunits, provided that there is sufficient q range, it may be possible to see two different fractal regions, one corresponding to the particulate subunit and one to the whole aggregate.

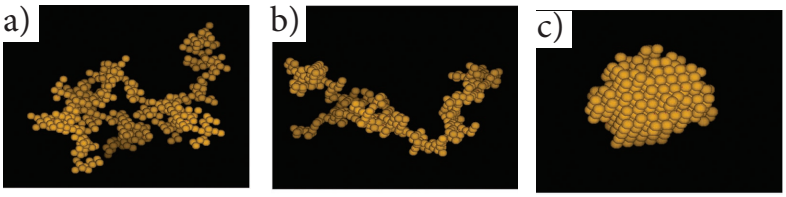


Figure 27: Structure of nanoparticle clusters composed of 400 particles a) a Reaction-limited cluster-cluster aggregate; b) a Diffusion-limited cluster-cluster aggregate; c) a Compact cluster. Reproduced from [179]

UNIFIED FIT The Guinier and Porod regions can be fitted simultaneously using a unified fit function. The scattering is modelled assuming several structural levels, with each level considered to be composed of a combination of a Guinier exponential and a Porod power law [17, 19, 18][20][90]. The toolset implemented in the Irena macros enables the fitting of up to five independent structural levels (n=5):

$$I(q) = F_B + \sum_{i=1}^{n} S_i(q)(G_i \exp\left(\frac{-q^2 R_g^2}{3}\right) + B_i \exp\left(\frac{-q^2 R_{gcf}^2}{3}\right)$$

$$\times \left\{ \frac{\left[\operatorname{erf}\left(\frac{qR_g}{\sqrt{6}}\right)\right]^3}{q} \right\}^{P_i})$$

where the index 'i' represents each structural level. For each structural level, G_i is the exponential pre-factor, R_g the radius of gyration, B_i the power-law pre-factor, erf the error function and P_i the Porod constant. A flat background can accounted for by introducing an optional F_B. When multiple structural level are modelled, the power law has to be cut off at high q; this is achieved by setting a cut-off radius R_{gcf}. The unified fit parameters are optimised using Levenberg-Marquard least squares fitting. The ability to simultaneously fit guinier and porod regions provides an a powerful a-priori method for data analysis, prior to fitting more complicated models, which are able to extract more structural information from a sample.

2.5.5 *Kratky*

Kratky plots ($I(q)q^2$ vs q) are commonly used for providing an indication of protein folding state [52]. A characteristic peak at low q is indicative of folded globular proteins, whilst unfolded proteins display an extended rise in $I(q)q^2$ with q (Figure 28). Flexible multi-domain proteins, demonstrate a combination of these features [153].

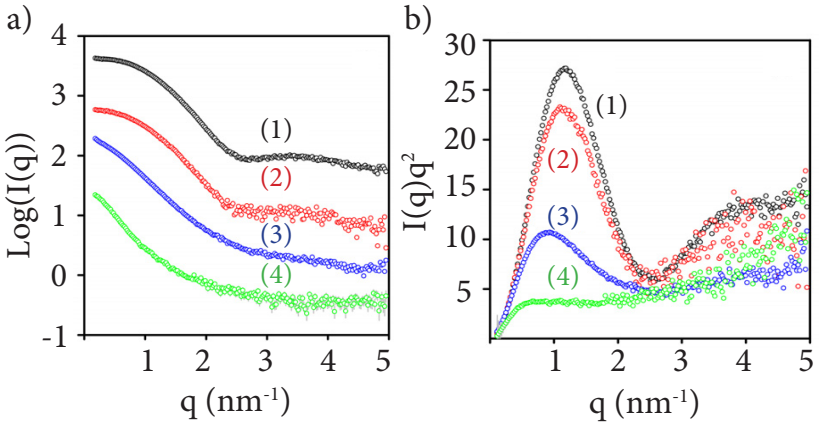


Figure 28: Application of Kratky plot to protein samples. a) SAXS intensities and b) Kratky plots for lysozyme samples, demonstrating (1) folded protein, (2) partially unfolded protein (in 8M urea) (3) partially unfolded protein (at 90°C) and (4) unfolded lysozyme (in 8 M urea at 90°C). Data and graphs reproduced from [153]

2.5.6 *Pair distribution function*

The pair-distribution function P(r) is a probability histogram describing the electron density weighted intramolecular distances within an analyte. It describes the probability of finding two scattering objects at a certain distance, within an analyte [135][28]. Whilst the scattered intensity has reciprocal units (i.e. $Å^{-1}$), the pair-distribution function provides structural information in real space and can be compared with calculated models (such as spheres, cylinders, cubes etc). This representation in real space is more intuitive for shape estimation by simple visual inspection than the reciprocal space of the scattered intensity. An indirect inverse Fourier transformation of the scattered intensity is performed using a program (e.g. Gnom, Irena Macros) to generate a P(r) histogram:

$I(q) = 4\pi \int_0^{D_{Max}} P(r) \frac{\sin(qr)}{qr} dr$
where formally
$P(r) = \frac{r^2}{2\pi^2} \int_0^{\infty} q^2 I(q) \frac{\sin(qr)}{qr} dq$
and D_{Max} is the maximum distance present within the scattering particle. The theoretical scattered intensities for several geometric shapes and their corresponding pair-distribution functions are presented in Figure 29. The function can be used to calculate a radius of gyration (R_g) and with sufficient modelling be used to generate low resolution shape envelopes of analytes, using programs such as GASBOR, DAMMIN and SASHA. The P(r) is heavily used in analysis of protein SAXS data, however the technique is prone to generating artefacts if backgrounds are not correctly subtracted.

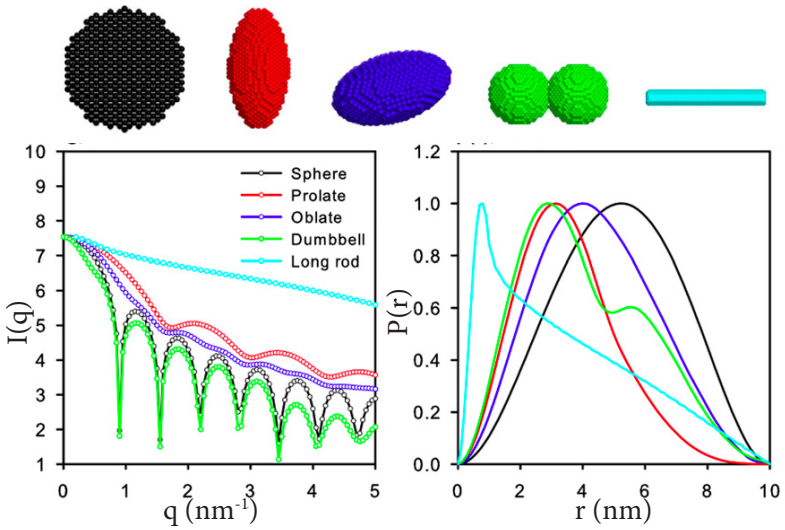


Figure 29: Scattered intensity I(q) and corresponding pair distribution function P(r) for different geometrical shapes: Sphere (black), prolate ellipsoid (red), oblate ellipsoid (blue), dimer (green) and cylinder (cyan). Figure reproduced from [153].

2.5.7 *Scattering from polydisperse populations of particles*

For polydisperse systems consisting of n distinct particle populations, the differential scattering cross-section ($\frac{d\Sigma}{d\Omega}$) can be written as a linear combination of the scattering contribution from each 'i' population:

$$\frac{d\Sigma}{d\Omega} = I(q) = \sum_{i=1}^{n} I_i(q) = \sum_{i=1}^{n} N_i S_i(q) P_i(q) \tag{2.11}$$

Where the index 'i' denotes a distinct particle population, n is the total number of distinct particle populations, N_i is the number density (number of particles per unit volume), $P_i(q)$ is the particle form factor and $S_i(q)$ the structure factor. The particle form factor $P_i(q)$ describes the particle shape and polydispersity, whereas the structure factor $S_i(q)$ describes the interference due to inter-particle interactions. In the absence of particle interactions, the structure factor has a value of unity ($S_i(q) = 1$). By this method, the contribution to scattering of each

particle population is summated to generate the differential scattering cross-section.

Spherical form factor $P_i(q)$

The form factor $P_i(q)$ describes the ensemble-averaged shape of scattering objects in solution. For the particle population 'i' with a size distribution $\Psi_i(r)$, it can be written as:

$$P_i(q) = \Delta\rho_i^2 \int_0^\infty V_p^2 \left[F_i(q,R)\right]^2 \Psi_i(R)\,dR \tag{2.12}$$

Where $F_i(q,R)$ is the shape function, $\Delta\rho^2$ is the relative scattering length density squared and $V_p = \frac{4}{3}\pi R^3$ is the volume of an individual particle. The relative scattering length density squared $\Delta\rho^2$ is a contrast term that describes the difference between the particle and solvent electron densities:

$\Delta\rho = \rho_{particle} - \rho_{solvent}$ and $\rho = \frac{n_e d_M N_A r_e}{M_w}$

Where d_M is the mass density, n_e is the number of electrons in a molecule, N_A is the Avogadro number, M_W is the molar mass and r_e is the Thomson scattering length (equal to the classical electron radius 2.818×10^{-15}m). A list of the scattering length densities of water, gold, ZnS and CdSe are presented in Table 3. These values were calculated using the IRENA contrast calculator, which implements the Cromer-Liberman code and cross-section tables to calculate X-ray atomic scattering factors for the beam energy of 10keV [45][46][15].

Sample	Density (g/cm3)	ρ_{sample} ($\times 10^{10}$cm^{-2})	$\Delta\rho^2 = \left(\rho_{sample} - \rho_{H_2O}\right)^2$ ($\times 10^{20}$cm^{-4})
Water	1	9.42	NA
Gold	19.3	131.4	1.487×10^4
ZnS	3.98	31.88	504.6
CdSe	5.81	42.25	1078

Table 3: The scattering length densities of water, gold, ZnS and CdSe calculated using the Irena macros [90] and physical constants obtained from the CRC handbook of chemistry and physics [131]. The scattering length densities are necessary for particle concentration calculations and application of core-shell models.

SPHERICAL SHAPE FUNCTION $f_i(q,r)$ For a spherical particle of radius R, the integration of equation 2.9, leads to the particle shape function $F_i(q,R)$:

$$F_i(q,R) = \frac{2\left[\sin(qR) - qr\cos(qR)\right]}{(qR)^3} \tag{2.13}$$

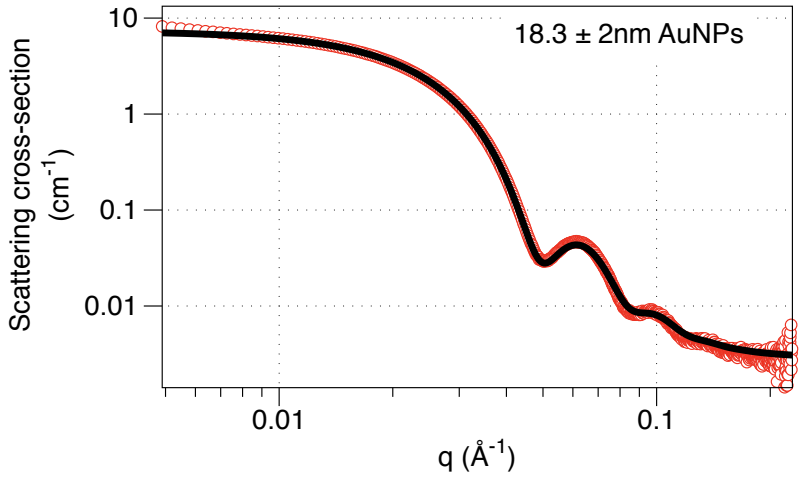


Figure 30: SAXS profile of AuNPs (red) fitted with a spherical form factor assuming a log normal distribution (black) with a mean size of 18.3±2 nm.

When incorporated, the form factor $P_i(q)$ for a spherical particle becomes:

$$P_i(q) = \Delta\rho_i^2 \int_0^\infty V_p^2 \left[\frac{2\left[\sin(qR) - qr\cos(qR)\right]}{(qR)^3}\right]^2 \Psi_i(R)dR \qquad (2.14)$$

Figure 30 displays AuNPs fitted with a spherical formfactor assuming a log normal distribution, the particle polydispersity is calculated from fitting the formfactor minima at high q.

CORE-SHELL FORM FACTOR For a spherical particle, with a core-shell morphology, the shape function has to take into account the contrast difference between layers within the particle (Figure 31). Hence the form factor is modified as follows:

$$P_i(q) = \Delta\rho_i^2 \int_0^\infty [V_p(R + r_{shell})(\rho_{shell} - \rho_{solvent})F_i(q, R + r_{shell})$$

$$+V_p(R)(\rho_{core} - \rho_{shell})F_i(q, R)]^2\Psi_i(R)dR \qquad (2.15)$$

Where ρ_{core}, ρ_{shell} and $\rho_{solvent}$ are the scattering length densities of the particle, core shell and surrounding solvent.

SIZE DISTRIBUTIONS $\Psi(r)$ Most scattering systems display a range of sizes and can be best described by a size distribution $\Psi_i(R)$ such as Gaussian or Log Normal. The size distributions $\Psi_i(R)$ are required to

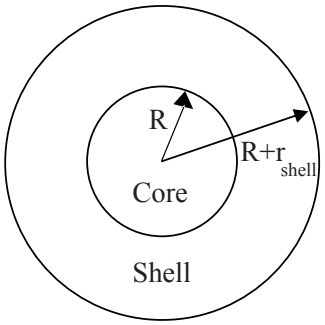


Figure 31: Schematic representation of core-shell model

normalise such that $\int_0^\infty \Psi_i(R)dR = 1$ and can be related to the particle volume fraction ϕ_i by:

$$\phi_i = N_{iT} \int_0^\infty V_p(r)\Psi_i(R)dR \tag{2.16}$$

Where N_{iT} is the total number of scattering particles in population 'i'. Both Gaussian and Log Normal distributions are commonly used to fit AuNP size distributions; a detailed comparison of Gaussian, Log Normal and Schulz distributions applied to SAXS measurements is compiled by Bienert et al [23].

Gaussian distribution The gaussian distribution can be written as

$$\Psi_i(R) = \frac{1}{\sigma\sqrt{2\pi}} \exp\left[-\frac{(R - R_{mean})^2}{2\sigma^2}\right] \tag{2.17}$$

where σ is the standard deviation and R_{mean} is the mean radius.

Log Normal distribution The Lognormal distribution is similar to the gaussian, but uses the variable ln(R) instead of R and is written as

$$\Psi_i(R) = \frac{1}{\sigma R\sqrt{2\pi}} \exp\left[-\frac{(\ln(R) - \mu)^2}{2\sigma^2}\right] \tag{2.18}$$

where σ is the shape function and $\mu = \ln(R_{med})$ is the natural log of the median radius. The corresponding mean averages are:

Mean radius	$R_{mean} = \exp\left(\mu + \frac{\sigma^2}{2}\right)$
Standard deviation on mean	$\sigma_{mean} = \exp\left(\mu + \frac{\sigma^2}{2}\right)\sqrt{e^{\sigma^2} - 1}$
Mean volume	$V_{mean} = \frac{4\pi}{3}\exp\left(3\mu + \frac{9}{2}\sigma^2\right)$
Distribution peak	$R_{peak} = e^{\mu - \sigma^2}$

Spherical formfactors were observed to fit AuNP populations more closely using a Log normal distribution rather than a Gaussian one, although both produced similar means for low standard deviations

(<10%). TEM size histograms were also observed to conform more closely to a Log normal than a Gaussian, with particle sizes obtained from both SAXS and TEM agreeing closely (Figure 18).

2.5.8 *Structure factor S(q)*

The introduction of inter-particle interactions introduces an interference term. This interference term can be described by the structure factor S(q):

$$S(q) = 1 + 4\pi N \int_0^\infty (g(r) - 1) \frac{\sin(qr)}{qr} r^2 dr \tag{2.19}$$

where $g(r)$ is the radial pair correlation function, which describes the probability of finding a particle at a distance r from another particle. The structure factor is the Fourier transform of the total correlation function $h(r) = g(r) - 1$. For the absence of inter-particle interactions, $S(q) = 1$. If the analyte form factor P(q) is known, e.g. from the scattering from dilute (unaggregated) samples, the structure factor S(q) can be obtained by dividing the scattering from aggregates by the scattering from dilute particles (Figure 32). As the structure factor S(q) is purely determined by inter-particle correlations, extracting it provides a clearer picture of short range inter-particle structure.

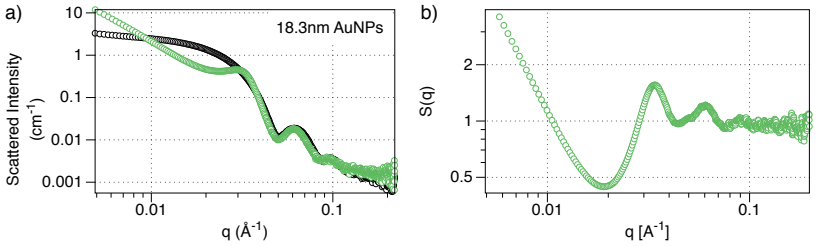


Figure 32: Effect of AuNP assembly on scattering pattern a) Scattering patterns of 18.3nm AuNPs functionalized with JR2EC2-KC2, in dispersed (black) and assembled (green) states. The JR2EC$_2$-KC$_2$ mediated assembly of AuNPs (green) results in a structural peak near 0.03Å^{-1} and a porod region at low q (0.005Å^{-1} to 0.02Å^{-1}). b) By dividing the scattering patterns from assembled AuNPs by that of dispersed AuNPs the structure factor S(q) can be extracted (green).

Quasi-Crystalline approximation

A rough interpretation of the structure factor can be performed by fitting the position and width of the structure factor peak. This provides a crude estimate of structure type and magnitude of order, however as Bragg's law only applies to true crystals, fitting of diffuse peaks must be taken with caution [75]. This is particularly the case with nanoparticle aggregates, as the primary peak is sensitive to volume fraction, shifting to higher q with increasing volume fraction [75]. The peak maxima (q_{peak}) can be approximately related to a scattering distance via Braggs law ($q_{peak} \simeq \frac{2\pi}{d}$), to estimate the centre to centre distance between neighbouring particles. The correlation length ($\xi = \frac{2\pi}{\triangle q}$) is obtained by fitting the full width half maximum ($\triangle q$) of the first structural peak

in S(q) [174][60] and provides an estimate of range of crystalline order within the aggregate [145].

For sufficient order, secondary peaks can become visible in the assembly structure factor (Figure 33b). Calculation of the relative position ratios ($q_0 : q_n$) of the primary (q_0) and secondary peaks (q_n) allow for comparisons with common lattice structures (Table 4) [86][174]. A clearer representation can be achieved by scaling the q axis relative to the primary peak.

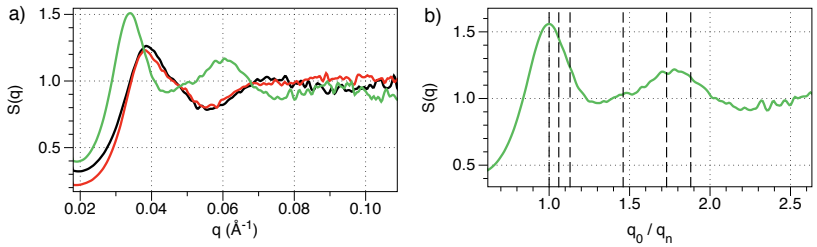


Figure 33: a) Structure factors S(q) of 18.3nm AuNP aggregates, functionalized with citrate (black), BSPP (red) and JR2EC$_2$-KC$_2$ (green). The citrate and BSPP functionalized AuNPs have been aggregated using NaCl, resulting in disordered aggregates. The JR2EC$_2$-KC$_2$ mediated assembly of AuNPs results in a more pronounced S(q) with secondary features visible, indicating a greater presence of order. b) S(q) of 20nm AuNP aggregates functionalized with JR2EC$_2$-KC$_2$ with the q axis scaled relative to the primary peak position. The horizontal dashed lines represent the theoretical positions of HCP peaks.

FCC		BCC		HCP	
Diffraction plane (HKL)	Relative position	Diffraction plane (HKL)	Relative position	Diffraction plane (HKL)	Relative position
(111)	1.00	(110)	1.00	(100)	1.00
(200)	1.15	(200)	1.41	(002)	1.06
(220)	1.63	(211)	1.73	(101)	1.13
(311)	1.91	(220)	2.00	(102)	1.46
(222)	2.00	(310)	2.24	(110)	1.73
(400)	2.31	(222)	2.45	(103)	1.88

Table 4: Relative lattice positions and diffraction planes of lattice peaks for HCP, BCC and FCC lattices [86]

2.5.9 *Structure factor models*

As Bragg's law only applies to true crystals, fitting of diffuse peaks with Braggs law must be taken with caution [75]. The position of the primary peak is known to shift to higher q with increasing volume fraction [75]. This necessitates the use of more complicated models derived from liquid theory for the structure factor. Particles suspended within a liquid are subjected to many body interactions, direct interactions between a pair of particles are represented by the direct correlation function c(r),

whilst interactions through other particles are described by the total correlation function $h(r) = g(r) - 1$ (Figure 34). The relationship between c(r) and h(r) can be described by the Ornstein-Zernike (OZ) integral equation. As the Ornstein-Zernike equation contains two unknowns (c(r) and h(r)), it can only be solved if another 'closure' relation is added. The Percus-Yevick or Mean Spherical Approximation closure relations are commonly used as they allow for a simple analytical solution to the integral equation. The Mean Spherical Approximation is given by

$$\begin{aligned} c(r) &= -\frac{U(r)}{k_B T} \quad \text{for } r > D \\ h(r) &= -1 \quad \text{for } r < D \end{aligned} \tag{2.20}$$

Where D is the diameter of the particle and $\frac{U(r)}{k_B T}$ is the interaction potential. The Mean Spherical Approximation is often used to describe charged systems as coulomb interactions can be included.

The Percus–Yevick (PY) approximation is given by

$$c(r) = g(r)\left[1 - \exp\left(-\frac{U(r)}{k_B T}\right)\right] \tag{2.21}$$

The Percus–Yevick closure has the advantage of generating analytical solutions of the OZ equation for common short ranged inter-particle potentials such as hard sphere and sticky hard sphere. Once c(r) is known, the structure factor S(q) can be calculated using

$S(q) = \frac{1}{1 - N c(q)}$

where c(q) is the Fourier transform of c(r).

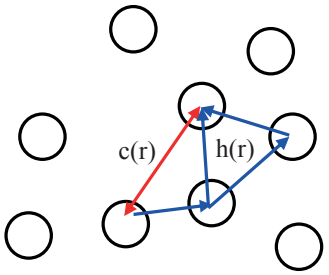


Figure 34: Illustration of direct c(r) (→) and indirect h(r) (→) inter-particle interactions. Redrawn from [77].

Square well potential (SWP)

The interaction between particles is modelled as an attractive square well with and infinite repulsion [121]. The mean spherical approximation (MSA) closure is used for this calculation and is not the most appropriate closure for an attractive inter-particle potential [113][114]. The interaction potential is defined as:

$$\frac{U(r)}{k_B T} = \begin{cases} \infty & r < 2r_{hs} \\ V(r) & 2r_{hs} \leqslant r \leqslant 2r_{hs}\lambda \\ 0 & r > 2r_{hs}\lambda \end{cases} \tag{2.22}$$

Where V(r) is the well depth, r_{hs} is the hard sphere radius and the well width (λ) is defined as multiples of the particle diameter ($2r_{hs}$). Whilst a good fit is observed with experimentally obtained structure factors, the SWP generates unrealistically wide well widths (Figure 35).

Sticky hard sphere (SHS)

The sticky hard sphere model first introduced by Baxter [16], describes the particle interaction U(r) by a square well of infinitesimal width and infinite depth, superimposed on a hard core repulsion [152][194]. The model uses the Percus-Yevick closure relation but generates a more realistic potential then the SWP. The hard core repulsion is established once the distance between particles 'r' becomes less than or equal to twice the hard sphere radius (r_{hs}). The interaction potential $U(r)$ is described by:

$$\frac{U(r)}{k_B T} = \lim_{\Delta \to \infty} \begin{cases} \infty & r < 2r_{hs} \\ \ln\left[12\tau\left(\frac{\triangle}{2r_{hr}+\triangle}\right)\right] & \text{for } 2r_{hs} \leqslant r \leqslant 2r_{hs}+\triangle \\ 0 & r > 2r_{hs}+\triangle \end{cases} \tag{2.23}$$

Where $\triangle$ is the width of the square well potential and τ is the stickiness parameter. The particle stickiness (τ), is a dimensionless quasi--temperature describing the change from hard sphere behaviour (large τ) to sticky sphere behaviour (small τ) [238]. The reciprocal ($\frac{1}{\tau}$) provides an estimate of the adhesive potential between particles. The fitting parameters for the model are particle volume fraction (ϕ), particle stickiness (τ), hard sphere radius (r_{hs}) and perturbation parameter (ε). The perturbation parameter ($\varepsilon = \frac{\triangle}{2r_{hr}+\triangle}$) describes the ratio of well ($\triangle$) width to hard sphere diameter ($2r_{hs}$) and is valid for $0.01<\varepsilon<0.1$. It should be noted however, that the volume fraction (ϕ) and particle stickiness (τ) are not completely independent [162][50][199][38][65], as an increase in attractive potential can be counterbalanced by a decrease in volume fraction [238][194][86]. Additionally ϕ and ε both have a well-known dependence on τ [50], making it difficult to find a unique independent solution for both ϕ and ε.

Structure factors were fitted directly using a least squares fit; whilst the same model code is implemented in both the Irena [90] and NIST SANS macros [114], the fitting process was found to converge more smoothly with the NIST SANS macros. Under the least squares fit a variation of 5% of a parameter easily detectable. For fitting, the NIST model documentation recommends to initially keep (ε) fixed and to allow other parameters to settle toward a fit. Under these conditions τ was found to vary slightly $\tau = 0.1 \pm 0.02$; to simplify the fitting process further, τ was fixed at 0.1 allowing ϕ and r_{hs} to converge to a unique result. Under these circumstances an increase in ϕ describes both a positive change in volume fraction and particle interaction potential. The SHS model provides good fits with experimentally obtained structure factors, whilst generating more realistic well widths than the SWP (Figure 35).

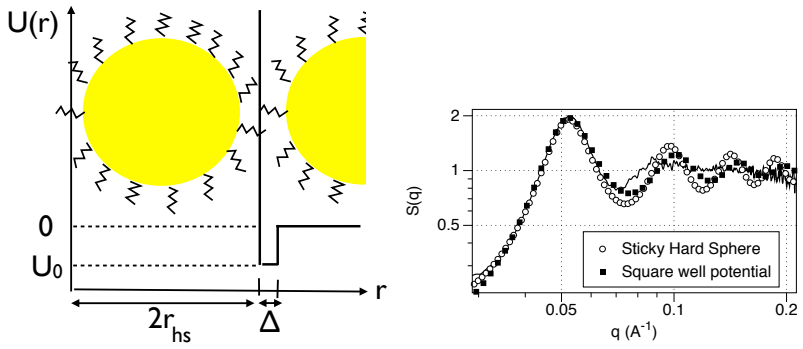


Figure 35: a) Well potential used for Baxters sticky hard sphere model; u_0, $2r_{hs}$ and Δ are the depth of the well, hard sphere diameter and the well width. b) Sticky hard sphere (◯) and Square well potential (■) models applied to the structure factor of 9.4nm AuNPs assembled with the polypeptide JR2EC$_2$-KC$_2$ (Chapter 3). A good fit with experimental data is observed for both models, however the SWP generates unrealistically wide well widths.

3

POLYPEPTIDE FOLDING-MEDIATED NANOPARTICLE ASSEMBLY

3.1 INTRODUCTION

What is it with humans and size anyways? Just because something is very, very small doesn't mean that it can't be important.
- Men in Black (Movie, 1998)

Efficient, sensitive biomolecule detection is an essential component of public healthcare, with early detection critical for the treatment of many diseases. This fundamental need drives the search for new effective high sensitivity biomolecular detection assays. Materials that are chemically and structurally defined at the nanoscale, offer novel electric, optical and chemical properties, making them suitable for applications in biosensing [3][202] therapeutics [159], drug delivery [67] and tissue engineering [216][224][220]. The fabrication of novel nano-structured materials requires a reproducible method for precise control of assembly process and arrangement of the components. An encouraging route for assembly of inorganic nano materials is through the use of biological macromolecules such as polypeptides [203][221][214] and DNA [160][9]. Biological structures typically display unique properties such as multi-functionality, self repair and strong mechanical properties (considering the softness of their component proteins). Their programable inter-molecular interactions and flexibility (both structural and chemical) allow natural biomolecules to assemble into elaborate hierarchical structures [154]. Through careful design, biomolecules can be chosen that change conformation in response to subtle environmental physicochemical changes. This enables the engineering of high sensitivity biosensors that transduce molecular changes into visual signals. For example AuNPs functionalized with DNA have been developed to detect cysteine residues [124], ATP [240], K^+ [241], Hg^{2+} [128][250], oligomeric hairpin DNA sequences [89] and enzymes such as alkaline phosphatase [255]. The rigidity of DNA enables assembly of AuNP into ordered quasi-crystalline structures [180]. As AuNP optical properties are extremely sensitive to inter-particle spacings, precise reproducible control of assembly structure enables the development of nanoparticle assays with robust and reliable optical changes.

The use of designer polypeptides offers an alternate route to DNA for biomolecular mediated assembly of nanomaterials. The characteristics of polypeptides can be customised through management of their amino acid positioning to emulate proteins found in nature or implement

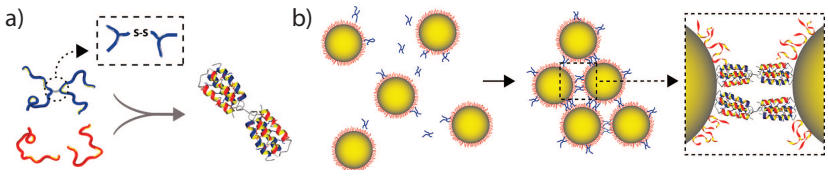


Figure 36: a) Assembly of two disulphide-linked four-helix bundles, through the association of JR2KC$_2$ and two complementary JR2EC polypeptides; b) Introduction of JR2KC$_2$ to AuNPs functionalised with JR2EC induces formation of ordered nanoparticle assemblies through polypeptide bridging. Images reproduced from [6].

novel designer behaviour. Increasing expertise in protein chemistry and synthesis joined with advancements in comprehending the intricate relationship connecting amino acid sequence and 3D protein structure allow for the engineering of novel synthetic polypeptides [3][100][251][80][27][14]. Additional flexibility is introduced from the ability to integrate chemical groups that are not found in nature. The overall charge of polypeptides can be modulated through protonating or de-protonating their constituent residues via control of pH. This enables engineered polypeptides to fold or unfold in response to pH.

Presented here is the characterisation of gold nanoparticles assembled using de novo designed polypeptides developed by D. Aili [7]. The assembly is achieved by the folding-dependent bridging of the AuNPs induced by the heteroassociation of immobilised helix-loop-helix polypeptides and a complementary non-linear polypeptide found in solution. The polypeptides are engineered to complementarily fold into a heterotrimeric complex comprised of two disulphide-linked four-helix bundles [56]. This chapter investigates the correlation between the optical properties of the AuNP assemblies and their in-situ 3D structure, as a function of assembly linker concentration and particle size.

3.2 POLYPEPTIDE MEDIATED ASSEMBLY OF AUNPS

The assembly mediators in this study are two 42 residue synthetic polypeptides, JR2EC and JR2KC, that heterodimerise in solution into four-helix bundles (Figure 36a) [4]. The main driving force behind folding is the formation of a hydrophobic core formed from the hydrophobic faces of the amphiphilic helices. At pH7 JR2EC and JR2KC are negatively (-5) and positively charged (+11), with favourable electrostatic interactions inducing heterodimerisation but preventing the formation of homodimers. Both peptides have a cysteine residue in the loop region (position 22), allowing for the formation of fiber forming units $JR2EC_2$ and $JR2KC_2$ by oxidation into disulphides. When linked, the disulphide mixed monomers $JR2EC_2$ and $JR2KC_2$, are known to form long, thin fibers through a propagation association into four helix bundles (Figure 41) [4].

The cysteine residue, enables the immobilisation of JR2EC onto the surface of gold nanoparticles. The subsequent addition of JR2KC2, induces the spontaneous aggregation of particles through the formation of two disulphide linked four helix bundles, composed of two JR2EC molecules linked by $JR2KC_2$ (Figure 36) [6].

3.2.1 *Materials and methods*

Citrate coated gold colloids (approx 10, 20 and 40 nm in diameter) were purchased from British BioCell international. The polypeptides JR2KC (NAADLKKAIKALKKHLKAKGPCDAAQLKKQLKQAFKAFKRAG), and JR2EC (NAADLEKAIEALEKHLEAKGPCDAAQLEKQLEQAFEAFERAG) were synthesised using standard fluorenylmethoxycarbonyl (Fmoc) chemistry protocols and coupled to gold nanoparticles by Dr Aili, the synthesis protocols are described elsewhere [56]. UV-VIS spectroscopy was performed by Dr Aili using a Perkin Elmer Lambda 25 UV-VIS spectrometer, TEM was performed using a Joel 2010 TEM and the software Image J used to obtain size distributions. SAXS measurements were performed at the Australian synchrotron SAXS/WAXS beamline.

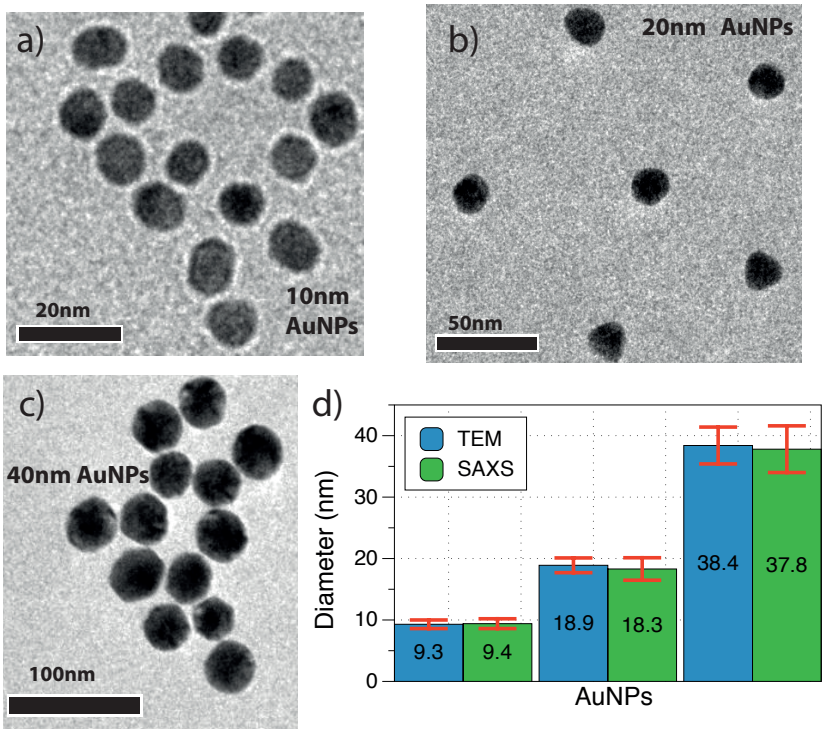


Figure 37: TEM Images of AuNPs with diameters of a) 9.3±0.7nm b)18.9±1nm and 38.4±3nm. c) Comparison of AuNP diameters obtained using TEM and SAXS.

A a low noise Pilatus 1M detector and a beam energy of 10 KeV and were used; with a sample detector (S-D) distance of 3 m used for the 10 and 20 nm Au NPs and a S-D of 7 m for 40 nm Au NPs, providing an accessible q range of 0.0049 to 0.2289 $Å^{-1}$ and 0.0023 to 0.1081 $Å^{-1}$ respectively. Silver behenate was used as a q space calibrant [85]. Liquid samples were measured inside 1.5mm (diameter) quartz capillaries (Figure 22); the fluid was oscillated within the capillary, so as to reduce radiation damage to the sample. Further details of the experimental methods are presented in the experimental methods chapter (Chapter 2).

3.2.2 *Characterisation of particle size and concentration*

Au NPs were characterised using a Joel 2010 TEM and size distributions obtained using ImageJ software [2] (Figure 37). A log-normal particle size was found to fit the particle size distribution and was chosen to describe the particle distribution for both SAXS and TEM measurements. Particle mean sizes and standard deviations of 9.3±0.7nm (n=500), 18.9±1nm (n=500) and 38.4±3nm (n=150) were obtained. SAXS measurements correlated closely with TEM, yielding particle sizes of 9.4±0.8 nm, 18.3±2 nm and 37.8±4 nm (Figures 37b and 38). In order to perform these experiments, the absolute concentration of the polypeptide JR2EC was chosen to remain fixed. To maintain the concentration of JR2EC constant across all experiments, the concentrations of nanoparticles were adjusted to yield a constant surface area per volume of liquid of $0.3 m^2 L^{-1}$, fixing the concentrations of particles at 1.6 nM, 0.4 nM and 0.09 nM, for 9.4nm, 18.3nm and 37.8nm AuNPs

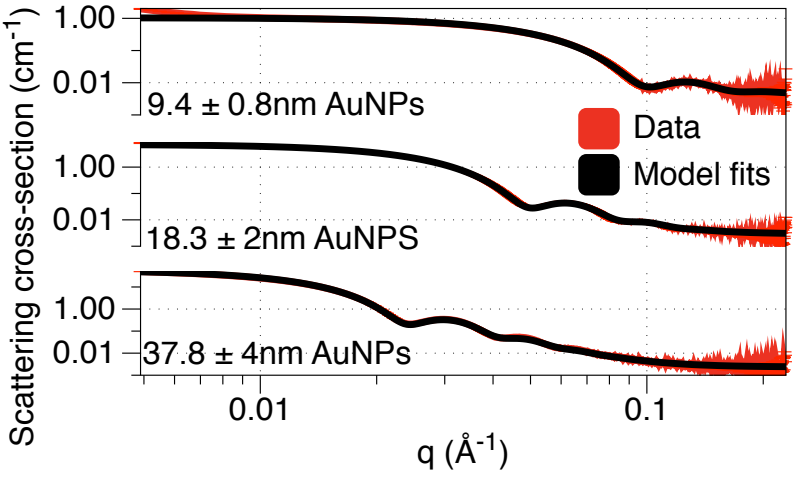


Figure 38: SAXS profiles from AuNPs with diameters of 9.4±0.8 nm, 18.3±2 nm and 37.8±4 nm (—), fitted using a spherical form factor with a lognormal distribution (—).

respectively. The concentrations of AuNPs were determined using UV-VIS spectroscopy and SAXS. The surface coverage of JR2EC on planar gold has been reported to be approximately 60% of a monolayer, with each monomer having an estimated footprint of 2 × 2 nm^2 [6]; hence the concentration of immobilised JR2EC is approximately 70 nM. For AuNPs with diameters of 9.4nm, 18.3nm and 37.8nm this corresponds to approximately 40, 175 and 780 JR2EC polypeptides per AuNP.

3.2.3 *Characterisation of synthetic polypeptides using SAXS*

Characterisation of monomers JR2EC$_2$ and JR2KC$_2$

Stock solutions of 0.5mM JR2EC$_2$ and JR2KC$_2$ polypeptides (0.1 M ammonium bicarbonate buffer, pH8) were characterised using SAXS (Figure 39). The scattered intensities were fitted using Guinier and Porod plots, Kratky plots and pair-distribution functions. Further descriptions of these techniques can be found in the experimental chapter (Chapter 2.5).

GUINIER AND POROD FITS Guinier fits provided radii of gyration (R_g) of 2.04nm and 1.6nm for JR2EC$_2$ and JR2KC$_2$ respectively. Dynamic light scattering measurements reported in literature, estimate the size of the hydrodynamic radius of the polypeptides to be about 3nm at pH7 [4]. The polypeptide JR2EC$_2$ displays logarithmic scattering at high q, which was fitted with a Porod gradient of 2.1; this is characteristic of a branched polymer [52][153]. Whilst both JR2EC$_2$ and JR2KC$_2$ are 42 residues in sequence length, the difference in radius of gyration and introduction of logarithmic scattering (for JR2EC$_2$), indicates that JR2KC$_2$ forms a more compact globular structure in solution, whilst JR2EC$_2$ forms a larger branched structure. This is thought to be as a result of the slightly basic pH of the buffer, reducing the charge on JR2KC$_2$.

KRATKY PLOT Kratky plots ($I(q)q^2$ vs q) are useful for providing an indication of protein folding state [52]. A characteristic peak at low q is

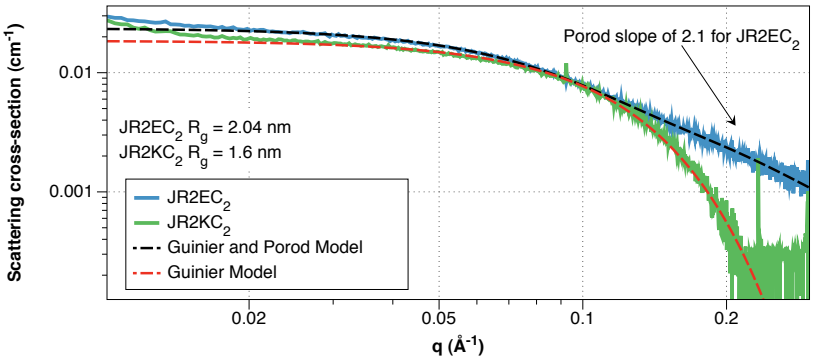


Figure 39: Scattering profiles of 0.5mM JR2EC2 and JR2KC$_2$. Polypeptides are fitted using a Gunier fit, with a Porod model added for JR2EC$_2$.

indicative of folded globular proteins, whilst unfolded proteins display an extended rise in $I(q)q^2$ with q. Flexible multi-domain proteins, demonstrate a combination of these features [153]. The Kratky plots for JR2EC$_2$ and JR2KC$_2$ indicate a compact globular structure for JR2KC$_2$ and a flexible multi-domain character for JR2EC$_2$.

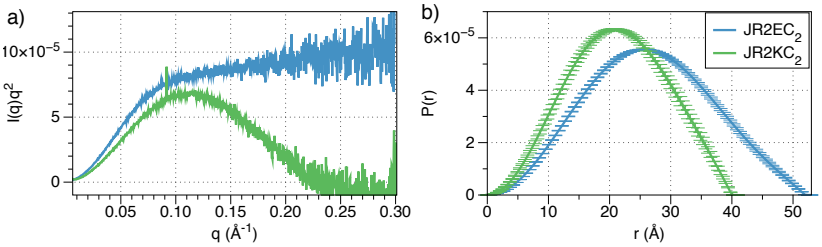


Figure 40: a) Kratky plots and b) Pair distribution of JR2EC$_2$ (blue) and JR2KC$_2$ (green). Under a Kratky plot JR2KC$_2$ displays a characteristic peak, indicating a globular structure, whereas a gradual rise with increasing q indicates a more disordered structure for JR2KC$_2$. Radii of gyration of 2.05nm and 1.6nm are obtained from the Pair distribution function for JREC$_2$ and JRKC$_2$ respectively.

CALCULATION OF PAIR DISTRIBUTION FUNCTION The scattering data from JR2EC$_2$ and JR2KC$_2$ were fitted using a regularisation technique to yield the pair distribution function. This approach calculates the maximum distance of scattering objects within the analyte and the radius of gyration [153][135]. The measured radii of gyration (2.05 and 1.6nm) closely agree with those from Guinier fits (Figure 39), with JRKC$_2$ displaying a more compact structure than JR2EC$_2$. The calculated pair distribution data, can be used to construct low resolution shape models for the proteins, using programs such as GASBOR, DAMMIN and SASHA [74][60][153][52], however this is beyond the scope of this thesis.

POLYPEPTIDE CHARACTERISATION SUMMARY We obtain radii of gyration of 2.04nm and 1.6nm for JR2EC$_2$ and JR2KC$_2$, with evidence suggesting that JR2EC$_2$ displays a globular conformation, whilst JR2KC$_2$ has a more branched structure. The peptide stock solutions were kept in a weakly basic buffer (pH 8), with a high salt concentration (0.1 M) to facilitate their oxidation into fiber-forming units. Under these

conditions, JR2KC$_2$ is less charged due to partial deprotonation of the primary amine groups in the lysine side chains, whilst JR2EC$_2$ becomes more charged at higher pH. These conditions are thought to lead to JR2KC$_2$ adopting the observed globular structure, whilst producing a more branched structure for JR2EC$_2$.

Characterisation of fibers formed from JR2EC$_2$ and JR2KC$_2$

Polypeptides JR2EC$_2$ and JR2KC$_2$ were combined in equal ratios at concentrations of 10μM, 0.1mM and 0.25mM in Hepes buffer and allowed to self-assemble into fibers (Figure 41). Using SAXS, at the lowest concentration of 10μM, it is not possible to differentiate the fiber scattering from background noise, indicating the sensitivity limits of the beam-line. For the 0.1mM and 0.25mM concentrations a unified fit (Guinier and Porod), yields a radius of gyration of Rg=1.9±0.1nm; a porod fit is applied at high q yielding values of 3.2±0.2 and 3.6±0.5 for 0.1μM and 0.25mM respectively. As the total fiber length is longer than the visible length-scale window provided by SAXS, the Guinier fit describes the cross-sectional length of the fiber and the porod region the fiber surface roughness. For a rod like shape, the Guinier cross section $R_c = R_g\sqrt{3/2}$, were Rg is the radius of gyration obtained from a Guinier plot [135]. The radial cross-section of the fiber (R_c) is therefore estimated to be 2.3±0.1nm. Our obtained values lie between the estimated theoretical size of a single four helix bundle (2 by 2.5nm) and TEM measurements (5nm) [4]. It should be noted that TEM imaging requires sample staining, drying and immobilisation onto a carbon support material, which are expected to denature the fiber.

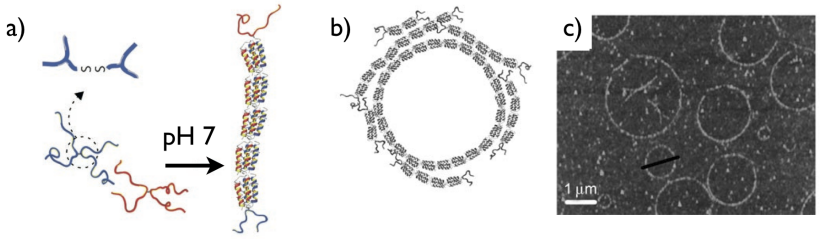


Figure 41: a) Two monomers linked through a disulphide bridge, to form polypeptides JR2EC$_2$ and JR2KC$_2$. When mixed the peptides fold into heteroassociated fibers; b) AFM image of fiber nanorings formed from polypeptide association; c) schematic representation of organisation of polypeptides into rings. Images reprinted from [4]

3.3 OPTICAL CHARACTERISATION

The optical properties of AuNPs place them as a convenient transduction mechanism for biosensor applications, taking advantage of the colourimetric changes upon NP assembly and dissociation. The collective oscillation of surface electrons, known as Localised Surface Plasmon Resonance (LSPR), gives rise to a wide extinction band in the UV-Visible region. The location and extent of this band is greatly influenced by particle size, shape, composition and aggregation. The onset of aggregation introduces a red-shift and broadening of the absorption peak, with the magnitude of the shift depending on the particle size, aggregate density, fractal dimension, and aggregate growth mech-

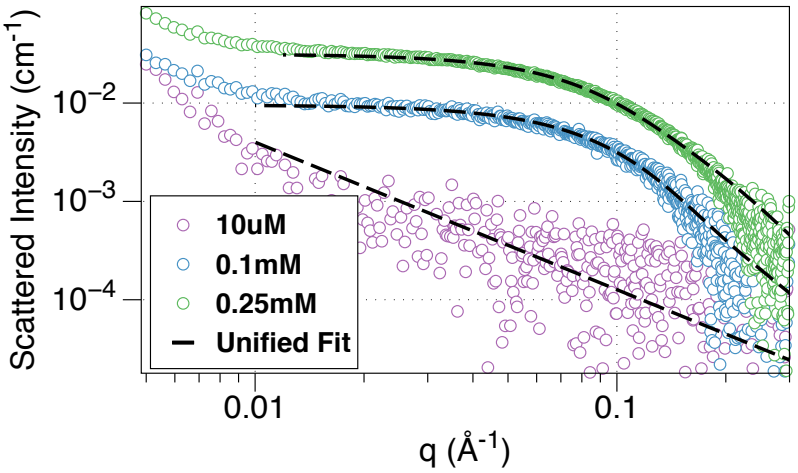


Figure 42: SAXS scattering patterns from fibers formed from JR2EC$_2$ and JR2KC$_2$. At the lowest concentration of 10μM, it is not possible to differentiate the fiber scattering from background noise, indicating the sensitivity limits of the beam-line.

anism [222][179]. The structure of AuNP assemblies is intrinsically linked to the forces and interactions involved in the assembly process; these can be correlated with colloidal growth models such as diffusion-limited cluster-cluster aggregation (DLCA), reaction limited cluster-cluster aggregation (RLCA) and compact clusters (CC) [246][94]. Dispersed JR2EC coated particles (10-40nm), display an absorption maxima between 523-528nm (Figure 43). The introduction of the linker peptide JR2KC$_2$ induces instant aggregation, accompanied by a broadening and red-shift of the LSPR band. The UV-VIS spectra for 10, 20 and 40nm AuNPs before and after the addition of 10μM JR2KC$_2$. The extent of the primary absorption peak shift increases with particle size, shifting approximately 35nm, 50nm and 120nm for 9.4, 18.3 and 37.8nm AuNPs, with the width of the LSPR band also broadening with larger particle size. The change in the peak LSPR position ($\Delta\lambda_{max}$) provides a description of optical change upon aggregation, but does not track changes in peak broadening. The integral ratios of the regions 700 to 550nm and 540 to 490nm, often called the A/D ratio, has been demonstrated as a valuable tool to characterise particle aggregation. A description of this process can be found in the methods section 2.3.3.

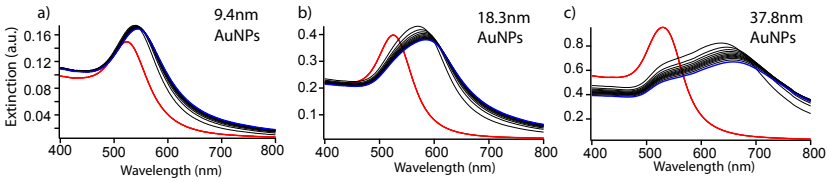


Figure 43: UV-VIS spectrum of JR2EC coated AuNPs with diameters of a) 9.3nm, b) 18.9nm and c) 38.4nm in diameter are shown in red. The spectra upon the addition of 0.1uM JR2KC$_2$ are shown in blue, and were recorded every two minutes for 30min

The change in ΔA/D ratio and $\Delta\lambda_{max}$ over time as a function of JR2KC$_2$ linker concentration and particle size is presented in Figure 44, with the corresponding UV-VIS spectra reproduced in the chapter

appendix 3.7.1. UV-VIS measurements were performed before and immediately after the addition of $JR2KC_2$, with subsequent measurements taken every 2 minutes for a total of 30 minutes. Concentrations of $JR2KC_2$ were chosen to span three orders of magnitude. The magnitude and extent of the red shift, was found to vary as a function of both particle size and peptide linker $JR2KC_2$ concentration.

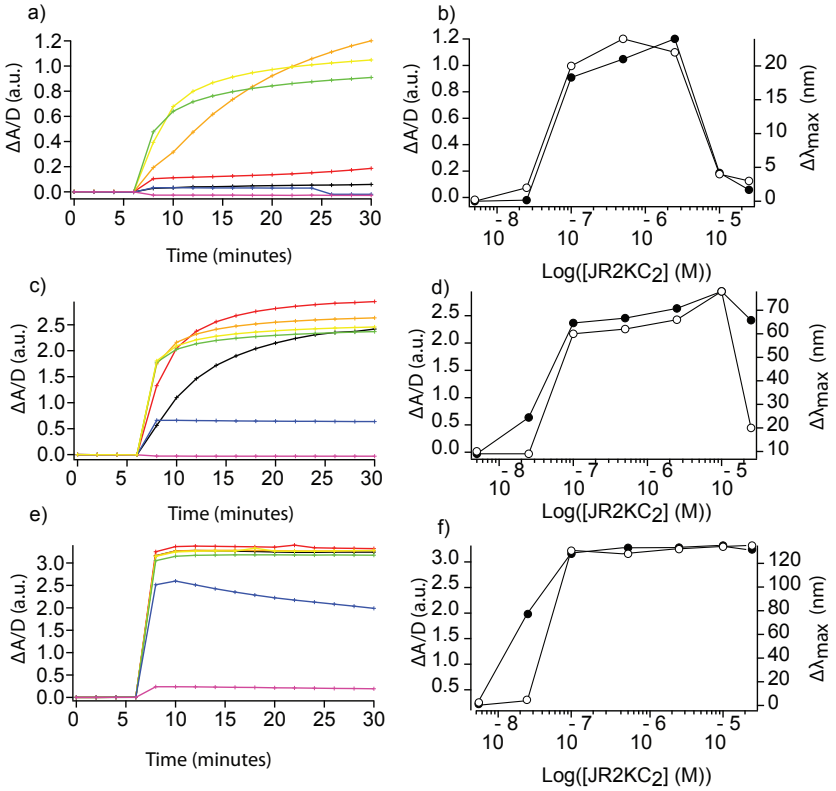


Figure 44: Optical characterisation of $JR2EC_2$ coated AuNPs, upon addition of $JR2KC_2$. Figures (a-c) change in A/D ratio (•) and $\Delta\lambda$max (○) as a function of $JR2KC_2$ concentration; data was obtained 25 minutes after addition of $JR2KC_2$. Figures (e-g) change in ΔA/D over time; $JR2KC_2$ was added after 6 minutes and spectra recorded with 2 minutes interval for 30 minutes. Measurements were performed using AuNPs of 9.4nm (a, b), 18.3nm (c, d) and 37.8nm (e, f) in diameter. The concentration of $JR2KC_2$ was (black) 25 µM, (red) 10 µM, (orange) 2.5 µM, (yellow) 0.5 µM, (green) 0.1 µM, (blue) 25 nM, and (purple) 5 nM.

The 9.4nm AuNPs exhibit little or no spectral shifts for the two lowest (5 and 25nM) and two highest (10 and 25µM) concentrations of $JR2KC_2$, whilst considerable optical shifts were observed for 18.3 and 37.8nm AuNPs for all but the lowest concentrations. The 9.4nm AuNPs aggregate swiftly at 0.1 and 0.5µM $JR2KC_2$, with a slower rate observed at 2.5µM. For 18.3nm AuNPs the reduction in aggregation rate is seen at the two highest $JR2KC_2$ concentrations (10 and 25µM). The slower aggregation rate observed at higher $JR2KC_2$ concentrations and the absence of aggregation for 9.4nm AuNPs at 25µM $JR2KC_2$ is attributed to a combination of the charge reversal of the particles upon polypeptide binding (from slightly negative to positive) and the saturation of binding sites available for polypeptide bridging. At pH7 JR2EC is negatively charged (-5) providing a net negative charge to

AuNPs functionalised with it. The association of positively charged 2x(+11) JR2KC$_2$ with JR2EC functionalised AuNPs results in a decrease of the AuNP charge repulsion promoting assembly formation. At high JR2KC$_2$ concentrations increasing amounts of JR2KC$_2$ provide the AuNP surface with a net positive charge, introducing a repulsive force between particles.

For 9.4nm and 18.3nm AuNPs at 0.1μM & 0.5μM JR2KC$_2$, the optical properties ($\Delta A/D$ ratio and $\Delta\lambda_{max}$) quickly saturate with time, reaching an endpoint. Work carried out by Park et al [179] indicates that the magnitude of plasmon shift is related to total aggregate size. This would suggest that the aggregates quickly grow to an equilibrium size, upon which their size remains constant. This binary behaviour in optical properties, may have potentially useful applications in discrete bioassays.

3.4 SYNCHROTRON CHARACTERISATION

Synchrotron characterisation was performed at the SAXS/WAXS beamline of the Australian Synchrotron, to correlate the optical properties to the structure of AuNP assemblies. The scattered data were integrated to 1D data plots of I(q) vs q, data were corrected for transmission, beam intensity, background scattering, exposure time and normalised to an absolute scale. SAXS data reduction was performed using SAXS15ID in an IDL environment and with modelling and fitting carried out using Irena macros implemented in Igor Pro [90]. More detailed information regarding the data acquisition, reduction and model fitting is provided in the experimental chapter (Chapter 2.5).

SCATTERING FROM AGGREGATES Particle diameters of 9.4±0.8 nm, 18.3±2 nm and 37.8±4 nm were obtained by fitting the scattering from unaggregated particles with a spherical formfactor (Figure 38). The obtained sizes closely agree with complementary TEM measurements 3.2.2. The complete scattering profiles for the JR2EC$_2$ coated AuNPs as a function of JR2KC$_2$ linker concentration are provided in the chapter appendix 3.7.2. To illustrate the effect of aggregation on SAXS patterns, the scattering profile of 18.3 nm AuNPs after 15min of incubation with JR2KC$_2$ ($0 \leqslant [\text{JR2KC}_2] \leqslant 0.1\mu M$) is shown in Figure 45. An increase in aggregate characteristics with increasing linker concentration is observed, agreeing with complementary UV-VIS data. The onset of aggregation introduces logarithmic scattering at low q (Figure 45[i]), the gradient of which is fitted to obtain a measure of aggregate fractal dimension. At intermediate to high q, destructive interference is observed [ii] with a peak at [iii] and small oscillations visible at high q [iv]. By removing the contribution of individual particles from the aggregate scattering, the structure factor S(q) can be calculated. The structure factor has the advantage of being purely determined by inter-particle correlations (Figure 45b). For Figure 45, the Roman numerals describing characteristic regions are kept consistent i.e. regions [ii] to [iv], map directly across a) and b).

SEMI-QUALITATIVE STRUCTURE FACTOR ANALYSIS A coarse interpretation of the structure factor can be performed by fitting the position and width of the structure factor peak. The peak maxima (q_{peak}) can be approximately related to a scattering distance via Braggs law

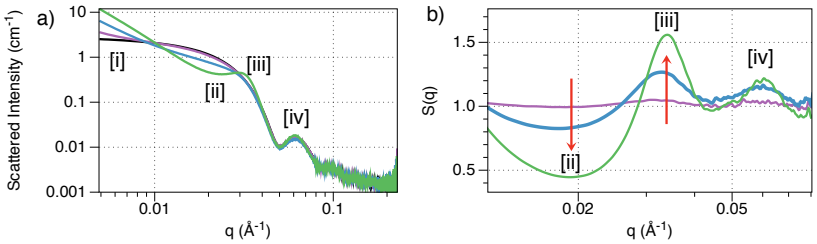


Figure 45: a) Scattered intensity and b) structure factor (S(q)) of 18.3nm nm AuNPs with increasing JR2KC$_2$ concentrations. For consistency the regions [ii] to [iv] in a) are mapped directly onto [ii] to [iv] in b). The arrows in b) indicate the change in S(q) with increasing JR2KC$_2$ concentration. The onset of aggregation gives rise to logarithmic scattering at low q [i], from which a Porod gradient is obtained. From intermediate to high q, a decrease in scattering [ii] is observed as well as a structural peak at [iii] and small shifts at high q [iv]. Changes in regions [ii] to [iv] are more clearly visible in the structure factor; regions [ii] to [iii] were fitted using a sticky hard sphere model and [iii] to [iv] with a para-crystalline approximation. The concentrations of JR2KC$_2$ are 0 nM (black), 5 nM (purple), 25 nM (blue) and 0.1 μM (green).

($q_{peak} \simeq \frac{2\pi}{d}$). The correlation length ($\xi \simeq \frac{2\pi}{\Delta q_{peak}}$) obtained from the full width half maximum (Δq_{peak}) of the primary structure factor peak provides and estimate of crystalline domain size (i.e. range of order within the aggregate). As Bragg's law only applies to true crystals, fitting of diffuse peaks must be taken with caution [75][60]. The primary peak is known to be sensitive to aggregate volume fraction, shifting to higher q with increasing volume fraction [75]. Correlation lengths of approximately $\xi \simeq 50$, 80 and 150nm are observed for particles of diameters 9.4nm, 18.3nm and 37.8nm respectively (Figure 46). These values are similar in magnitude to those reported for DNA coated AuNP aggregates, however larger correlation lengths ($\xi \simeq 500$) have been achieved using thermal cycling [180][174]. Relative to particle size, the correlation lengths indicate the presence of semi-crystalline order across approximately 5 particles for 9.3nm AuNPs ($\xi \simeq 50$nm, **0.1μM** JR2KC$_2$), 4 particles for 18.3nm AuNPs ($\xi \simeq 80$nm, **0.1μM** JR2KC$_2$) and 3.8 particles for 37.8nm AuNPs ($\xi \simeq 150$nm, **25nM** JR2KC$_2$), indicating a relative decrease in assembly order with larger particle size. The AuNP polydispersity increases with size (9.4±0.8 nm, 18.3±2 nm and 37.8±4 nm), however a reduction in Brownian Motion and hence particle mobility is also expected for larger AuNPs. Additionally larger particles posses larger binding regions enabling the cementing of more bridging polypeptides. This effect combined with a reduction in Brownian motion, moderates the extent of dynamic particle rearrangements within the aggregate. Taking into account that for 37.8nm AuNPs, the particle polydispersity (±4nm) is on the order of a bridging polypeptide (~5nm), correlation lengths of $\xi \simeq 150$nm are extraordinary to observe, underlining the inherent ability of biological soft-potentials to tolerate nanoscale imperfections.

Small changes in correlation length are observed upon increasing concentrations of JR2KC$_2$; for 37.8nm AuNPs a sharp increase at 25nM JR2KC$_2$ is observed suggesting a sudden increase in order.

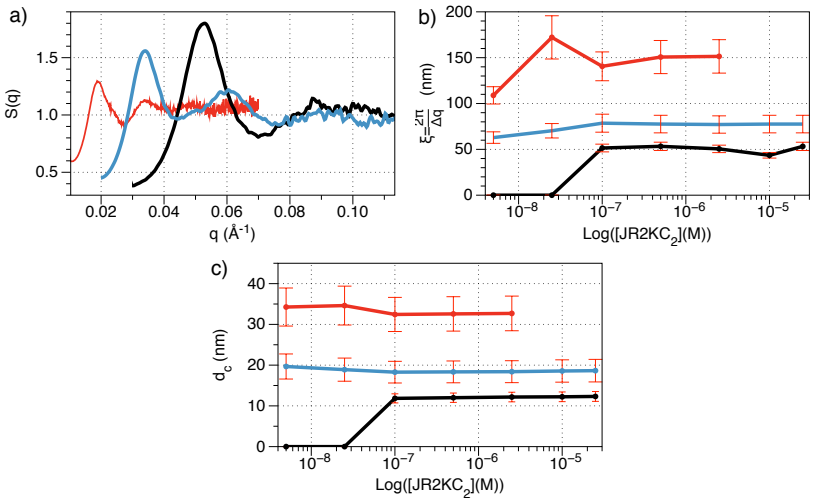


Figure 46: a) Structure factors of JR2EC2 coated AuNPs with 0.1uM JR2EC2. Semi qualitative analysis of the structure factor using b) Braggs law and c) correlation length. Particles of 9.4nm (red), 18.3nm (blue) and 37.8nm (black) in diameter

PARACRYSTALLINE APPROACH The observation of secondary peaks in the assembly structure factor, points to the presence of semi-crystallinity within the assembly. Calculation of the relative position ratios ($q_0 : q_n$) of the the primary (q_0) and secondary peaks (q_n) allow for comparisons with common lattice structures [86][174]. A primary/secondary peak ($q_0 : q_n$) ratio of (1:1.73) indicates the presence of a closed packed structure such as FCC or HCP. These close packed structures are degenerate in energy; any energy difference is expected to be insignificant to non equilibrium effects [149]. The structure factors for 9.4, 18.3 and 37.8nm AuNP assemblies at 0.1µM JR2KC$_2$ are presented in Figure 46a, with other JR2KC$_2$ concentrations presented in the appendix (Figure 58). For easier comparison with expected crystalline peaks, the horizontal axis (q axis) can be scaled relative to the position of the primary S(q) peak (q_0/q_n) (Figure 47).

The (1:1.73) peak ratios are seen for all particle sizes for concentrations of JR2KC$_2$ where aggregation occurs. For 40 nm AuNPs at 25 nM JR2KC$_2$ an additional peak shoulder is visible at (1:1.25) and a minima at (1:1.46) suggesting a possible preference for the FCC lattice over a HCP arrangement.

FRACTAL DIMENSION (POROD FITS) Scattering from nanoparticle aggregates typically display logarithmic scattering scattering ($I(q) \sim q^{-D_f}$) at low q ($q^*R_g >> 1$, where R_g is the radius of gyration) (Figure 45 a)[i]). For values of $1 \leqslant D_f \leqslant 3$, this region provides an estimate of aggregate mass fractal dimension (D_f), describing the scaling in aggregate mass with size ($M \sim R_g^{-D_f}$) (Chapter **??**). Values of $3 \leqslant D_f \leqslant 4$, indicate the presence of surface fractals. The mass distribution of aggregates is intimately linked to their aggregation kinetics. The measured fractal dimension can be compared with colloidal models, such as diffusion limited colloidal aggregation (DLCA) ($D_f \sim 1.8$), reaction limited colloidal aggregation (RLCA) ($D_f \sim 2.1$) and compact clusters ($D_f \sim 3$).

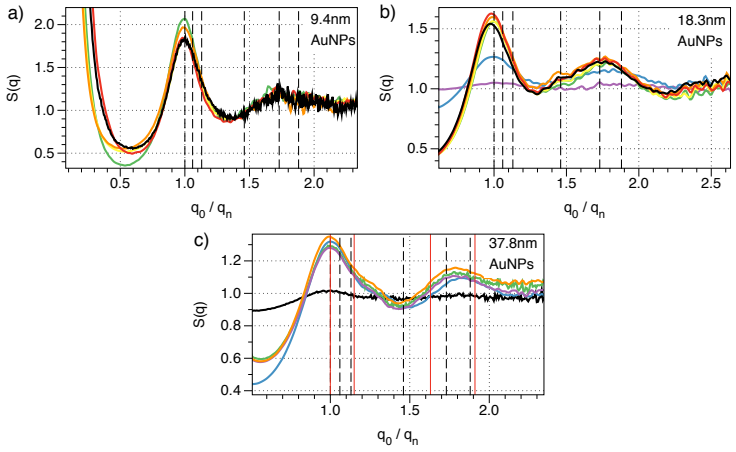


Figure 47: Structure factor of AuNPs, with the q axis scaled to q_0/q_n. The vertical lines indicate the expected positions for HCP (- - -) and FCC (—) structures.

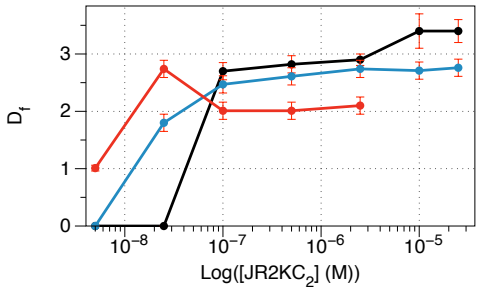


Figure 48: Fractal dimension of AuNPs Particles of 9.4nm (red), 18.3nm (blue) and 37.8nm (black) in diameter

Fractal dimensions (D_f) of 2.8, 2.6 and 2 were observed for 9.4, 18.3 and 37.8nm AuNPs at concentrations of $JR2KC_2$ between 0.1μM and 2.5μM (Figure 48). The fractal dimensions for 9.4 and 18.3nm AuNPs are higher then those predicted by DLCA and RLCA models, approaching values expected for compact clusters ($D_f \sim 3$) [179][180]. The RLCA and DLCA models are derived on the assumptions of particle diffusion and mobility, with particles eventually sticking permanently. Hence higher particle mobility leads to denser aggregates with higher fractal dimensions. The formation of peptide mediated bridging is known to be reversible, allowing AuNP assemblies to dynamically rearrange into denser, energetically favourable structures. The high fractal dimensions observed here, suggest that the particles do not stick permanently and are able to diffuse in dense compact clusters [179]. This has been reported for DNA coated AuNPs [179][174][180]. A sudden increase in fractal dimension for 37.8nm AuNPs occurs at 25nM $JR2KC_2$, indicating a structural rearrangement into a more compact morphology. This behaviour at 25nM $JR2KC_2$ coincides with an increase in particle correlation length ($\xi \simeq 150$nm) and the formation of an additional structure factor shoulder (at $q_0 : q_n = 1{:}1.25$) indicating increased order under this compact morphology.

CHOICE OF STRUCTURE FACTOR MODEL The interpretation of the structure factor requires a suitable model. Two models that are com-

monly used are the Square Well Potential (SWP) and the Sticky Hard Sphere (SHS). The Square Well Potential has the advantage of being simpler but does not fully represent the system physically, whilst the Sticky Hard Sphere offers a more realistic but complicated pair potential. In practice, both the SWP and SHS are able to adequately fit experimental data, as illustrated in Figure 49. The model structure factors over predict the extent of oscillations at high q; the explicit introduction of polydispersity into the structure factor is known to gradually smooth out these oscillations [60]. The SWP generates an unrealistically wide square well width (~1.2 times the particle diameter) necessitating the use of the SHS model for further structure factor modelling.

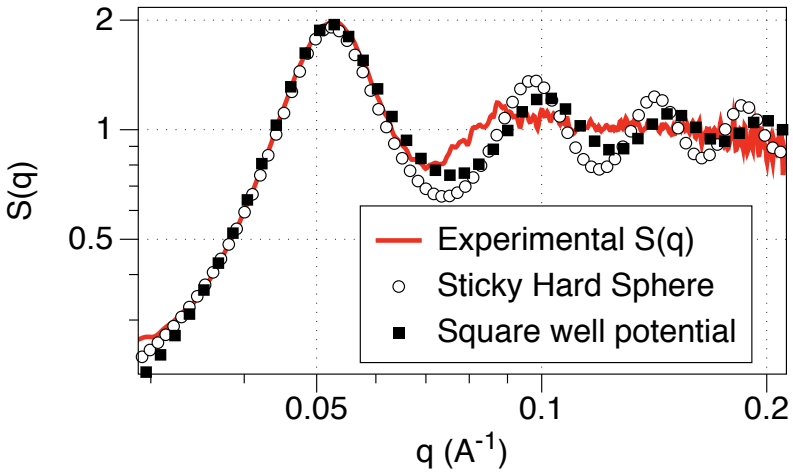


Figure 49: Square Well Potential (■) and Sticky Hard Sphere (○) models applied to structure factor of JR2EC$_2$ coated 9.4nm AuNPs with 0.1μM JR2KC$_2$ (—)

STICKY HARD SPHERE MODEL The structure factor was fitted using the sticky hard sphere model presented by Baxter [16][152]. The model is described by a narrow attractive square well potential, coupled with a short range repulsive potential. The repulsive potential is introduced once adjacent particles approach within a hard sphere radius (r_{hs}), describing the repulsion produced by the overlap of surface peptides. More information regarding the application of the Baxter model is provided in chapter 2.5.9. The model enables the calculation of aggregate volume fraction (ϕ), hard sphere radius (r_{hs}) and particle stickiness (τ). The hard sphere radius (r_{hs}) designates the radial distance from the particle centre to the point where particle repulsion occurs; it is assumed to describe the combined radius of the particle and peptide length. The particle stickiness (τ) is a dimensionless quasi temperature, with the reciprocal ($\frac{1}{\tau}$) proportional to the attractive interaction between particles. An additional complexity is introduced, as ϕ and τ are not completely independent [162][50][199][38][65] as a rise in aggregate volume fraction can be counterbalanced by a decrease in attractive potential [238][194][86]. Unique independent solutions for both ϕ and τ are difficult to obtain [194]. Under free fitting, τ was found to vary only sightly $\tau = 0.1 \pm 0.02$. To simplify the fitting process, τ was fixed to 0.1; ϕ and r_{hs} were fitted providing a unique solution. As τ is fixed,

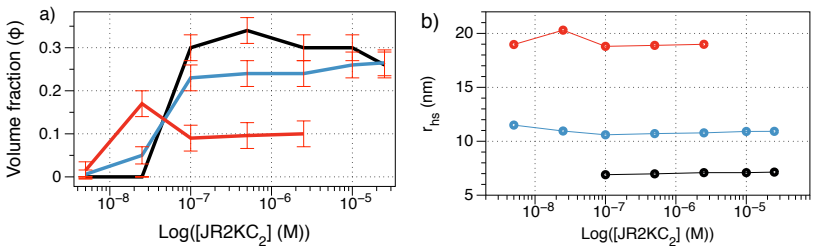


Figure 50: Sticky hard sphere model applied to structure factors of JR2EC modified AuNPs with different concentrations of $JR2KC_2$. a) The volume fraction (ϕ) describes the interaction potential and aggregate density b) The hard sphere radius (r_{hs}) describes the distance at which particle repulsion is introduced due to the overlap between bio-linker molecules. Particles of 9.4nm (red), 18.3nm (blue) and 37.8nm (black) in diameter were used.

a positive increase in volume fraction (ϕ) describes a positive increase in both interaction potential ($\frac{1}{\tau}$) and local AuNP volume fraction.

An estimate of the immobilised polypeptide size can be made by subtracting measured the radius of AuNPs (r_{AuNP}) from the hard sphere radius r_{hs} obtained from the sticky hard sphere model. The hard sphere radius depicts the radial distance from the centre of AuNPs at which particles repel and is assumed in this setting to describe the point at which overlapping proteins repel. For 9.4nm AuNPs, a distance of 4.8±0.4nm is obtained, which closely agrees with sizes measured using SEM (~5nm) [5]. This assumes that there is no preferential orientation of the particles due to AuNP polydispersity. For 18.3nm and 37.8nm AuNPs the polydispersity of particles is on the order of the expected polypeptide size, hindering accurate calculations of separation size using this approach.

3.5 DISCUSSION

Information acquired from both SAXS and UV-VIS was used to correlate the optical response of the particles to changes in assembly structure. More efficient plasmonic coupling between larger particles gives rise to the greater shifts in $\Delta A/D$ ratio and $\Delta\lambda_{max}$ for larger particles [58][93].

CRITICAL $JR2KC_2$ CONCENTRATION FOR AGGREGATION Aggregation is not seen for the lowest two $JR2KC_2$ concentrations (5nM and 25nM) for 9.4nm AuNPs; at 25nM $JR2KC_2$. Light aggregation is visible for 18.3nm AuNPs and extensive aggregation for 37.8nm AuNPs. A clearer understanding about the minimum concentration of $JR2KC_2$ required to induce aggregation can be obtained by estimating the number of $JR2KC_2$ bound to the surface of AuNPs. This was estimated from the dissociation constant of interaction (K_d =0.3μM); at 25nM $JR2KC_2$ approximately 4, 15 and 60 $JR2KC_2$ polypeptides are estimated to be bound to the surface of particles. Hence the absence of aggregation for 9.4nm AuNPs at 25nM $JR2KC_2$ is likely due to the low amount of associated polypeptides.

The 18.3nm AuNPs are just starting to aggregate, with small shifts in both $\Delta A/D$ ratio and $\Delta\lambda_{max}$ a low volume fraction (ϕ) and a low fractal dimension (D_f=1.8±0.2) indicating the presence of loose branched aggregates. Only a few peptides bridges are available, with

particle surface repulsion dominating. The 15 JR2KC$_2$ polypeptides per 18.3nm AuNP represent the minimum required to overcome electrostatic repulsion between particles and induce aggregation. Fractal dimensions of D_f~1.8 are traditionally associated with DLCA aggregates, which display highly branched structures due to high particle sticking probability. For this case, as the bridging polypeptides are able to dissociate, the lower mass fractal dimensions are thought to be related to the electrostatic repulsion between charged particles within the aggregate mediated by the attractive force applied by the bridging peptides.

At 25nM JR2KC$_2$ for 37.8nm AuNPs a sudden increase in volume fraction (ϕ) and fractal dimension (D_f) is observed. This is accompanied by a significant broadening of the LSPR band (Figure 56). The jump in ϕ and D_f indicate the formation of denser aggregates. Closer inspection of the structure factor reveals the introduction of a broad shoulder to the primary S(q) peak and the presence of an additional broad peak at (1:1.25), possibly suggesting a preference of a HCP structure against an FCC. Quasi-forbidden secondary diffraction peaks are known to appear in soft-matter systems, originating from phase boundaries surrounding crystalline islands [62]. Assembly structure is thought to be a mediation between electrostatic repulsion between particles and attraction due to polypeptide bridging. In this case, there are enough peptide bridges to keep the particles assembled, whilst still allowing for particle rearrangements **within** the aggregate to optimise interaction and minimise system energy.

BEHAVIOUR OF AGGREGATES (0.1μM$\leqslant$JR2KC$_2\leqslant$ 2.5μM) Extensive aggregation is seen for all particle sizes at this JR2KC$_2$ concentration range. Overall volume fractions (ϕ) and fractal dimensions (D_f) were observed to decrease with particle size, indicating a decrease in aggregate density with larger particle size. Aggregate correlation lengths ($\xi \simeq \frac{2\pi}{\Delta q_{peak}}$) were overall found to increase with particle size, however taking into account particle size, the range of crystalline order decreases to approximately 5, 4 and 3.8 particles for 9.4, 18.3 and 37.8nm AuNPs. A reduction in Brownian Motion and hence particle mobility combined with wider binding regions for larger particles is thought to moderate the magnitude of dynamic rearrangements, enabling order despite increasing polydispersity for larger particle sizes (9.4±0.8 nm, 18.3±2 nm and 37.8±4 nm).

In this linker concentration range (0.1μM$\leqslant$JR2KC$_2\leqslant$ 2.5μM), 9.4nm AuNPs display a gradual rise in $\Delta A/D$ ratio, $\Delta\lambda_{max}$, volume fraction (ϕ) and fractal dimension (D_f) as a function of linker concentration, whist these remain roughly constant for 18.3 and 37.8nm AuNPs.

37.8nm AuNPs display a lower volume fraction (ϕ), fractal dimension (D_f), when compared to the same particle size at 25mM JR2KC$_2$. Higher JR2KC$_2$ concentrations increase the amount of cooperative peptide bridges, restricting particle rearrangements within the aggregate. This leads to slightly less ordered AuNP aggregates, with a more branched and less dense morphology.

The optical properties ($\Delta A/D$ ratio and $\Delta\lambda_{max}$) quickly saturates with time, reaching a plateau. Work carried out by Park et al [179] indicates that the magnitude of plasmon shift is related to aggregate size. This would suggest that the aggregates quickly grow to an equilibrium size. This binary behaviour in optical properties, is particularly seen for

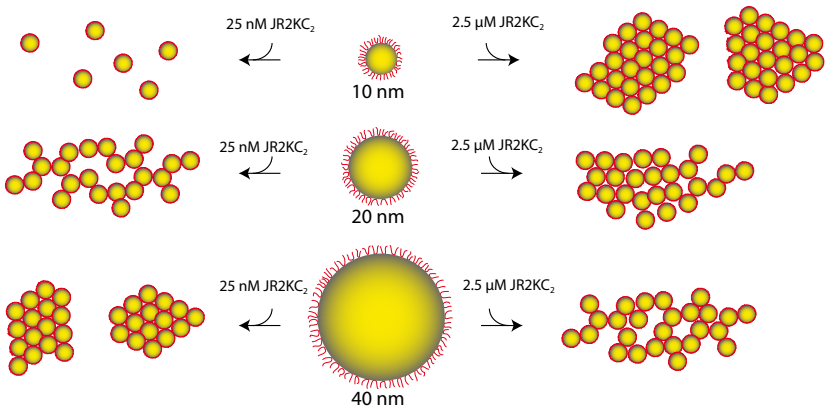


Figure 51: Schematic illustration of proposed assembly structure

9.4nm and 18.3nm AuNPs at 0.1µM & 0.5µM $JR2KC_2$, with potentially useful applications in binary bioassays.

BEHAVIOUR OF AGGREGATES ($10\mu M \leqslant JR2KC_2 \leqslant 25\mu M$) At the two highest $JR2KC_2$ concentration, only small optical shifts are observed ($\Delta A/D$ ratio, $\Delta\lambda_{max}$) for 9.4nm AuNPs and the particle volume fraction (ϕ) decreases. High fractal dimensions of $D_f \sim 3.5$ (indicative of surface fractals) suggest that the aggregate size has shrunk to the point where the aggregate surface is visible under SAXS. Small aggregates of AuNPs (less than 10 AuNPs) have been reported not to display significant optical shifts [106]. The formation of small AuNP clusters at high $JR2KC_2$ concentrations is attributed to a combination of the charge reversal of the particles upon polypeptide binding (from slightly negative to positive) and the saturation of binding sites available for polypeptide bridging. This effect manifests as seen a decrease in aggregation rate for 18.3nm AuNPs at 10µM and 25µM $JR2KC_2$. The proposed structural models for 9.4, 18.3 and 37.8nm AuNPs at 25nM and 2.5µM $JR2KC_2$ are summarised in Figure 51.

3.6 CONCLUSION

Polypeptide mediated assembly of AuNPs is a complex phenomenon arising from a dynamic interplay between particle size, surface charge and polypeptide binding. SAXS and UV-VIS measurements are used to understand these fundamental processes, correlating the optical properties and assembly structure to the kinetics of assembly. The magnitude and extent of aggregation was found to be highly dependent on both particle size and $JR2KC_2$ linker concentration. The presence of order is observed, indicating a close packed structure (FCC/HCP) with a regular inter-particle spacing of 4.8±0.4nm. The polypeptide assembled AuNPs display a higher fractal dimension than commonly seen for aggregated citrate coated AuNPs, indicating the mobility of AuNPs within the aggregate. The reversible nature of polypeptide bridging is likely a key aspect in this intra-aggregate particle mobility. The extent of order is similar to that seen for DNA coated AuNPs, but not as high as for DNA aggregates that have undergone thermal cycling. Larger AuNPs demonstrated lower fractal dimensions (D_f) and aggregate volume fractions (ϕ), indicating a decrease in aggregate density

and increase in branching for larger particle sizes. A combination of decreased particle diffusion with increasing size and wider binding regions enables more cooperative polypeptide binding between particles. This results in a higher sticking probability and lower particle mobility within the aggregate, making structural rearrangements difficult after initial assembly. At high $JR2KC_2$ concentrations, a combination of binding site saturation and particle surface charge reversal, results in the formation of small aggregates (<10 NPs) for 9.4nm AuNPs.

To summarise, when the concentration of linker polypeptides is high enough to induce assembly, but low enough to allow for structural rearrangements, dense aggregates are formed. Smaller particles form denser aggregates due to higher particle mobility and smaller polypeptide binding regions. Particles large enough to accommodate several polypeptides per binding region, display a decrease in aggregate density due to constraints on particle rearrangement after initial assembly. For higher concentrations of $JR2KC_2$, a combination of particle surface charge reversal and binding site saturation, hinders extensive aggregation. These results enable strategies for optimising the structure and the optical characteristics of AuNP assemblies, which are vital for their performance as colourimetric sensors. The work presented here can thus act as a guide in the synthesis of general principles for assembly of NPs by biomolecular mediated bridging, whilst contributing to the fundamental understanding of the assembly process.

3.6.1 *Possible future work*

USE OF LONGER FIBRES Through careful control of $JR2EC_2$ and $JR2KC_2$ concentration, the bridging polypeptide can be formed into a fibre. This could be used to control the spacing between AuNPs in assemblies.

USE OF MORE MONODISPERSE PARTICLES The polydispersity of AuNPs used (9.4±0.8nm, 18.3±2nm and 37.8±4nm) may inhibit the range and extend of order in the aggregates. Several sources offer AuNPs with greater monodispersity for example standard reference AuNPs can be purchased from NIST [23]. Additionally British BioCell International provides "Micro Array AuNPs" with a lower polydispersity. Alternatively, the use of pH control can be used to synthesise AuNPs with a lower polydispersity [108].

NEUTRON SCATTERING (SANS2D) Neutron scattering, combined with deuterium doping could be used to enhance the visibility of the bridging peptide on AuNPs. The ISSIS neutron facility offers a beamline with sufficient capability.

INCORPORATION OF $JR2KC_2$ INTO LIPOSOMES The versatility of the polypeptides JR2EC and JR2KC has enabled their incorporation into a liposome-AuNP based assay for the detection of phospholipase [8]. The assay developed by D. Aili and M. Mager relies on loading liposomes with with $JR2EC_2$, with the complementary JR2EC immobilised on AuNPs. The specific degradation of the liposomes by phospholipase A_2 (PLA_2) releases $JR2KC_2$ enabling folding-dependent nanoparticle assembly, generating a colourimetric response to the enzyme addition (Figure 52).

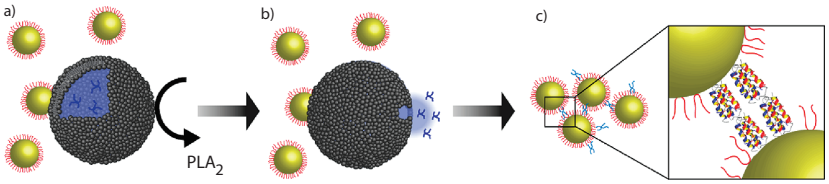


Figure 52: Schematic illustration of hybrid nanoparticle liposome detection of phospholipase assay. a) Liposomes are loaded with JR2EC$_2$ and the complementary JR2EC immobilised on AuNPs. b) Phospholipase A$_2$ (PLA$_2$) hydrolysis of the liposome lipids releases confined JR2KC$_2$. c) The JR2KC$_2$ associated with the JR2EC immobilised on AuNPs leading to nanoparticle assembly. Image reproduced from [8].

Preliminary SAXS measurements of liposomes with and without JR2KC$_2$ were performed at the Australian synchrotron. The SAXS profiles reveal a porod region at low q and two structural peaks at higher q (Figure 53). The structural peak for JR2KC$_2$ loaded liposomes is shifted to higher q compared to the regular liposomes suggesting that the liposomes are smaller upon JR2KC$_2$. The efficiency of JR2KC$_2$ and liposome morphology is likely to affect assay sensitivity and reliability. Further synchrotron studies would allow for further characterisation and optimisation improving the understanding of this system [135].

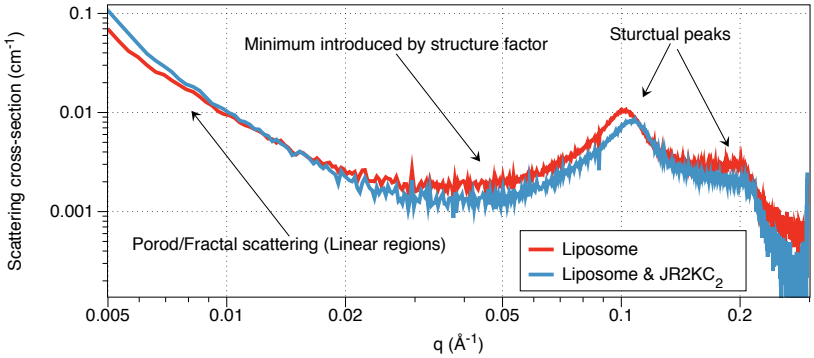


Figure 53: Scattering profiles of liposomes with and without JR2KC$_2$. Structural peaks observed at low q describe the liposome wall thickness, with the shift to higher q, indicating that the incorporation of JR2KC$_2$ results in thinner walls. The Porod region at low q describes the surface roughness of the liposomes, with the steeper gradient for JR2KC$_2$ indicating a smoother surface.

3.7 CHAPTER APPENDIX

Supporting UV-VIS spectra and SAXS data are presented here, for JR2EC$_2$ coated AuNPs, of 9.4±0.8nm, 18.3±2nm and 37.8±4nm in diameter. Concentrations of JR2KC$_2$ are labelled with the colours 5nM (purple), 25nM (blue), 0.1µM (green), 0.5µM (yellow), 2.5µM (orange), 10µM (red) and 25µM (black). These sets of data can also be found in the supplementary information of our published work.

3.7.1 *UV-VIS spectra*

Presented here are the UV-VIS spectra of JR2EC coated AuNPs, before and after the addition of different concentrations of $JR2KC_2$.

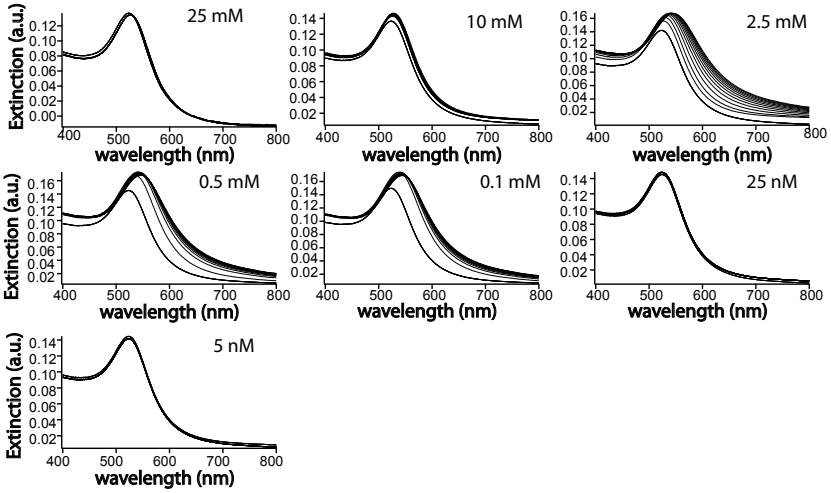


Figure 54: UV-VIS spectra of 9.4nm AuNPs

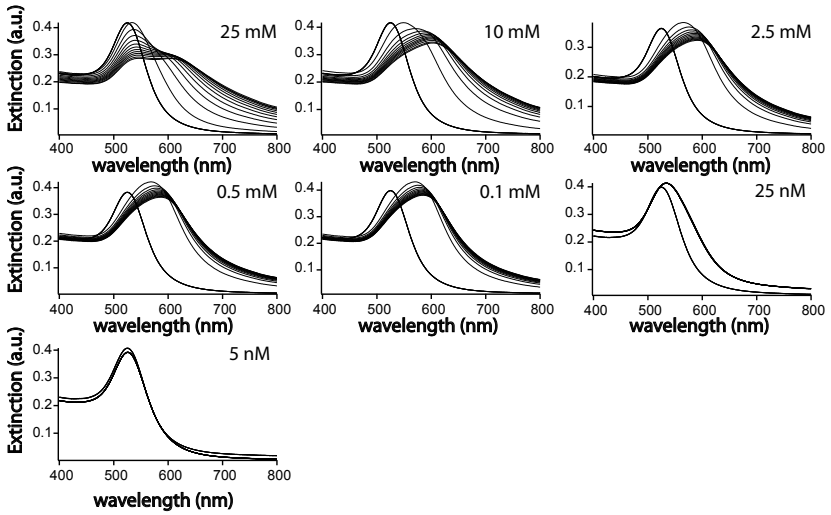


Figure 55: UV-VIS spectra of 18.3nm AuNPs

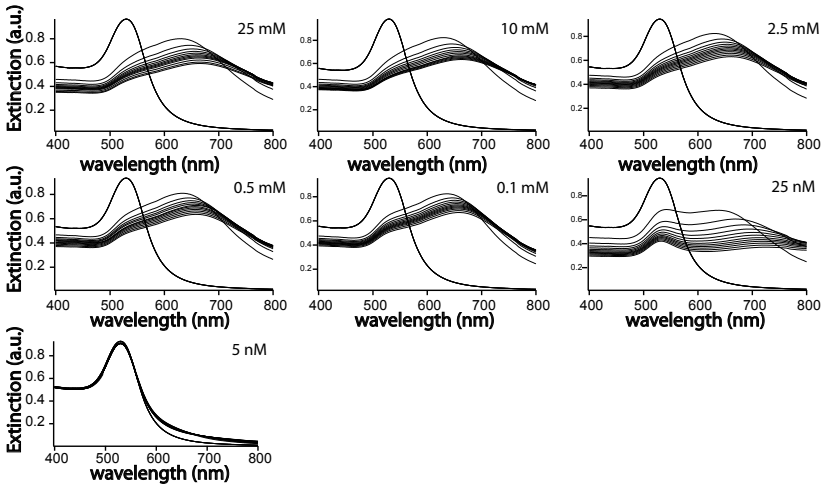


Figure 56: UV-VIS spectra of 37.8nm AuNPs

3.7.2 *SAXS data*

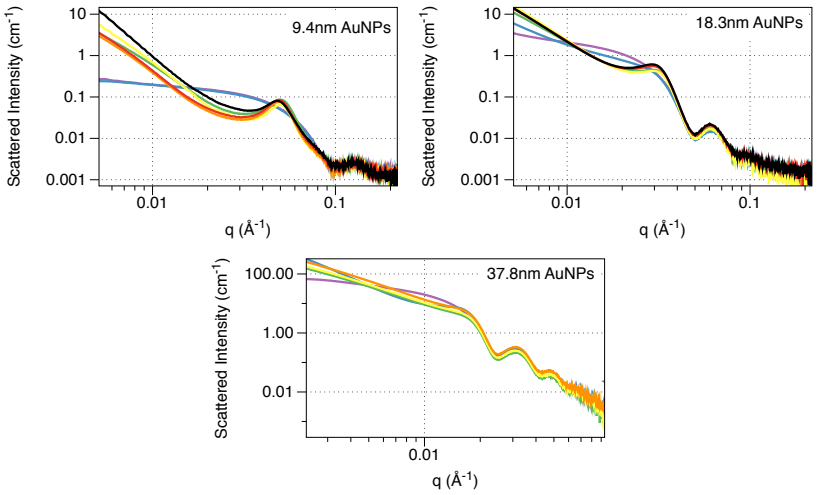


Figure 57: Scattered intensities of $JR2EC_2$ modified Au NPs, 15min after addition of $JR2KC_2$. Particle diameters of 9.4nm, 18.3nm and 37.8 nm were used.

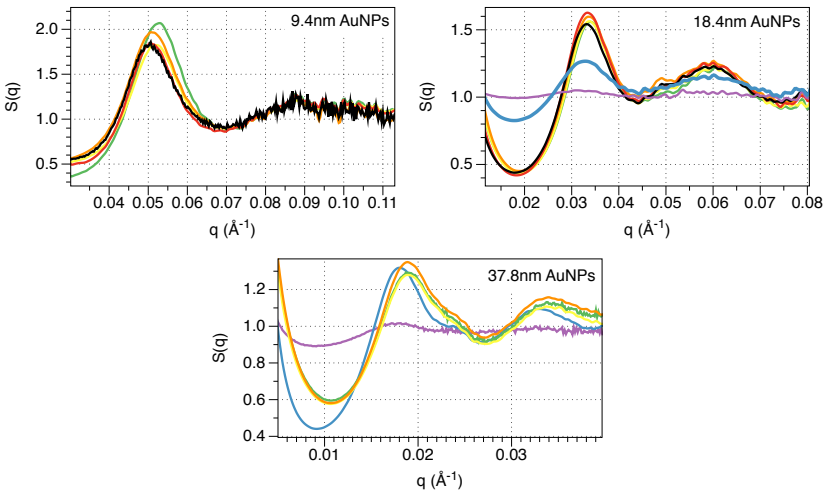


Figure 58: Structure factors of 9.4nm, 18.3nm and 37.8 nm AuNPs.

4

INTERACTION OF GOLD NANOPARTICLE AGGREGATES WITH BSA

4.1 INTRODUCTION

Academic politics are so vicious precisely because the stakes are so small
- Henry Kissinger

Bovine serum albumin (BSA) is a vital component of immunological assays preventing enzyme adhesion and degradation without interfering in immunological interactions [177]. Common assays such as ELISAs (Enzyme-Linked Immunosorbent Assays) use BSA to stabilise enzymes and prevent the adhesion of proteins to the inside of reaction vessels [47][57]. The increasing drive for higher sensitivity has pushed for new biomolecular assays using nano-particle (NP) imaging labels such as gold nanoparticles (AuNPs) and quantum dots (QDs). These particles exploit quantum properties to offer optical scattering cross-sections up to a million times greater than standard chemical fluorophores [12] opening the way for de novo high sensitivity assays. Biomolecular assays are typically complex multi-component systems, relying on enzyme/protein recognition, imaging label, and stabilising factors. A common approach is to adapt current immunoassays by replacing standard imaging labels (e.g. Fluorophores) by NPs.

The colloidal nature of NPs introduces additional complexity in the form of stability control. NPs, due to their high surface energy, are thermodynamically unstable, necessitating the introduction of kinetic stability through surface functionalisation by adsorbed chemical species. BSA is known to bind to the surface of citrate coated AuNPs through a combination of electrostatic attraction and thiol linkage via a surface exposed cysteine group [234]. Due to the complexity of the NP aggregation process and the wide spread use of Serum Albumin in assays, an understanding of the role of BSA on AuNP stability and assembly structure is critical for further assay development.

4.1.1 *Role and structure of BSA*

Serum Albumin is the most abundant protein found in mammalian blood plasma, responsible for regulating the osmotic pressure and pH of blood [34]. Additionally it plays an important role as a transport protein, assisting in the transport of insoluble fatty acids in the circulatory system and demonstrating a particular affinity for many ligands [**?**][171][161][34]. Albumin proteins have been demonstrated as dispersing agents for TiO_2, SiO_2, and Al_2O_3 nanoparticles [24][97][230][218].

Bovine serum albumin is functionally similar to Human serum albumin, displaying similar physiological functions and 76% sequence homology [34]. It is widely available at low cost as a by product of the cattle industry. BSA has a Mw of 66.4 kDa, consisting of 585 residues [248][82]. The secondary structure is a mix of α-helix, β-sheet and random structures [193][186][148].

Thirty four cysteine residues stabilise nine loops through the formation of 17 internal disulphide bonds, thereby supporting the protein tertiary structure [125]. Its small resistance to unfolding leads to its common description as a soft molecule [170], with a propensity to change

conformation upon heating or adsorption [109]. The three principle conformations of BSA are thought to be founded upon these internal disulphide bonds (Figure 59) [125][53]. The normal conformation (N form) of BSA, exhibits a compact globular form with a radius of gyration of 3.4±0.3nm [125] and a slight negative charge [187]. This N form is typically stable at pH's between 4.5 to 8, with the principle stability thought to arise from the internal disulphide bonds. The N form secondary structure is a mix of α-helix (approx 55-65%), β-sheet (21 %) and random structures [193][186][148].

For pH's bellow 4.5, BSA is able to reversibly unfold into a more elongated conformation (F form) with dimensions of approximately 4nm x 12.9nm, with 45% α-helix content [103][192]. This form is known to exhibit greater viscosity and lower solubility. Bellow pH 4, the BSA structure fully extends to an aspect ratio of 1:9 (E form) with 35% α-helix content [26][79][34]. The reduction in α-helix content across these conformations is thought to originate from the unfolding of domains resulting in a loss of intra-domain helicity [34].

Whilst in the N form, only a single cysteine residue is accessible on the surface of BSA, upon transitions to extended conformations (E and F forms) additional residues become accessible for binding to AuNPs [34]. BSA is known to partially unfold between 40 and 50°C, exposing non-polar residues on the surface and facilitating reversible protein-protein interactions [243][43].

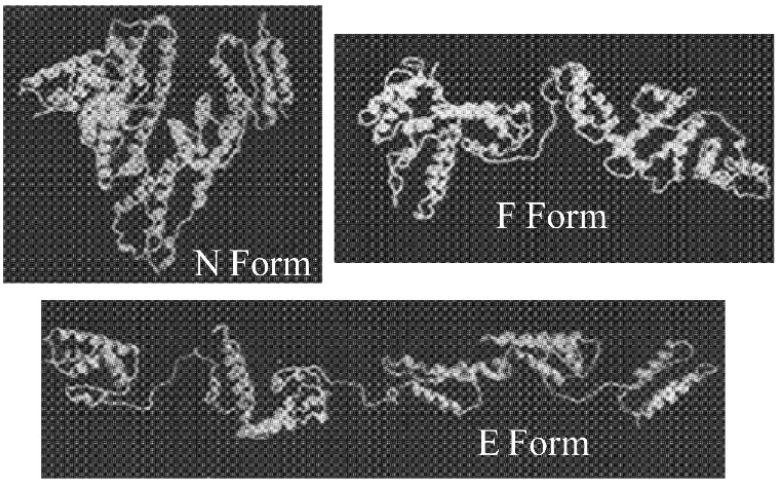


Figure 59: Structures of BSA under: normal conformation (N form, pH 4.5-8), fast conformation (F form, pH 4.5-4), and extended structure (E form, below pH 4). Figures reproduced from [34][234].

4.1.2 *Rationale for work*

The introduction of NPs into physiological fluids results in the formation of a protein corona. This corona alters the physiochemical properties of the NP surface, providing significant impact on the interaction of NPs with their environment (Chapter 1.3.2). Whilst a number of studies have looked at the association of plasma proteins onto the surface of nanoparticles for in-vivo and in-vitro uses [144][24][143][**?**][161][234], there are few studies focusing on serum albumin NP interactions with relevance to NP assembly state and structure. This is particularly critical

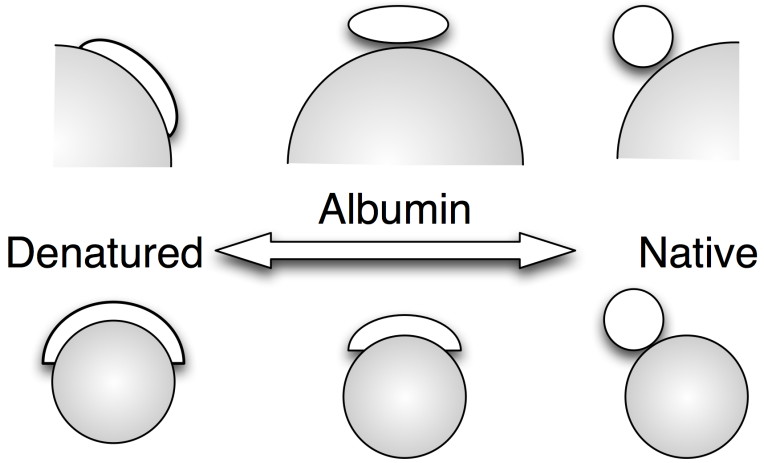


Figure 60: Schematic demonstrating control of biomolecular conformation and orientation by NP surface curvature. Image redrawn from [198].

as BSA and HSA are extensively used in NP bioassays which rely on colourimetric changes transduced through transitions in NP assembly state. Common methods of assembling NPs involve the use of inter-particle cross-linkers (e.g. DNA [257] or polypeptides [7][6][56]) or the destabilisation of particles through the controlled loss of stability (e.g. removal of steric or electrostatic stabilisation [240][241] [128]). The binding of BSA may alter these processes resulting in alterations in NP stability, competitive place exchange with existing NP surface ligands, passivation of exposed NP surface sites, direct interactions with peptide cross-linkers, improvement of NP mobility and absorption of free ligands in solution. These effects may alter the sensitivity of NP bioassays, or provide false results due to unexpected reactions.

NP surface chemistry, physiochemical environment and surface curvature are thought to have major impacts in serum albumin adsorption. Protein structural stability is a balance between electrostatic and hydrophobic interactions counterbalanced by the entropy loss associated with ordering [120]. Interactions with surfaces can shift the interplay between intramolecular forces distorting native protein structures. Possible changes in conformation upon adsorption as a function of NP surface curvature are presented in Figure 60. A study presented by Roach et al demonstrates the structural changes of globular BSA and rod like fibrinogen when adsorbed onto silica NPs (10-90nm diameter) [198]. A reduction in ordered secondary structure is observed in BSA upon adsorption to smaller NPs (between 10-40nm in diameter) with a greater loss in structure for larger NPs (~90nm diameter). Different behaviour is seen for rod shaped fibrinogen which becomes more disordered on smaller particles. The loss of structure in BSA and fibrinogen is seen for both hydrophilic and hydrophobic particle surfaces, but is exacerbated more on the hydrophobic substrates. The adsorption of BSA onto polystyrene nanoparticles has been shown to irreversibly alter the proteins secondary structure through a loss in α-helix content, by Norde et al [172]. Again, this effect is observed to be enhanced for polystyrene NPs with hydrophobic surfaces.

HSA has also been demonstrated to a have an affinity for hydrophobic surfaces by Lindman et al [134]. The adsorption of HSA onto copolymer

particles is observed to be exothermic, with protein binding thought to be entropy driven due to the release of water bound to the surface of NPs [144]. The more hydrophobic particles bind considerably more HSA than the hydrophilic ones, resulting in a higher surface coverage for more hydrophobic particles [144].

The unfolding of BSA on the surface of silica NPs has been shown to have a temperature dependence, with a lower enthalpy change when immobilised [68]. Free BSA in solution is known to undergo reversible conformation changes for temperatures between 42-50°C, with irreversible unfolding of α-helix occurring between 52-60°C [163]. Teichroeb et al investigated the thermally activated denaturing of BSA adsorbed onto AuNPs (5-100nm diameter) for temperatures between 60 and 70°C [232]. They observe an activation barrier for the thermal denaturing of adsorbed BSA with a clear dependency on particle size. The activation barrier increases for smaller particle sizes with that for 5nm AuNPs approximately 25 times larger than that for 100nm AuNPs. Kiss et al demonstrated a gradual increase in adsorption of BSA onto the surface of poly(ethylene oxide) grafted polystyrene NPs as a function of increasing temperature from 25-65°C [109].

This chapter focuses on the role of BSA on AuNP aggregation and assembly structure through the use of salt stability assays, DLS, UV-VIS and SAXS. The effect of temperature, BSA concentration and NP size is investigated for three different AuNP surface chemistries (citrate, BSPP and Fmoc-GFC).

Gold nanoparticles coated in Citrate are common starting materials for AuNP assays. They are widely commercially available and can be easily produced though the citrate reduction of gold chlorate [108][235]. Due to their negative charge, citrate molecules are able to stabilise AuNPs through negative charge repulsion. This electrostatic stabilisation is very sensitive to solvent salt concentration, with the introduction of small quantities of salt ions sufficient to induce aggregation.

Citrate coated AuNPs are often further stabilised using (Bis (p-sulfonatophenyl) phenylphosphine dihydrate dipotassiumsalt) which improves particle stability [211] and is often used as an intermediate, step prior to further functionalisation with ligands such as peptides [190][141][173] or DNA [208][217] [229][142][210][190][239]. BSPP is a water soluble triarylphosphine that is able to form strong coordination complexes with gold nanoparticles due to the presence of a lone pair of electrons on phosphorous [213]. The enhanced electrosteric stability upon functionalisation with BSPP enables repeated cycles of AuNP washing involving NaCl precipitation, solvent removal and re-dispersion [142]. This method of salt washing AuNPs suffers from particle loss and residual aggregation, with washing using centrifugal filters preferable.

Finally the tri-peptide Fmoc-Gly-Phe-Cys-NH_2 was chosen as an AuNP surface ligand. The tri-peptide has been developed for the detection of thermolysin by Laromaine et al [115][122]. The protein includes a sequence designed to be cleaved by the enzyme thermolysin, and hydrophobic Fmoc (Fluorenylmethyloxycarbonyl) groups to promote particle aggregation. Peptides formed from Fmoc groups are known to hydrogelate to form fibres with beta sheet characteristics [39][212].

Three different particle diameters (approximately 10nm, 20nm and 40nm) are chosen to capture a range of surface curvatures. Additionally

as AuNP stability is linked to particle size, a wider particle stability range can be characterised.

4.2 MATERIALS AND METHODS

4.2.1 *Characterisation using TEM, UV-VIS, DLS and SAXS*

SAXS measurements were performed at the Australian Synchrotron with data analysis performed using the Irena macros implemented in Igor Pro. UV-VIS measurements were carried out using a Perkin Elmer Lambda 25 UV-VIS spectrometer and Malvern ZetaSizer nano was used to obtain DLS and Zeta potential measurements. Further details on these techniques are presented in the experimental chapter (Chapter 2). It should be noted that two different AuNP batches are described.

4.2.2 *Sample preparation protocols*

Three different AuNP surface ligands are investigated, citrate, BSPP and Fmoc-GFC, with a diagram representing the functionalisation process presented in Figure 61. Citrate coated AuNPs are obtained from the manufacturer and used as provided; BSPP stabilised particles are prepared by adding BSPP to the citrate coated AuNPs, incubating the samples over night and washing to remove excess BSPP (Figure 61[ii]). The functionalisation with Fmoc-GFC follows the protocol provided by Laromaine et al [122][115], where the tri-peptide Fmoc-GFC is added to AuNPs that have been previously stabilised with BSPP (Figure 61[iii]). The authors work assumes that Fmoc-GFC completely displaces the BSPP previously found on the surface of AuNPs [115]. To test this hypothesis, citrate coated AuNPs were directly functionalised with Fmoc-GFC (Figure 61[iv]). If all the BSPP is displaced from the AuNP surface upon Fmoc-GFC addition, then the properties of Fmoc-GFC functionalised AuNPs should be independent of preparation route, whether prepared from citrate or BSPP coated particles. To distinguish between the two different peptide functionalisation protocols, the peptide functionalised AuNPs are from here on referred to as BSPP Fmoc-GFC or Citrate Fmoc-GFC, reflecting their preparation methods. The first batch of AuNPs have diameters of 9.9±1nm, 20.3±2nm and 42.1±4nm (sizes provided by the manufacturer) were used for DLS and UV-VIS measurements. The second batch of AuNPs have diameters of 8.9±0.9nm and 18.2±2nm were used for SAXS measurements.

Materials

Citrate stabilised AuNPs were purchased from British Biocell International, N,N-Dimethylformamide (DMF) and Bovine serum albumin (BSA) were purchased from Sigma-Aldrich, Bis(p-sulfonatophenyl) phenylphosphinedihydratedipotassiumsalt (BSPP) from Stern and Fmoc-GFC as a powder (purity 99.3%) from Genscript.

Stabilisation with BSPP

Citrate functionalised AuNPs were further stabilised through the addition of 50µM BSPP and left to equilibrate for 24hrs. The particles were washed three times to remove excess BSPP and re-dispersed in

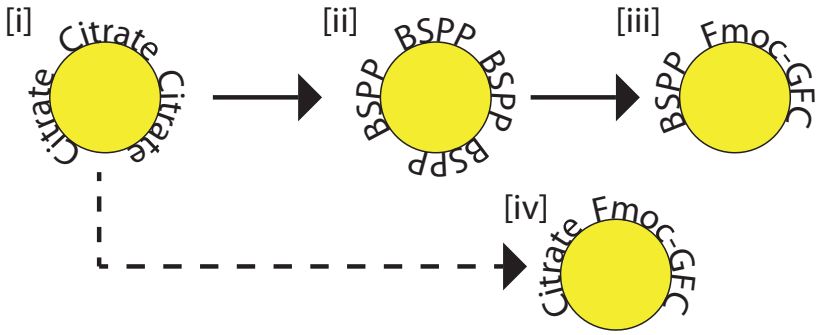


Figure 61: Functionalisation pathways for AuNPs; [i] citrate coated AuNPs are purchased from the manufacturer, [ii] BSPP functionalised particles are prepared from citrate coated AuNPs, [iii] Fmoc-GFC is incorporated onto the surface of BSPP functionalised AuNPs. For [iv] Fmoc-GFC is incorporated onto citrate coated AuNPs, without a prior BSPP stabilisation step.

10mM potassium phosphate solution (pH 8). 10 and 20nm AuNPs were washed using 10,000 MWCO centrifugal filters (Millipore). 40nm AuNPs were found to aggregate under these conditions and so were washed via sedimentation by centrifuging at 1800rcf and removing the top supernatant.

Functionalisation with Fmoc-GFC

A solution of 50μM Fmoc-GFC in DMF was prepared, with 10nm and 20nm AuNPs coupled with 1μM Fmoc-GFC, and 40nm BSPP AuNPs with 0.1μM Fmoc-GFC. After leaving 24hrs to incubate, the particles were washed three times to remove excess Fmoc-GFC. These peptide concentrations were chosen to remain consistent with those used by Laromaine et al [122][115].

4.3 ASSOCIATION OF BSA ONTO AUNP SURFACE

4.3.1 *Characterisation of BSA*

Initial characterisation of bovine serum albumin was performed in the absence of AuNPs using a combination of DLS, SAXS and Zeta potential measurements. Small angle x-ray scattering measurements were performed on solutions of BSA dispersed in Milipure water (Figure 62). The application of a unified fit to a solution of 1mg/ml BSA, yielded a radius of gyration (Rg) of 3.8nm and a porod gradient of 3.2, indicating a rough globular structure (Figure 62a). Bendedouch et al reported a radius of gyration (Rg) of 3.05nm for BSA [22] measured using SANS, whilst other groups have reported measurements of 3nm [92], 3.5nm [176] and 3.15nm [204] using SAXS. The variations in reported values of Rg represent the use of different buffers and pHs for dispersing BSA. The value of Rg reported here is slightly larger then those reported in literature and may be a result of a weak structure factor arising from inter-peptide correlations. For example at a much higher concentration of 20mg/ml BSA, a structure factor peak is clearly visible at q~0.02 $Å^{-1}$ (Figure 62b).

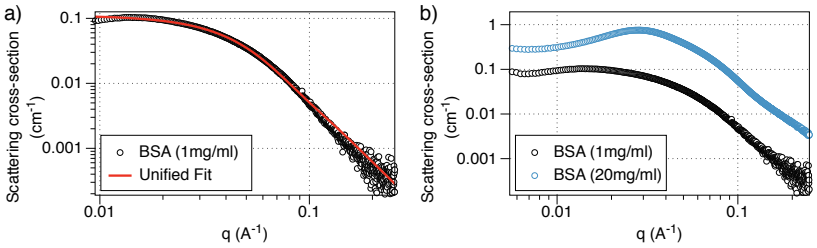


Figure 62: a) SAXS of a solution (1mg/ml) BSA in nanopure water. The pattern is fitted using a unified fit providing a radius of gyration (Rg) of 3.8nm and a Porod gradient of 3.2. b) A comparison of SAXS from BSA at concentrations of 1mg/ml and 20mg/ml. At the higher concentration of 20mg/ml BSA, a structure factor peak is clearly visible at q~0.02 $Å^{-1}$.

Dynamic light scattering (DLS) measurements can also be used to obtain a hydrodynamic radius of gyration for BSA, which describes the combination of the analyte and it's surrounding ion 'corona' [44][25]. Samples of BSA were dispersed in Milipure water, with a range of concentrations from 0.5µg/ml to 2.5mg/ml. The lowest measurable concentration of BSA was at 0.25mg/ml, with an Rg of 5.3±0.5nm obtained at 2.5mg/ml. This radius of gyration represents an intensity weighted mean. When the refractive index of BSA (n=1.445) is used to convert to a volume weighted mean, an Rg of 3.7±0.5nm is obtained, resembling measurements of 3.56nm [35] and 3.4±0.3nm [125] reported in literature. The Malvern ZetaSizer nano used to perform DLS measurements is also able to perform zeta-potential measurements; at a BSA concentration of 2.5mg/ml a zeta potential of -15±3mV was recorded reflecting the proteins slight negative charge [187].

4.3.2 *Dynamic light scattering of BSA adsorption*

The association of BSA onto the surface of citrate functionalised AuNPs was monitored using dynamic light scattering (DLS). This technique infers particle sizes from Brownian motion, providing a hydrodynamic radius, which describes the combination of the particle and it's surrounding protein and ion corona [25][44]. Dynamic light measurements of 9.9±1nm, 20.3±2nm and 42.1±4nm AuNPs were performed with BSA at concentrations of 0 mg/ml, 0.5 µg/ml, 1.25 µ/ml, 2.5 µg/ml, 5 µg/ml, 50 µg/ml, 0.5 mg/ml and 2.5 mg/ml at a temperature of 25°C (Figure 63). These reported hydrodynamic radii are from an intensity weighted mean; a conversion to a volume weighted mean would require knowing the refractive index of the AuNP-BSA conjugate.

Increases in the AuNP-BSA conjugate hydrodynamic radius are observed as a function of BSA concentration for all three AuNP sizes. The increase in radii are approximately 1-5nm for BSA concentrations of 50µg/mL, 4-10nm for 0.5mg/mL BSA and 5-12nm for 2.5mg/ml BSA. The increase in coronal thickness of BSA as a function of BSA concentration has been reported by Tsai et al [234], however free unbound BSA in solution is known to contribute to the measured DLS correlation function, interfering DLS size measurements [234].

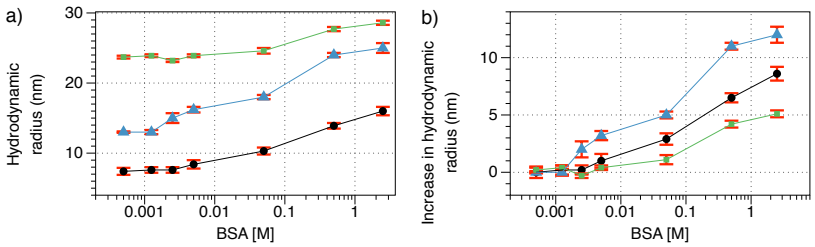


Figure 63: Dynamic light scattering measurements of citrate stabilised AuNPs incubated with BSA. Figure (a) displays the hydrodynamic radius and (b) the increase in hydrodynamic radius. Core AuNP diameters are approximately 9.9±1nm (black), 20.3±2nm (blue) and 42.1±4nm (green).

4.4 STABILITY OF AUNPS TO SALT CONCENTRATION

The stability of colloidal gold nanoparticles is a complex function of NP surface chemistry, solvent composition and particle size. Dispersed gold nanoparticles display a distinct red colour and enhanced extinction band, as a result of Surface Plasmon Resonance (SPR). The aggregation of AuNPs results in a red shift of the absorption spectrum, with the extent of the shift dependent on particle size, aggregate size and aggregate morphology [93] (See chapter 2.3.1). This colourimetric change based on AuNP assembly state is commonly used in nanoparticle biochemical assays to transduce analyte detection into changes visible to the naked eye. The optimisation of AuNP bio-detection systems often involves characterising the salt stability range for each particle size and surface ligand.

Salt stability assays of AuNPs were performed to characterise the stability of AuNPs as a function of surface ligand and particle diameter. AuNPs were incubated with a range of NaCl concentrations for 10 minutes and the UV-VIS absorption spectra recorded using a Safire 2 plate reader. These stability profiles were prepared as a reference for the later characterisation of the effect of BSA on AuNP stability.

As mentioned previously, three different AuNP surface ligands are investigated, citrate, BSPP and Fmoc-GFC. A diagram representing the functionalisation process is presented in Figure 61. Citrate coated AuNPs are obtained from the manufacturer and used as provided; BSPP stabilised particles are prepared by adding BSPP to the citrate coated AuNPs (Figure 61[ii]). Two different approaches are used to functionalise AuNPs with Fmoc-GFC: the first follows the protocol provided by Laromaine et al [122][115] whereby Fmoc-GFC is added to particles previously stabilised with BSPP (Figure 61[iii]) and the second involves direct addition of Fmoc-GFC to citrate coated AuNPs (Figure 61[iv]).

4.4.1 *UV-VIS measurements*

To quantify the aggregation of AuNPs, an integral ratio of the Aggregate region (A) to the Dispersed region (D) of particle UV-VIS absorption was used. The A and D regions represent the primary absorption band of the particles when aggregated and dispersed respectively. The A/D ratio first described by Laromaine et al [122], defines the Dispersed region as 490<D<540 and the Aggregate region as 550<A<700

for 10nm AuNPs. For 20 and 40nm AuNPs the integral regions for the A/D ratio were modified to reflect the absorption band locations. For 20nm AuNPs the Dispersed region was chosen as 500<D<550 and the Aggregate region as 600<A<750. For 40nm AuNPs the Dispersed region was chosen as 500<D<550 and the Aggregate region as 700<A<850. Smoother and sharper transitions upon aggregation are observed when using the A/D ratio, compared to using the absorption at a single wavelength to describe aggregation. A more detailed description of the A/D ratio can be found in the methods section 2.3.3.

Figure 64 displays the salt stability assays of AuNPs as a function of ligand concentration. For 9.9nm AuNPs, the functionalisation with BSPP improves the particle stability over their citrate coating. The further functionalisation with hydrophobic Fmoc-GFC reduces the stability of the 9.9nm AuNPs. For 20.3nm AuNPs, BSPP functionalisation also improves particle stability over a citrate coating. However further functionalisation with Fmoc-GFC does not significantly change AuNP stability.

The regions between aggregation points for the three different capping ligands become smaller for larger particles. For 9.9nm AuNPs, the point at which aggregation starts is fairly distinct for each different capping ligand. The spacing between the points of aggregation for different capping ligands becomes smaller for 20.3nm AuNPs, with those of 42.1nm AuNPs almost overlapping. This decrease in difference between aggregation points suggests that smaller particles may have more flexibility in stability control through choice of surface ligand chemistry. This may be particularly useful for AuNP assays that rely on stability changes for non-crosslinking AuNP assays [257]. It may also be useful for cross-linker systems where precise control of inter-particle forces is necessary to optimise assembly structure [180][6].

The overall stability of AuNPs is observed to decrease with increasing particle size (Figure 64d), which is consistent with standard colloidal DVLO theory which states that attractive forces between the particles increase with increasing particle size [44]. Similar size dependent stability has been reported in literature [175].

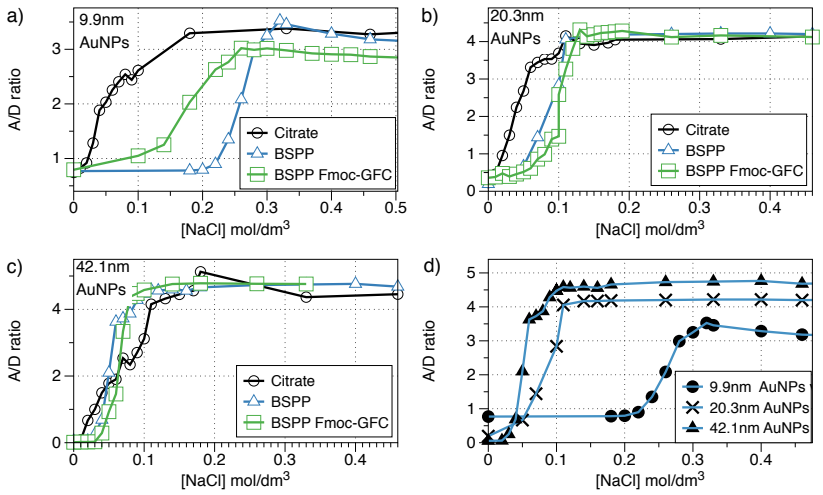


Figure 64: (a-c) Salt stability assay of AuNPs as a function of ligand concentration for particles of diameters a) 9.9nm, b) 20.3nm c) 42.1nm. d) Comparison of the relative salt stability for 10nm, 20nm and 40nm AuNPs functionalised with BSPP.

Figure 65 demonstrates that the stability profile of Citrate Fmoc-GFC is almost identical to Citrate coated AuNPs. This indicates that the peptide Fmoc-GFC is insufficient to stabilise AuNPs by themselves. Hence surface layer of AuNPs prepared using both BSPP and Fmoc-GFC likely have both ligands present, with the improvement in stability is due to BSPP.

Another noticeable effect, is the tolerance of AuNPs stabilised with BSPP to survive repeated cycles of AuNP washing, through NaCl precipitation, solvent removal and re-dispersion in fresh solvent [142]. In other words AuNPs prepared with BSPP or BSPP Fmoc-GFC can be re-dispersed after salt aggregation, through precipitation and replacement of solvent. Citrate and citrate Fmoc-GFC AuNPs aggregate permanently when salt is added and hence cannot be re-dispersed.

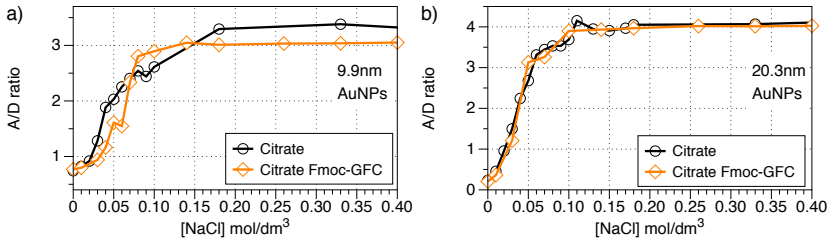


Figure 65: Salt stability assays of citrate coated AuNPs and citrate Fmoc-GFC coated AuNPs for AuNPs with diameters of a) 9.9nm and b) 20.3nm.

4.4.2 *SAXS measurements*

Synchrotron SAXS measurements were performed to characterise the structures formed from AuNP aggregates. Two different sizes of AuNPs were investigated, with particles measured to have diameters of 8.9±0.9nm and 18.2±2nm, where ±0.9nm and ±2nm describe the standard deviations of the particles distributions. These sizes were determined through the fitting of a spherical form factor with a log-normal distribution, to the scattering of unaggregated AuNPs (Figure 66). The precision of the fitted particle mean diameter is estimated to be ±0.2nm and ±0.4nm for particles with diameters of 8.9nm and 18.2nm respectively.

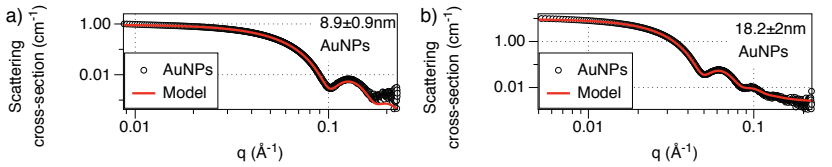


Figure 66: SAXS profiles from AuNPs with diameters of a) 8.9±0.9 nm b) 18.2±2 nm (○), fitted using a spherical form factor with a lognormal distribution (—).

The aggregation of AuNPs was induced through the addition of NaCl. From the previous salt stability assay (Figure 64), salt concentrations were chosen to sufficiently aggregate particles of each size. Salt solution concentrations of 0.35M and 0.15M were used for 8.9nm and 18.2nm AuNPs, functionalised with BSPP or BSPP Fmoc-GFC. For Citrate or Citrate Fmoc-GFC a salt concentration of 0.1M for both particle

sizes; higher salt concentrations induce fast precipitation of AuNPs out of solution, hindering characterisation measurements. SAXS measurements were performed after 15 minutes of salt addition. The scattering from AuNPs as a function of ligand concentration is presented in Figures 67a and 67c. For the 8.9nm AuNPs, the aggregates formed by the citrate coated AuNPs display logarithmic scattering at low q, indicating a fractal structure. A porod gradient of 2.14±0.05 is obtained indicating reaction limited colloidal aggregation (RLCA) (Chapter **??**). The scattering from BSPP and BSPP Fmoc-GFC 8.9nm AuNPs are similar to each other, with a wide non fractal region visible between 0.01<q<0.04 and a short porod gradient of 2.8 between 0.005Å^{-1}<q<0.009Å^{-1}. Non fractal NP structures can be formed when particles are able to dynamically re-arrange within an aggregate into more energetically favourable structures. The porod gradient of 2.8 at low q suggests a dense structure approaching a compact cluster. Porod scattering is only valid when spanned over several orders of q, with insufficient experimentally accessible q to confirm that the porod gradient continues over wider q.

The accessible low q porod region is even smaller for 18.3nm AuNPs, with only a cautious estimate of aggregate porod gradient possible. A porod gradient of 2.8 is obtained for the BSPP and BSPP Fmoc-GFC AuNPs, with a lower gradient of 2.4 for citrate coated AuNPs. This suggests similar behaviour to 8.9nm AuNPs, with BSPP and Fmoc-GFC AuNPs re-arranging into dense clusters, whilst citrate AuNPs stick permanently upon aggregation to form more open branched structures.

By removing the contribution of individual particles from the aggregate scattering, the structure factor S(q) can be calculated (Chapter 2). The structure factor has the advantage of being purely determined by inter-particle correlations [135]. The absence of secondary structural peaks in any of the structure factors indicates the absence of long range order in the aggregates (Figures 67b and 67d). The structure factor peaks for BSPP and BSPP Fmoc-GFC AuNPs are shifted to lower q when compared to citrate AuNPs, suggesting larger centre to centre distances for AuNPs with BSPP coatings. The SAXS profiles and structure factors of citrate and citrate Fmoc-GFC AuNPs are found to overlap (Figure 68) confirming that Fmoc-GFC alone is insufficient to stabilise AuNPs.

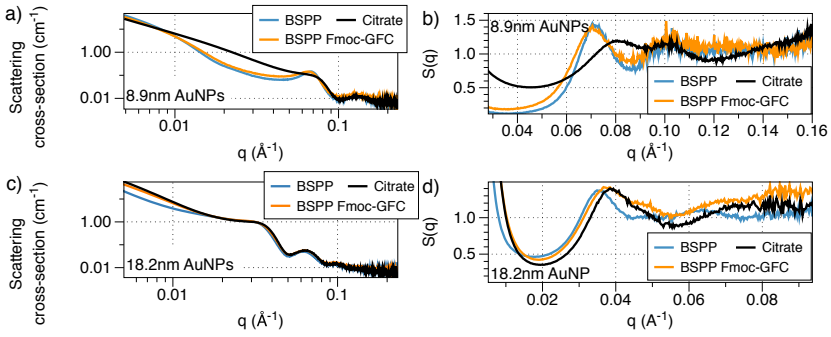


Figure 67: SAXS profiles (a, c) and extracted structure factors (b, d) for AuNP aggregates formed from particles with different capping ligands. AuNPs with diameters of 8.9nm (a, b) and 18.2nm (c, d) are used.

To further interpret the structure factors, a sticky hard sphere model was applied [16][152]. The model describes the interaction between

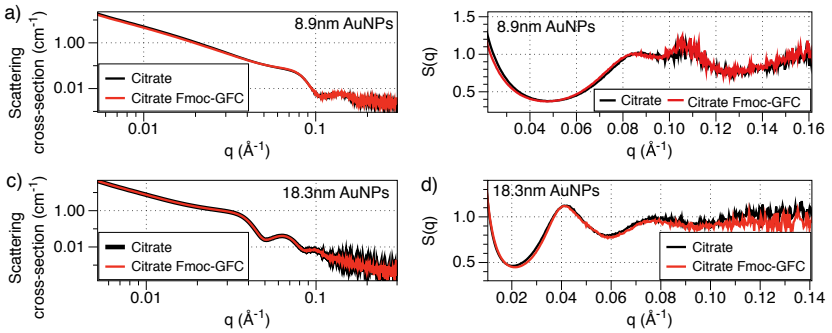


Figure 68: Comparison of SAXS from aggregates formed from citrate and citrate Fmoc-GFC coated AuNPs. a) SAXS from 8.9nm AuNPs and b) 18.3nm AuNPs.

two adjacent particles through the application of a narrow attractive square well potential, coupled with a short range repulsive potential introduced by the overlap of surface ligands. The model enables the calculation of aggregate local volume fraction (ϕ) and hard sphere radius (r_{hs}). The hard sphere radius (r_{hs}) describes the radial distance from the particle centre to the point where particle repulsion occurs; it is assumed to describe the combined radius of the particle and the ligand stabilisation layer. The volume fraction (ϕ) is a function of inter-particle attractive potential and local AuNP density within the aggregate, hence a positive increase in volume fraction (ϕ) describes a positive increase in both these characteristics. The particle stickiness τ was fixed at 0.1 and the perturbation parameter ε at 0.05 as described in previous chapters (Chapters 2.5.9 and 3). More information regarding the application of the sticky hard sphere model is provided in the experimental chapter (Chapter 2.5.9), with the model used to describe the assembly of AuNPs by folding polypeptides in chapter 3.

The results of structure factor fits with the sticky hard sphere model are presented in Table 5. An estimate of the immobilised ligand size can be made by subtracting the measured radius of AuNPs (i.e. r_{AuNP} = 4.5nm or 9.2nm for particles with diameters of 8.9nm and 18.3nm respectively) from the hard sphere radius r_{hs} obtained from the sticky hard sphere model. For citrate coated AuNPs, the hard sphere radius is approximately equal to the AuNP radius, indicating that the surface of AuNPs are touching. For BSPP and BSPP Fmoc-GFC AuNPs similar ligand shell thickness are obtained, in the range of 0.6-0.8nm. The uncertainties on the ligand shell thickness presented in Table 5 are estimated from the precision of r_{AuNP} and r_{hs}.

4.5 EFFECT OF BSA ON AUNP STABILITY

4.5.1 *UV-VIS measurements*

Gold nanoparticles of 9.9nm and 20.3nm in diameter were incubated with a solution concentration of 0.05mg/ml BSA for 10 minutes. Salt stability assays were then performed on the AuNP BSA mixtures at 25°C with the results presented in Figure 69. A large increase in stability is seen for both particle sizes. Exceptional stability is seen for AuNPs stabilised with BSPP Fmoc-GFC, which were stable in salt concentration upto 2 M.

AuNP Aggregate	r_{hs} (nm)	ϕ	Shell Thickness (nm)
10nm AuNP Citrate	4.5±0.1	0.22±0.02	0±0.2
10nm AuNP BSPP	5.1±0.1	0.45±0.02	0.6±0.2
10nm AuNP BSPP Fmoc-GFC	5.1±0.1	0.39±0.02	0.6±0.2
20nm AuNP Citrate	9.5±0.2	0.15±0.02	0.3±0.4
20nm AuNP BSPP	10.2±0.2	0.17±0.02	1±0.4
20nm AuNP BSPP Fmoc-GFC	10±0.2	0.18±0.02	0.8±0.4

Table 5: Results of sticky hard sphere model fitted to structure factors of 10nm and 20nm AuNP aggregates. Particles with core radii of 4.5nm and 9.2nm (i.e. diameters of 8.9nm and 18.3nm) are functionalized with a range of capping ligands and aggregated using NaCl. By subtracting the difference between the hard sphere radius (r_{hs}) and the AuNP core radius an estimate of ligand layer thickness can be obtained.

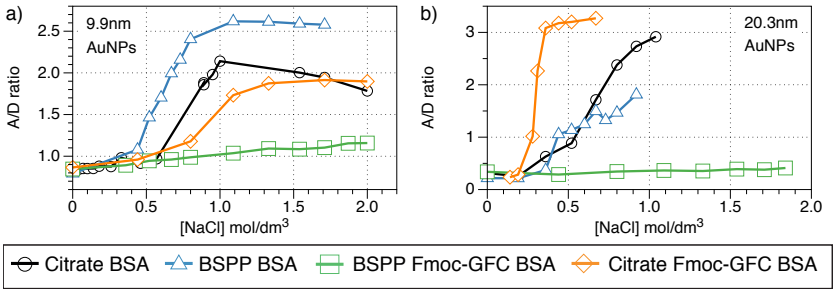


Figure 69: Salt stability assay performed on AuNP BSA conjugates, for AuNPs with diameters of 9.9nm and 20.3nm.

Figure 70 displays the effect of BSA on the assembly state of 9.9nm AuNP aggregates as a function of BSA concentration. The AuNPs were aggregated with 0.35M NaCl and allowed to assemble for 5 minutes. They were then incubated with BSA for 15 minutes and the UV-VIS extinction measured. The experiments were performed at two different temperatures 25°C and 37°C to explore temperature dependencies. The AuNP aggregates are observed to start to disperse at BSA concentrations of 0.5mg/ml, with greater dispersion visible for elevated temperatures. Aggregates formed from Citrate coated AuNPs are found not to disperse in the presence of BSA. Preliminary measurements with 18.2nm AuNPs, show that a lower concentration of BSA (0.05mg/ml) is sufficient to disperse the AuNP aggregates formed from BSPP and BSPP Fmoc-GFC surface ligands, with greater dispersion visible at 37°C compared to 25°C.

4.5.2 *SAXS measurements*

Figure 71 displays the SAXS scattering of 8.9nm AuNP aggregates formed from particles with (a) BSPP and (b) BSPP Fmoc-GFC coatings. The aggregates are then either incubated with or without 0.05mg/ml BSA at 25°C. Despite the concentration of BSA being too low to induce a change in A/D ratio (Figure 70), a decrease in the aggregate structure factor is visible for aggregates incubated with BSA.

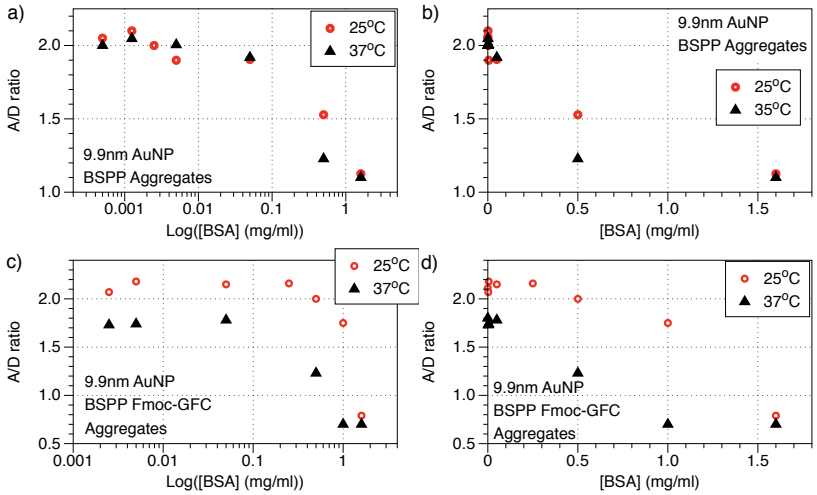


Figure 70: Effect of BSA concentration on aggregates formed from 9.9nm AuNPs. AuNPs are functionalised with two different capping ligands with BSPP (a, b) and BSPP Fmoc-GFC (c, d). The BSA concentration is presented on either a logarithmic scale (a, c) or linear scale (b,c). The assay was performed at two different temperatures of 25°C and 37°C.

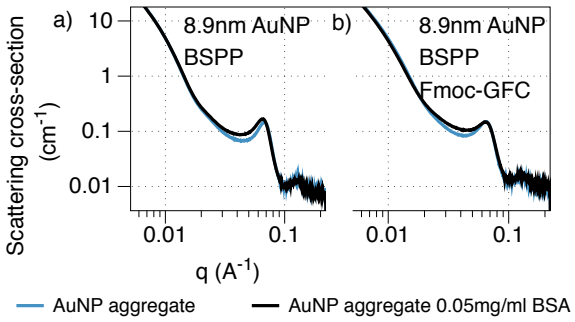


Figure 71: SAXS measurements of 8.9nm AuNP aggregates. The particles are incubated with and without 0.05mg/ml BSA

Figure 72 displays the SAXS scattering and calculated structure factors from 18.3nm AuNPs functionalised with BSPP Fmoc-GFC; the AuNPs are aggregated and incubated with 0.05mg/ml BSA at either 25°C or 37°C. The incubation with 0.05mg/ml BSA at 25°C results in a reduction of the aggregate structure factor, indicating a decrease in aggregate density. At 37°C the structure factor almost completely disappears indicating that the AuNP aggregate disperses.

4.6 CONCLUSION

This chapter investigates the effect of BSA on AuNP aggregates through the use of stability assays, DLS, UV-VIS and SAXS. This work demonstrates that far from being an inert component, the introduction of BSA directly alters the structure, stability and interaction of AuNPs and their aggregates. We find that temperature is a factor in these interactions and a specific affinity for hydrophobic systems. The role of BSA in NP

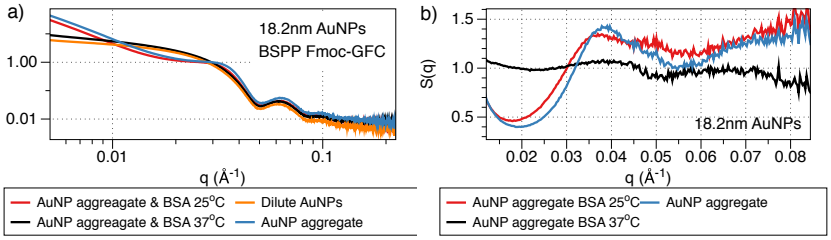


Figure 72: a) SAXS scattering from 18.3nm AuNPs functionalised with BSPP Fmoc-GFC. Profiles are visible for dilute AuNPs (orange), aggregated AuNPs (blue), aggregated AuNPs with 0.05mg/ml BSA at 25°C (red) and aggregated AuNPs with 0.05mg/ml BSA at 37°C (black). b) The extracted structure factors from the aggregates.

systems is not negligible and may play a beneficial role in biosensors based on AuNP aggregates.

For example Aili and Manger et al demonstrated the use of HSA to optimise the sensitivity of a hybrid Liposome-AuNP system designed to detect phospholipase activity [8]. The liposomes are filled with a designer linker polypeptide that induces folding-dependent AuNP aggregation upon release. The controlled addition of HSA removes fatty acids from the membrane specifically decreasing the stability of the membranes and increasing the sensitivity of the system. The AuNP plasmon peak shift is also enhanced in the presence of HSA, suggesting that HSA removes excess fatty acids that may interfere with polypeptide linker folding.

5

PEPTIDE MEDIATED ASSEMBLY AND ENZYME TRIGGERED DISPERSION OF A COMPOSITE QUANTUM DOT GOLD NANOPARTICLE SYSTEM

5.1 INTRODUCTION

Cancer is the second largest cause of death in the western world, after heart disease, accounting for 1.7 million deaths in Europe in 2004 [61]. Cancer metastasis and propagation requires cancer cells to penetrate and infiltrate local healthy tissue, crossing tissue boundaries to form a new tumour site. During this process, natural tissue barriers have to be degraded for malignant cell propagation. The disintegration of these barriers is performed by proteolytic enzymes produced by the propagating tumour [11]. Urokinase plasminogen activator (uPA) is a key enzyme in this process and is hence both a biomarker and drug target for cancer treatment [54].

Common protease assays rely on fluorescence resonance energy transfer between two adjacent fluorophores, one acting as an energy donor, the other as a receptor. Fluorophore assays however are susceptible to photochemical bleaching and exhibit a broad emission spectra. As a result assays based on Quantum dot (QD) fluorescence are an area of active research. Quantum dots are effective energy donors exhibiting a broad absorption spectrum, tuneable narrow emission spectrum and a resistance to photo-bleaching [196]. The tuneable emission wavelength of QDs can be used for concurrent excitation of a mixture of different-sized QDs, enabling multiplex detection systems [37].

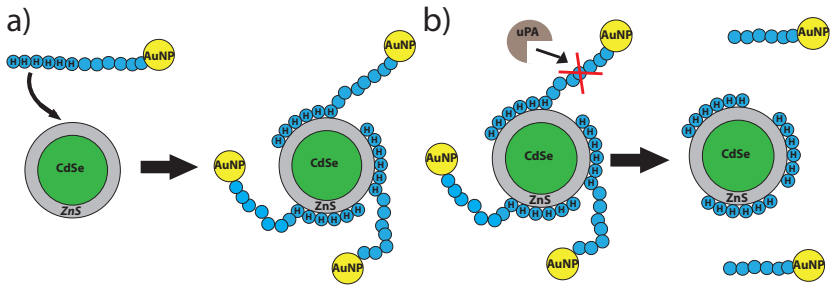


Figure 73: Schematic illustration of a) Peptide mediated surface assembly of Pep-Au onto QDs surface. The peptide anchors the 1.3nm AuNP to QDs via a hexahistadine sequence $(H)_6$ bound through a metal co-ordination bond to the Zn^{2+}. The AuNP quenches the luminesce of the QDs. b) Conjugate disassembly upon addition of uPA. uPA specifically cleaves the substrate peptide, ensuring conjugate dispersion and luminescence recovery

Through the association of electronic structures such as fluorophores or gold particles the luminescence of QDs can be suppressed via a non radiative pathway [196][189][259]. The extent of quenching is dictated by the electron density of the electronic structure, the extent of surface coverage and distance from the QDs surface [196]. The recent development of novel acceptors has focused on the use of metal nanoparticles. For example AuNPs display high quenching efficiencies of up to 99%,

with potential applications as highly sensitive activatable probes. The fluorescence quenching by small AuNPs has a power of 4 distance dependence, providing a greater quenching range compared to fluorophores which obey a 6th power distance dependence [227]. Hence QD - AuNP assemblies are a viable route for highly sensitive bio-molecular detection. For example Pons et al have demonstrated the luminescence quenching of CdSe/ZnS QDs by AuNP acceptors assembled on the QD surface [189].

In this chapter the reversible peptide mediated assembly of Mono peptide functionalized gold nanoparticles (Pep-Au) (1.3 nm diameter) onto the surface of CdSe/ZnS quantum dots (6.3 nm diameter) is discussed (Figure 73). The system consists of monomaleimide functionalised gold nanoparticles (1.3nm diameter), conjugated to a substrate peptide with a uPA specific cleavage sequence (H_2N-H_6GGGSGR↓SANAIC-$CONH_2$) via a C terminal cysteine group, (where ↓ is the cleavage site) [101].

The hexahistidine sequence found on the protein N-terminal, is designed to associate onto the QDs surface, via a metal co-ordination between the Zn^{2+} on the QDs and the histidine residues. The association of the gold particles onto the surface of QDs, results in a quenching of the QDs photoluminescence. QDs have a CdSe core and ZnS shell and a peak eminence at 565nm.

The conjugate is engineered for the detection of the protease urokinase plasminogen activator (uPA), due to its role as an enzymatic biomarker for breast cancer [54]. The addition of uPA results in the hydrolysation and cleavage of the substrate peptide, leading to the conjugate dissociation and a 40-60% recovery of the original luminescence.

This work is a result of a collaboration between this author and Mr John Dick (Imperial College London), who designed and provided the conjugate assay for study. The QDs fluorescence prevents conjugate size measurements from techniques such as DLS. Standard spectroscopy techniques such as UV-VIS absorption and fluorescence spectroscopy are unable to provide structural information whilst electron microscopy techniques require sample drying. These restrictions in standard colloidal characterisation techniques necessitate the use of synchrotron radiation to characterise in-situ assembly.

5.1.1 *Optical properties of quantum dots*

Direct gap semiconductor materials can absorb a photon, promoting a valence electron into the conduction band, generating an electron-hole pair (Figure 74b) [110]. When the dimensions of the semiconductor material approaches the nano-scale, the carriers are confined and the bands become energetically quantised [112]. The photoexcited carriers exist in a 3D potential well, within a quantised ladder of energy levels (Figure 74a). This restricts the transitions between energy levels and therefore the optical transitions that are allowed. As the electron-hole pair are sensitive to the degree of confinement, the optical spectra of QDs are tightly depended on crystal size.

Cadmium Selenide (CdSe) quantum dots are one of the first high quality QDs to be synthesised chemically [164]. Particles can be chemically synthesised with diameters from 0.8nm to 6nm in mean radius, providing control of their emission spectra. Through the coating of QDs in a higher band gap semiconductor such as ZnS, the quantum yield of

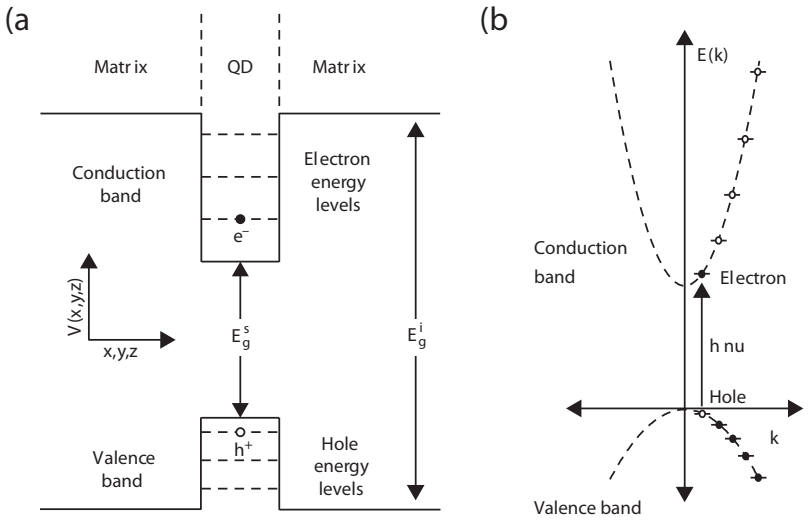


Figure 74: a) Potential well formed in quantum dot in the conduction and valence bands. The carrier (electron and hole) energy levels become quantised due to the finite size of the nanocrystal b) Band diagram describing optical transitions in semiconductor quantum dot. The optical transitions are discrete as a result of quantization of the bands. Diagrams reproduced from [112].

CdSe QDs can be further improved. This core-shell morphology more tightly localises (confines the wave-functions) of the carriers (electrons and holes) in the QDs core and reduced carrier interaction with surface trap sites [182]. Additionally the ZnS shell provides protection to the core from oxidation and improves stability in aqueous solvents.

5.1.2 *Quenching of quantum dots by proximal AuNPs*

When clusters of QDs are formed, optically active ions or metal NPs are brought into close proximity to QDs, an additional pathway for the de-excitation of QDs in introduced [10][42][112][130]. Non radiative energy transfer has been demonstrated from QDs to molecules and metal NPs, and is typically mediated by electrostatic coupling. The initially excited species (in this case the QD) is referred to as the donor, with the energy transferred to a nearby acceptor.

QDs and AuNPs are known to behave as excellent donor-acceptor pairs [189][130]. Small AuNPs (3nm< diameter) exhibit only negligible surface plasmon resonance and hence interact with QDs through nano metal surface transfer (NEST) with a characteristic $\frac{1}{R^4}$ distance dependence on quenching efficiency [116][96]. Larger AuNPs exhibit strong SPR absorption bands which overlap with the emission band of QDs. This energy transfer is dominated through dipole-dipole interaction known as Forster resonance energy transfer (FRET), with an energy transfer efficiency of $\frac{1}{R^6}$ distance dependence [130][200].

NEST describes the behaviour of a dipole emitter where the acceptor metal does not exhibit an SPR band [185]. NEST does not depend on resonant interactions between electrons (as in FRET) but on inter band electronic transitions. The theory considers the formation and interaction of dipole induced electron hole pairs in the thin layer of semi infinite metal hemisphere surface. As a result for the dipole

approximation a $\frac{1}{d}$ coupling instead of the standard $\frac{1}{d^3}$ coupling is used, providing a longer quenching range [130]. The small nanoparticles (diameter 1,3nm) described in this chapter are expected to interact with QDs through nano metal surface transfer (NEST).

5.2 MATERIALS AND SYNTHESIS

All nanoparticle preparation, fluorescence measurements, conjugation chemistry and peptide synthesis were performed by Mr John Dick (Imperial College London); the synthesis preparation methods are included here for completeness.

5.2.1 *Peptide synthesis*

Standard solid-phase Fmoc chemistry was used to prepare the substrate peptides amide-HHHHHHGGGSGRSANAIC-$CONH_2$ and amide-HHHHHHGGGVPLSLTMGGC-CONH2 using an Aapptec ACT Apex 396 Peptide Synthesizer. The peptide amide-HHHHHHGGGSGRSANAIC-$CONH_2$ is designed to be cleaved by uPA [101], whereas amide-HHHHHH-GGGVPLSLTMGGC-$CONH_2$ is designed to be specific for Matrix Metalloproteinase 7 (MMP7) and was used here as a control [249]. The peptides were incubated for 3 hrs with a mixture of 95:2.5:2.5 trifluoroacetic acid (TFA), H_2O, triisopropylsaline to cleave and deprotect the peptides. Cold diethyl ether was used to precipitate and washout the crude peptides. Liquid chromatography was used to purify the peptides to >98% using a Merck Chromolith analytical HPLC column and a water/acertonitrile mobile phase with 0.1% TFA (v/v).

Name	Sequence
Peptide 1	H_2N-$(H)_6$-G-G-G-S-G-R↓S-A-N-A-I-C-$CONH_2$
Peptide 2 (Control)	H_2N-$(H)_6$-G-G-G-V-P-L-S-L-T-M-G-G-C-$CONH_2$

Table 6: Substrate peptide sequences, $(His)_6$ hexa-histidine - residues for QDs surface attachment, spacer residues, enzyme recognition/cleavage sequence, control sequence, cystine residue - AuNP attachment site via thiol. Peptide 1 has a uPA specific sequence [101], with cleavage occurring between the Arginine and Serine residues (R↓S). Peptide 2 has a specific sequence for Matrix Metalloproteinase 7 (MMP7) and is used here as a control [249].

5.2.2 *Quantum dot phase transfer from organic to aqueous solvent*

Quantum dots are hydrophobic by nature and are typically synthesised in an organic solvent. They are then phase exchanged into an aqueous solvent for use in biological environments. CdSe/ZnS Quantum dots with a peak emission at 565nm were purchased from Invitrogen. Peng's method [183] was used to transfer the QDs from decane to HEPES buffer. A mixture of 0.5mL chloroform, 0.5mL 3-mercaptopropionic acid (MPA) (Sigma) and 1g tetrmethylammonium hydroxide pentahydrate (TMAH) (Sigma) was left for one hour, after which the aqueous layer was decanted. 100µL of QDs in decane was precipitated using 800µL of 3:1 MeOH:iPOH solution. The solution was centrifuged at 5000rcf

for 5min, the supernatant removed and the QDs were re-dispersed in chloroform (1mL).

The $CHCl_3$/TMAH/MPA mixture was added to the QDs (in chloroform) and the resultant solution left to settle for two days. The QDs were made soluble through the addition of 10mL of 10mM pH 9.6 borate buffer; the mixture is gently shaken and the organic layer removed. To remove organic contaminants, chloroform was added, the mixture shaken and the organic layer removed; this washing process was repeated twice.

The aqueous solution was then washed using centrifugal filters with a 10 KDa cut-off limit (Milipore) for 12min at 3000rcf. The particles were re-suspended in 10mM borate buffer (pH 9.6), 0.01% wt. BSA and the washing process was repeated two more times to remove contaminants. Finally the QDs were transferred to 10mM HEPES buffer with 0.01% wt. BSA and washed using centrifugal filters twice. QDs concentration was estimated using the molar extinction coefficient ($3 \times 10^6 M^{-1} cm^{-1}$) at the excitation peak (565nm).

5.2.3 *Gold nanoparticle peptide conjugation*

Monomaleimide functionalized AuNPs (NANOGOLD® Invitrogen), with a manufacture provided diameter of approximately 1.4nm ±10% were conjugated to the substrate peptide. Maleimides react with thiol groups to produce stable thioether-coupled products; by this route the monomaleimide group enables the attachment of the AuNPs to most proteins with an accessible sulfhydryl group (R-SH).

The Monomaleimide functionalized AuNPs were dissolved in a mixture of 20μL iPOH and 180μL H_2O. 60μL of 1mM substrate peptide (either amide-HHHHHHGGGSGRSANAIC-$CONH_2$ or the control amide-HHHHHHGGGVPLSLTMGGC-$CONH_2$) in H_2O was mixed with 60μL 0.01M tris(2-carboxyethyl)phosphine (TCEP) and 660uL 10mM HEPES buffer for 18 hours under refrigeration. The solution was washed using 10 kDa centrifugal filters (Milipore) and the solvent replaced with 10mM pH 7.5 HEPES to remove unconjuagted peptide and AuNPs. The concentration of the resultant conjugated AuNPs (Pep-Au) was determined using the molar extinction coefficient ($1.1 \times 10^5 M^{-1} cm^{-1}$) from the UV-VIS absorbance at 420nm.

5.2.4 *Quantum dot conjugation with Pep-Au*

The concentrations of stock QDs and Pep-Au solutions were obtained from their molar extinction coefficients as described previously. The stock solutions were then mixed in Pep-Au:QD molar ratios of 100, 75, 50, 40, 30, 25, 15, 10, 5, 3, 1, 0.5 and 0. This was performed under either constant QDs concentration (starting QDs concentration 8.7nM) or constant Pep-Au concentration (starting Pep-Au concentration 0.53μM). The mixtures were allowed to equilibrate for 20min prior to analysis (SAXS, UV-VIS, Fluorescence).

5.2.5 *Enzymatic dispersion of conjugates*

Native uPA from human urine was purchased from CalBiochem. A solution of 1mg/ml uPA in H_2O was prepared and stored at -20°C. For

dispersion, 5µL of 1mg/ml uPA were added to 37µL of QDs-Pep-Au conjugate for 2.5 hrs at 38°C.

5.2.6 *Inhibitor control*

An enzymatic inhibitor solution of 4-((5-Oxo-2-phenyl-4(5H)-oxazolylidene)-methyl)benzenecarboximidamide trifluoroacetate in DMSO was prepared. This was diluted in H_2O to concentrations of 100µM, 10µM and 1µM for inhibitor control experiments.

5.2.7 *Imidazole induced conjugate dispersion*

Imidazole is commonly used to prevent binding of His-taged proteins during purification [206][226][259] and is applied here as a non-enzymatic control for dispersing the QDs-Pep-Au conjugates. Mixtures of 200mM and 20mM Imidazole were added to QDs-Pep-Au conjugates and left to equilibrate for four hours prior to analysis.

5.2.8 *High Resolution TEM*

A TEM TITAN 80/300 microscope was used to obtained high resolution TEM images of QDs-Pep-Au conjugates. The system provides improved stability in lenses and electronics providing close to atomic resolution TEM and nano-analytical spectroscopy. Samples were dried on Teflon coated copper grids and measurements performed by Mr John Dick and Dr Mahmoud Ardakani.

5.2.9 *SAXS at the Australian Synchrotron*

The small size of analyte particles (Pep-Au ~ 1.4nm diameter, QDs ~ 6nm diameter), expected polydispersity in conjugate morphology and low analyte concentrations necessitated the use of the high performance SAXS/WAXS beamline provided by the Australian Synchrotron. The beamline offers a low noise, high flux, fast detection setup essential for collecting these data. A short camera length (~2m) was used to obtain a low enough q range. SAXS data reduction was performed using SAXS15ID in an IDL environment and with modelling and fitting carried out using the APS Irena macros implemented in Igor Pro [90]. Further information on the beamline and model fitting is provided in the experimental section 2.5.2.

5.3 CHARACTERISATION OF STOCK MATERIALS

For accurate analysis of conjugate experiments, the sizes and concentrations of stock solutions of QDs and Pep-Au need to be obtained. Particle sizes and concentrations are calculated using SAXS; the concentrations are compared to those obtained using UV-VIS spectroscopy. TEM was used to obtain an estimate of QDs diameter, however the Pep-Au was observed to be too small for acquisition of an accurate size distribution via TEM (Figure 79).

5.3.1 *Quantum dots*

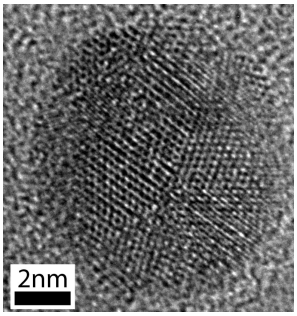


Figure 75: Typical HR TEM image of a CdSe/ZnS QD acquired using a Titan 80/300 TEM. Image provided by Mr John Dick and Dr Mahmoud Ardakani

Stock solutions of QDs dispersed in Hepes/BSA, were characterised using SAXS (Figure 76a). The QDs are known to be spherical and consist of a CdSe core and ZnS shell. For fitting a spherical form factor a size distribution must be assumed to describe the particles polydispersity. Two different size distributions were fitted, a Log-Normal and a Gaussian. The results of the distribution fits are presented in Table 7 and Figure 76.

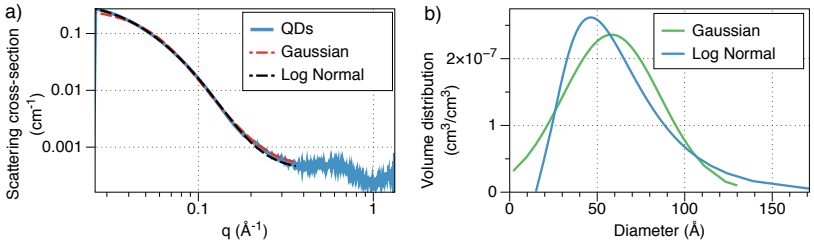


Figure 76: Comparison between Log-Normal (blue) and Gaussian distributions (green) for QDs. a) Spherical form factor fits to scattered intensity b) Corresponding size distributions.

Size distribution	Median	Mean	Standard deviation	χ^2
Gaussian	56±3Å	56±3Å	30Å	132
Log Normal	59±2Å	63±2Å	22Å	10

Table 7: Summary of Log-Normal and Gaussian distributions applied to spherical form factor fits of CdSe/ZnS QDs. The distribution's median, mean, standard deviation and the reduced χ^2 are presented.

Both distributions provide a similar estimate of the median particle size, however a better fit (lower reduced chi squared) is obtained using the Log-Normal distribution. However an unusually large polydispersity (~30%) is observed, due to the absence of form factor features at high q.

Work published by Dabbousi et al suggests the ZnS layer is responsible for smoothing the high q form factor minima, thereby resulting in an overestimate of the core polydispersity [48]. They characterised core-shell CdSe/ZnS QDs using SAXS and TEM for increasing thicknesses

of the ZnS layer [48]. They demonstrate bare uncoated QDs cores with a diameter of 39Å±8.2% (characterised via TEM) with the percentage polydispersity increasing with increasing ZnS layer thickness (Table 15). Their QDs with a 4Å ZnS layer display a peak luminescence at 565nm, resembling the spectra of the QDs used in this paper. Their SAXS scattering data and TEM distributions are reproduced for reference in the appendix (Figure 94 and Table 15). For a ZnS layer of thickness of 4Å, they observe a doubling in the QDs polydispersity to 20% when measured under SAXS compared to TEM. Under TEM the bare CdSe core's display a Gaussian distribution, whilst the ZnS coated core's approach a Log-Normal.

From TEM the diameter of QDs was estimated to be xx+-xx nm (~xx particles counted), agreeing closely with SAXs measurements.

Core-Shell form factor

By taking account the difference in electron density between the CdSe core and ZnS shell, a more accurate estimate of the stock QDs concentration can be made. A core-shell form factor was applied, as described in the Experimental section, using the relative scattering length densities of CdSe, ZnS and water. Core diameter of 5.3nm with a shell thickness of 0.5nm and standard deviation of 2nm (assuming a Log-Normal distribution) can be fitted (Figure 77). Using the fitted volume fractions and mean particle sizes, the molar concentrations of particles can be calculated (Table 8).

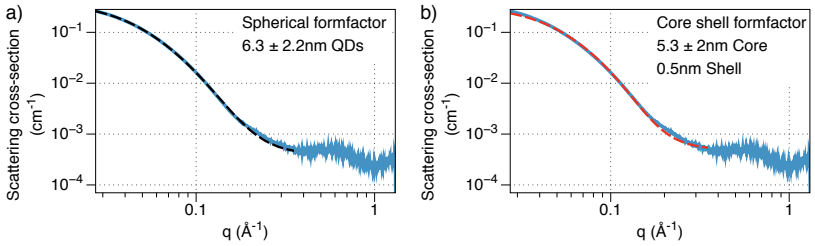


Figure 77: SAXS scattered intensity of CdSe/ZnS QDs fitted using a) Spherical form factor b) Core shell form factor.

Similar mean particle diameters and concentrations of 203±20nM and 220±20nM are obtained when assuming spherical and core-shell form factors respectively. These agree the particle concentration of 210nM calculated from UV-VIS measurements using a manufacturer provided molar extinction coefficient. Both size distributions (Gaussian and Lognormal) and form factors (spherical and core-shell) are demonstrated to provide similar values of particle diameter and concentration. For later modelling of scattering from QDs in this chapter, a spherical form factor and a Log-Normal distribution are used due to their simplicity and lower reduced χ^2.

Optical luminescence

The photo-luminescence of QDs upon transfer to Hepes buffer is presented in Figure 78a. The photo-luminescence of QDs to proportional to their concentration in solution, leading to a reduction in luminescence upon dilution to working concentrations (Figure 78b). When mixed with non associating AuNPs (i.e. Pep-Au without the assembly peptide)

Spherical form factor					
Median (Å)	Mean (Å)	Standard deviation (Å)	Particle Volume fraction (cm^3/cm^3)	Concentration (Mol)	χ^2
59±2	63±2	22±2	$1.6 \pm 0.1 \times 10^{-5}$	203±20nM	10

Core-Shell form factor						
Median core diameter (Å)	Mean core diameter (Å)	Standard deviation (Å)	Shell thickness (Å)	Particle Volume fraction (cm^3/cm^3)	Concentration (Mol)	χ^2
50±2	53±2	20±2	5	$1.8 \pm 0.1 \times 10^{-5}$	220±20nM	56

Table 8: Summary of Spherical and Core-Shell form factor fits and distributions applied to spherical form factor fits of CdSe QDs. The distribution's median, mean, standard deviation and the are presented.

in a ratio of 30:1 (Figure 78c) only a small decrease in luminescence (~3%) occurs. This indicates that the AuNPs and QDs remain dispersed without the assembly peptide as non-radiative energy transfer from QDs to AuNPs has a strong distance dependence. Upon the addition of Pep-Au in a ratio of 30:1 (Figure 78d) a quenching of QDs luminescence to 20% of the original is observed, resulting from the Pep-Au:QDs conjugate formation. No photo-luminesce was observed from solutions of only AuNPs or Pep-Au.

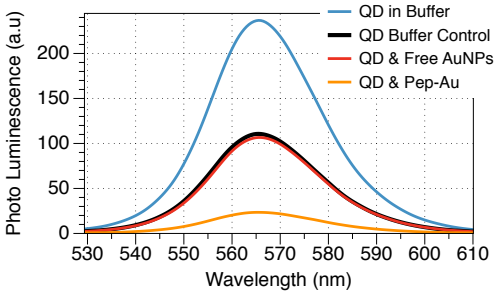


Figure 78: Photoluminescence spectra of QD a) after transfer to HEPEs buffer (—-) b) diluted to working concentrations (—-) c) mixed with non associating AuNPs (—) d) assembled with Pep-Au (—). The AuNP:QDs and Pep-Au:QD ratios are 30:1. Photoluminescence quenching is only observed for the Pep-Au/QDs mixtures indicating assembly of Pep-Au onto the QDs surface.

5.3.2 *Peptide-AuNP*

High resolution TEM images of gold particles (Pep-Au) and corresponding SAXS patterns are presented in Figure 79. The presence of gold particles could be inferred from Titan HR-TEM measurements, however a combination of the particle diameter lying at the boundary

of the machine's resolution and the tendency of the particles to melt under extended viewing prevented the acquisition of an accurate size distribution.

The application of a Guinier fit to the SAXS scattering data from Pep-Au provides an estimated radius of gyration Rg of 0.62nm. Particle size is calculated using a spherical form factor assuming either a Log-Normal or a Gaussian distribution (Table 9). Similar mean diameters and concentrations of 1.2nm (1.2 ± 0.5μM) and 1.3nm (1.0 ± 0.5μM) are obtained for Gaussian and Log-Normal distributions respectively. These are near to concentrations calculated using the manufacture's supplied optical extinction coefficient (1.7μM) and the manufacturer provided particle diameter (1.4nm±10%). The diameter of atomic gold is 0.27nm, indicating that the sample polydispersity is on the scale of ±2 gold atoms [131]. The optical extinction coefficients for gold nanoparticle concentration estimates are typically calculated based on synthesis ingredients (assuming 100% conversion) and a mean particle size [140]. Considering the difficulty in measuring the size distributions of particles on this size scale using TEM, the concentrations reported by SAXS are interpreted as more accurate than UV-VIS estimates. The electron density of gold is considerably higher than the electron density of the peptide, resulting in similar gold particle diameters with and without the attached substrate peptide under SAXS.

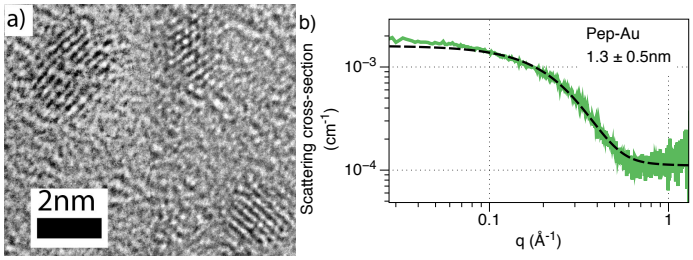


Figure 79: Pep-Au characterised using a) HR-TEM and b) SAXS (green) fitted using a spherical form factor with a Log-Normal distribution (black).

Size distribution	Median	Mean	Standard deviation	Particle Volume fraction (cm^3/cm^3)	Concentration (Mol)	χ^2
Gaussian	12±2Å	12±2Å	6Å	$6.9 \pm 0.2 \times 10^{-7}$	1.2±0.5μM	0.4
Log Normal	12±2Å	13±2Å	5Å	$6.6 \pm 0.2 \times 10^{-7}$	1±0.5μM	0.3

Table 9: Summary of Log-Normal and Gaussian distributions applied to spherical form factor fits of Pep-Au. The distribution's median, mean, standard deviation and the reduced χ^2 are presented.

5.3.3 *Non-interacting mixtures of QDs and Pep-Au*

The SAXS scattered intensity from a mixture of 'n' distinct populations of non interacting particles can be calculated by summating the scat-

tering from each particle population (Section 2.5.7). The mixture of non-interacting QDs and Pep-Au can be therefore simulated by summating the individual scattering profiles of the particles (Figure 80a). The Pep-Au scatters almost two orders of magnitude less than the QDs, however it still has a visible influence on the combined scattering pattern. The larger QDs primarily contribute to scattering at low q (Figure 80a [i]) whilst the smaller gold particles contribute at mid q (Figure 80a [ii]), enabling the two different size populations to be fitted accurately from a single SAXS data-set.

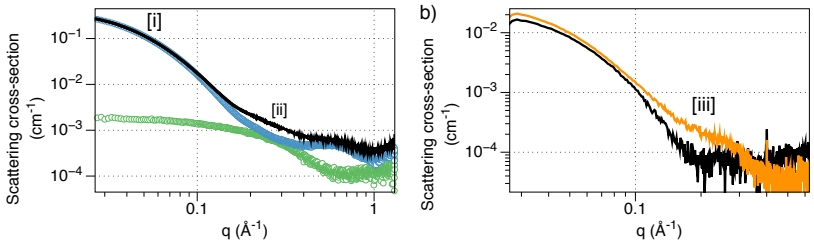


Figure 80: a) Simulated scattering from a non interacting mixture of QDs and Pep-Au. The scattered SAXS intensity from Pep-Au (○) and QDs (□) can be summed to simulate a non interacting two population mixture (—). The QDs primary contribute to scattering at low q ([i]), whereas the Pep-Au contributes at higher q ([ii]). b) Scattering from a control mixture of non-interacting QDs and AuNPs for AuNP:QD ratios of 3:1 (black) and 50:1 (orange). The influence of increasing concentration of AuNPs is visible at higher q [iii].

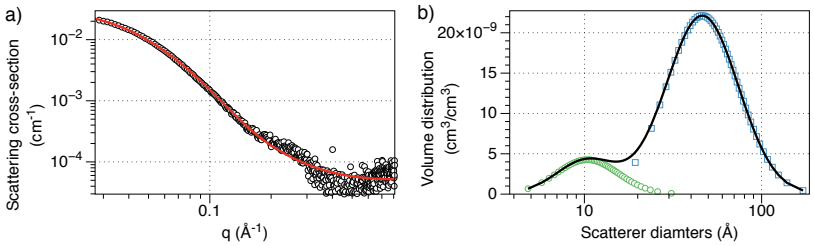


Figure 81: Application of two particle population model to a mixture of non interacting QDs and AuNPs. a) Scattered intensity from the mixture, with an AuNPs:QDs ratio of 50:1 (○), fitted with the two population model (—). b) Volume distributions of population 1 (QDs) (□), population 2 (AuNPs) (○) and the total distribution (—).

To verify this behaviour, control mixtures of QDs and gold nanoparticles (i.e. Pep-Au without the substrate peptide) were characterised (Figures 80b and 81). The particles were mixed in AuNP:QD ratios of 3:1, 25:1 and 50:1; the photo-luminescence of the mixture was not quenched, confirming that the QDs and AuNPs (without substrate peptide) do not associate.

The scattering from the non associating mixtures was fitted with a two population model (m=2). The first population (Pop 1) describes a larger particle population that scatters at low q, with the second population (Pop 2) describing the scattering from smaller particles. Thereby Pop 1 describes the scattering from the QDs and Pop 2 the scattering from the AuNPs. The fitting process involved initially fixing the particle diameters and polydispersities to known values (i.e. those obtained from individual population measures). Then only the volume fraction

of each population was allowed to vary to fit the experimental data. Once a close fit had been achieved, all parameters were allowed to float. However, the population parameters remain the same as those expected for single particles. A close fit is observed between the model and the experimental data (Figure 81a), with the concentrations agreeing with those expected from mixing individual solutions. A spherical form factor rather than a core-shell for Pop 1 (QDs) is deliberately chosen to maintain simplicity during model fitting (Figure 81).

AuNP:QDs ratio	Pop 1 Mean Diameter (QDs)	Pop 1 Volume	Pop 2 Mean Diameter (Pep-Au)	Pop2 Volume
3	63	1×10^{-6}	0	0
25	63	1.14×10^{-6}	13	1×10^{-8}
50	63	1.26×10^{-6}	13	6.8×10^{-8}

Table 10: Summary of two particle population model to a mixture of non interacting QDs and AuNPs.

5.3.4 *Characterization of Urokinase Plasminogen Activator*

SAXS measurements of 1mg/ml uPA in Hepes buffer were performed and fitted using a Regularization technique to generate a pair distribution function and a radius of gyration of 3.1±0.2nm (Chapter 2.5.6) (Figure 82). These results closely match those presented by Behrens et al (Rg = 3.16 ± 0.08nm) [21].

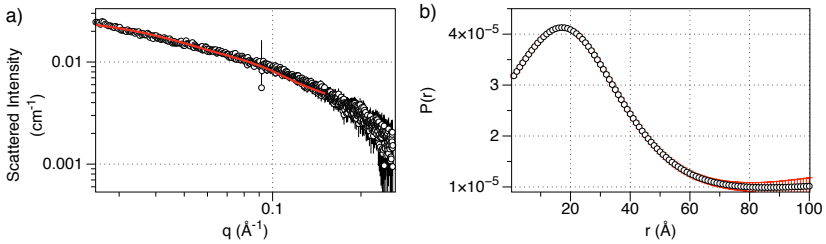


Figure 82: a) SAXS pattern of uPA (black) fitted using a regularization technique (red) b) the generated pair distribution function. A radius of gyration of 3.1±0.2nm is obtained, agreeing with values reported in literature [21].

5.4 PEPTIDE MEDIATED ASSEMBLY OF QDS-PEP-AU CONJUGATES

The introduction of Pep-Au to a solution of QDs, results in the assembly of Pep-Au onto the QD surface. The surface attachment of the Pep-Au, occurs via a ligand exchange between the QDs surface MPA groups and the hexahistidine groups on the Pep-Au. For the conjugate formation experiments, a range of Pep-Au to QDs ratios were investigated. The change in conjugate size was monitored using SAXS and correlated to optical properties via Fluorometry experiments. Two different approaches were taken when performing conjugation experiments. For

the first, the QDs concentration was kept constant at 8nM and the Pep-Au concentration gradually increased, to increase the Pep-Au:QD ratio. The second approach involved keeping the Pep-Au concentration constant at 0.5µM whilst regulating the QDs concentration. For both experiments, the Pep-Au:QD ratio was adjusted from 0:1 to 100:1 through the controlled dilution of the stock solutions. The SAXS patterns for these experiments are presented in Figure 83.

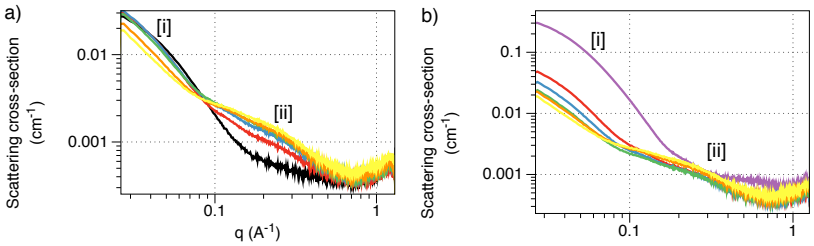


Figure 83: SAXS scattering patterns from conjugate assembly experiments, performed under a) constant QDs concentration b) constant Pep-Au concentration. The Pep-Au:QD ratios are 0:1 (black), 0.5:1 (purple), 25:1 (red), 40:1 (blue), 50:1 (green), 75:1 (orange) and 100:1 (yellow). The change in scattering at low q ([i]), provides information on conjugate size, whereas the scattering at higher q ([ii]) is due to changes in Pep-Au concentration.

5.4.1 *Choice of Conjugate model*

A suitable model is required to fit the SAXS data. The model must be able to describe the physical characteristics of the system whilst still closely fitting the data. The conjugates are expected to display a polydisperse particle/halo morphology (Figure 73a). An exact model would involve describing the Pep-Au/QD conjugate with a particle/halo model described by Zhang et al [253] or a core-shell model applied by Balmer [13]. Zhang's particle/halo model describes three contrast layers, one for the substrate particle, one for the solvent gap and one for the adsorbent particle (Figure 84). The model is applied to investigate charged zirconia nanoparticles surrounding silica microspheres. Balmer applied a similar core/shell model to describe the assembly of silica nanoparticles on latex microspheres, where the shell describes the average scattering length density of both the silica nanoparticles and solvent. Both these models fit scattering from monodisperse particles (<10%). This monodispersity in constituent components provides fine features such as spherical form factor oscillations that allow for more precise fitting of model parameters. Crucially both these models require an estimate of halo/assembly layer electron density to calculate its thickness.

For more polydisperse systems the distinct layers begin to overlap upon ensemble averaging (Figure 73b). The conjugate scattering length density can then be approximated as a single spherical polydisperse particle rather than distinct layers.

We have chosen to model the Pep-Au/QD conjugate by assuming a polydisperse spherical particle rather than a layered structure. A more complicated layered model was found to be unfeasible due to a combination of factors:

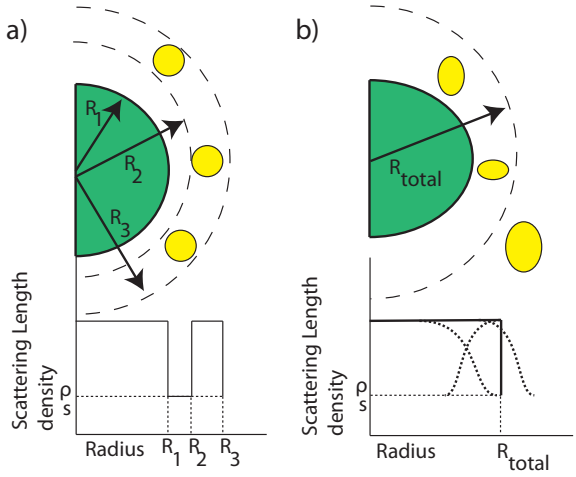


Figure 84: Schematic illustration of scattering length density for a) Halo model described by Zhang et al [253], b) Spherical particle approximation. Zhang's particle/halo model describes three layers, one for the substrate particle, one for the solvent gap and one for the adsorbent particle. When polydispersity and ensemble averaging is introduced, the distinct layers begin to overlap. The conjugate scattering length density can then be approximated as a single spherical particle rather than distinct layers.

CONSTITUENT COMPONENT POLYDISPERSITY: The intrinsic polydispersity in both the QDs (±35%) and Pep-Au (±40%) subunits removes the presence of fine features such as form factor oscillations.

POLYDISPERSE CONJUGATE MORPHOLOGY: The conjugate morphology is likely to be highly polydisperse. In a solution, for any given Pep-Au:QD ratio, there will be variation in the number of Pep-Au per particle across the conjugate population. The Pep-Au is not expected to tether in an ordered manner on the QDs surface. The tethering peptide is expected to have a degree of flexibility, providing a limited mobility to the Pep-Au in the assembly layer. These effects are ensemble averaged across time and particle populations.

ASSEMBLY LAYER ELECTRON DENSITY: Finally a layered model would require the electron densities of the assembly layer to be estimated. The electron density would be calculated from a spatial average of the number of AuNPs over the volume of the assembly layer - hence the electron density and the layer thickness are related parameters and not independent. If the electron density is set too low, the particle diameter would be over estimated. If the electron density is too high, then the diameter is under estimated.

Hence the conjugates are approximate as behaving as polydisperse spheres, with a scattering contrast equal to that of the QD core (i.e. CdSe). This way, instead of seeing a central particle and a surrounding layer, just one particle is seen describing both the Pep-Au cloud and QD core. Under this approximation the calculated conjugate diameters represent an effective electron density weighted mean.

As the Pep-Au in the assembly layer is particulate, the scattering from these spherical structures must be taken into account through the introduction of an addition particle population model [17][13][253].

To summarise the conjugate scattering is fitted using a two population model, with each population described using a spherical form factor with a Log-Normal distribution. The first population (Pop 1) describes a larger particle population that scatters at low q, with the second population (Pop 2) describing the scattering from smaller particles.

When applied to the non-interacting mixture (section 5.3.3), Pop 1 describes scattering from the QDs, whilst Pop 2 describes scattering from AuNPs. For the assembly measurements, Pop 1 describes the effective conjugate size whilst Pop 2 describes scattering from Pep-Au.

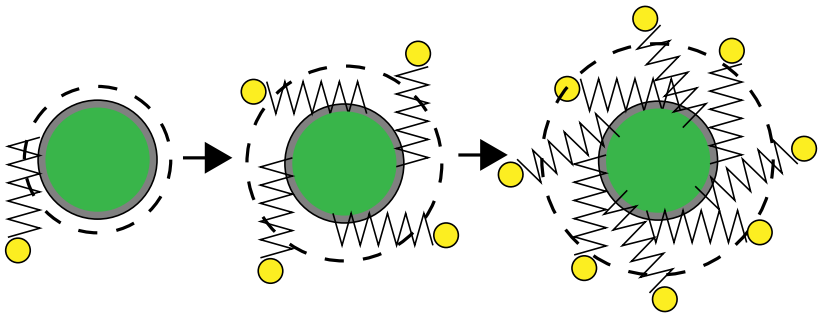


Figure 85: Schematic illustration of Pep-Au:QD conjugate growth. The dashed line represents the effective conjugate size obtained from a spherical particle model. The calculated diameter describes an ensemble and electron density weighted mean.

5.4.2 *Conjugate assembly at constant QD concentration*

For this experiment the QDs concentration was kept constant at 15nM and the Pep-Au concentration gradually increased, to increase the Pep-Au:QD ratio. From the SAXS pattern an increase in form factor gradient is observed at low q, with it shifting to lower q (Figure 83[i]), indicating an increase in particle size. A decrease in the scattering intensity is also observed suggesting either an overall decrease in conjugate electron density or concentration. At higher q an increase in scattering is observed (Figure 83[ii]). From previous modelling of form factors (section 5.3.3), this increase can be attributed to the increase in Pep-Au concentration. This result is consistent considering that the Pep-Au concentration is being increased to increase the Pep-Au ratio.

To further interpret the scattering data, a two population model is applied as described previously. Here Pop 1 describes the electron weighted conjugate size, while Pop 2 describes the scattering from Pep-Au. A precision uncertainty of ±2 is observed on the position of the mean for the bimodal distribution fits. This value is used for the plotted mean measurement error.

Dynamic assembly experiments were performed, however assembly was observed to occur faster than the initial SAXS measurements (<1 min). Work performed by Balmer et al on the assembly of silica nanoparticles onto latex microspheres indicates that assembly occurs on the time scale of seconds [13].

Figure 86 presents the results of the two population model fit to assembled structure, with the exact numbers presented in the chapter

appendix (Table 16). An increase in the effective Pep-Au/QD conjugate diameter (pop 1) occurs with increasing Pep-Au:QD ratio. A linear increase in conjugate size is seen at for Pep-Au:QD ratios upto 30:1, with the conjugate size saturating at higher ratios. At the highest experimentally measured ratio of 100:1, a mean conjugate size of 103Å was obtained. The conjugate volume fraction was observed to decrease with increasing conjugate size. The scattered intensity is a function of both volume fraction and scattering length density. As gold has a higher scattering length density than CdSe (golds contrast in solution is about 13.8 times greater than that of CdSe (section 2.5.7)), an increase in conjugate contrast would be expected for close-packed surface assembly of Pep-Au. As conjugates were oscillated in a capillary during measurements and no precipitation was observed over the experimental time periods, this reduction in volume fraction is interpreted, as an overall reduction in conjugate electron density, due to the incorporation of solvent in the assembly layer. This reduction in coronal electron density has been observed in Balmer's silica/latex conjugates [13]. No structure factor peaks are observed for the assembled conjugates, indicating the absence of long range order. A structure factor (such as Percus-Yevick [16]) was not required, to describe short-range inter-particle correlations such as Pep-Au-Pep-Au interactions, indicating that the surface assembly is relatively disordered.

The size of the second population 2 (Pep-Au) was observed to remain constant at 13Å, matching the diameter obtain from stock solutions, with the volume fraction increasing with increasing Pep-Au:QD ratio, reflecting the increase in Pep-Au concentration.

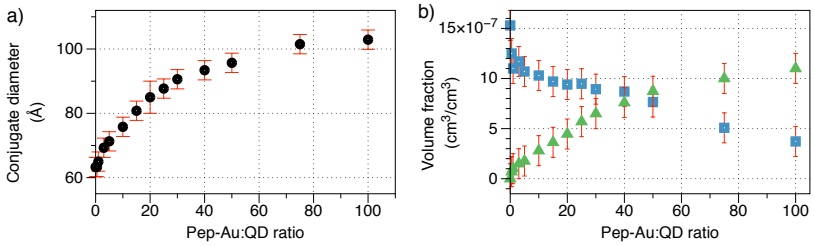


Figure 86: Conjugate growth under constant QD concentration. a) Effective Conjugate diameter (pop 1), b) Volume fractions describing the conjugate (pop 1) and the Pep-Au (pop 2). The Pep-Au (pop 2) was observed to remain constant at 13Å.

5.4.3 *Conjugate assembly constant Peptide-AuNP concentration*

For this experiment, the Pep-Au concentration was fixed at 0.5µM and the QDs concentration adjusted to alter the Pep-Au:QD ratio. An increase in conjugate size is observed with increasing Pep-Au:QD ratio (Figure 87), agreeing closely with values observed under constant QDs concentration experiments (Figure 88). The conjugate volume fraction decreases rapidly with increasing Pep-Au ratio, reflecting the decreasing concentration of QDs in solution. The Pep-Au (pop 2) and the diameter remains constant at 13Å. The Pep-Au volume fraction is observed not to change reflecting the fixed concentration under which the experiments were performed. As the Pep-Au is assembled on the conjugates this demonstrates that conjugates do not precipitate during the course of the experiments.

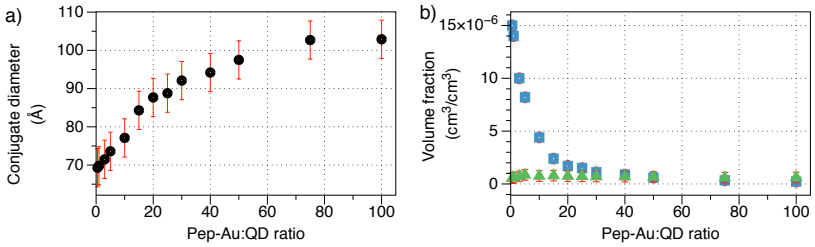


Figure 87: Conjugate growth under constant Pep-Au concentration. a) Effective Conjugate diameter (pop 1), b) Volume fractions describing the conjugate (pop 1) and the Pep-Au (pop 2). The Pep-Au (pop 2) diameter was observed to remain constant at 13Å.

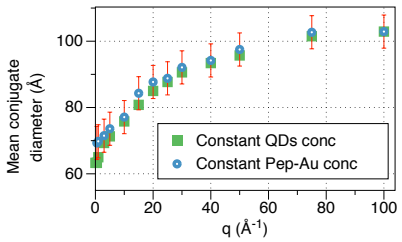


Figure 88: Comparison of effective conjugate mean diameter for experiments performed under constant QDs concentration (■) and constant Pep-Au concentration (●).

5.4.4 *Optical characterisation*

Photoluminescence measurements of Pep-Au/QD conjugates were performed by John Dick, using a Spectramax M5 plate reader (Molecular devices), with the experiments performed under constant QDs concentration. The assembly of Pep-Au onto the surface of QDs quenches their Photoluminescence (Figure 89), with total quenching occurring at a Pep-Au:QD ratio of approximately 30:1.

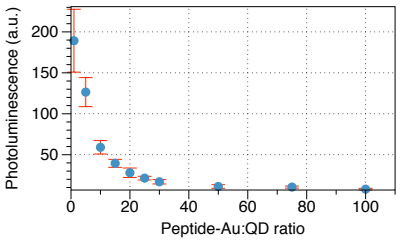


Figure 89: Photoluminescence measurements of Pep-Au/QD conjugates performed under constant QDs concentration.

5.4.5 *Langmuir adsorption*

The conjugate growth as a function of Pep-Au:QD ratio can be fitted with a Langmuir adsorption isotherm, to quantify the binding affinity for Pep-Au on QDs through the calculation of a binding constant K.

The Langmuir adsorption equation relates the surface coverage of adsorbate molecules onto a substrate surface as a function of adsorbate concentration [44][25]. The equation typically has the from:

$$\theta = \frac{Kc}{1 + Kc} \tag{5.1}$$

Where c is the concentration of the adsorbing species and $K = \frac{K_a}{K_d}$ is an equilibrium constant describing the ratio between the analyte rate constant for adsorption (k_a) and dissociation rate (k_d). The fractional coverage (θ) can be described as:

$$\theta = \frac{x}{x_0} \tag{5.2}$$

Were x_0 represents the total concentration of available binding sites on a solid substrate and x is the concentration of occupied sites. An isotherm of θ against concentration describes how the surface sites become saturated with increasing concentration. By combining equations 5.1 and 5.2 the following relationship can be obtained:

$$x = \frac{x_0 Kc}{1 + Kc} \tag{5.3}$$

Describing the concentration of occupied sites, with x_0 and K as fitting parameters. The model assumes that adsorbent species only interact with the surface, that the surface is homogeneous and that adsorption is limited to a monolayer. When applied to growth of a surface layer, the fractional coverage (θ), can also be written as $\theta = \frac{\triangle d}{d_{max}}$, were Δd is the change in layer thickness and d_{max} is the maximum change in thickness upon surface saturation [234]. This allows use to rewrite equation 5.3 as:

$$\triangle d = \frac{d_{max} Kc}{1 + Kc} \tag{5.4}$$

Figure 90 displays the change in conjugate size (Δd) as a function of Pep-Au:QD ratio. The Langmuir equation (equation 5.4) is applied providing values of d_{max} = 49Å and K = 0.042. The isotherm suggests that at the highest measured Pep-Au:QD ratio of 100:1, approximately 80% of available QD surface binding sites are occupied.

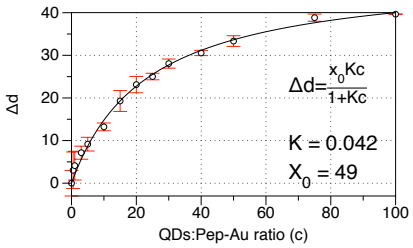


Figure 90: Increase in Conjugate diameter (Δd) as a function of Pep-Au:QD ratio. The data is fitted with an Langmuir adsorption isotherm providing a constant K of 0.042 and a theoretical maximum conjugate diameter increase of d_{max} = 49Å.

Prasuhn and coworkers have investigated the loading of tetrahistidine and octahistidine residues onto the surface of QDs (with peak emittance at 550nm) [191]. Prior to peptide attachment the QDs are stabilised with dihydrolipoic acid to make them water soluble. The peptide surface attachment is characterised using agarose gel electrophoresis. They estimate the footprint of tetrahistidine to be approximately 72Å^2, with a theoretical maximum surface packing density of ~140 peptides per QD. Through comparison with larger proteins (Myoglobin, mCherry and Maltose binding protein) they demonstrate that steric hindrance is a major packing constraint for large biomolecules, with the assembly of smaller peptides pronominally determined by the number of available surface binding sites. As an additional reference, Bawedi et al demonstrated average values of 140 ligands per QD for an analogous system consisting of quantum dots capped with longer DHLA–PEG–amine ligands [139].

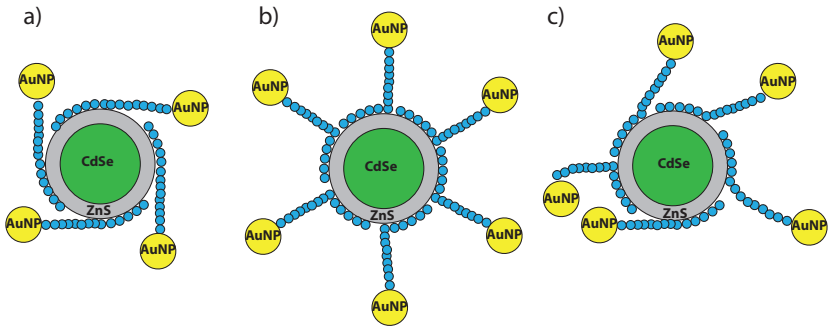


Figure 91: Possible conformations of Pep-Au assembly on the QD surface a) parallel b) perpendicular c) a disordered hybrid structure.

The conformation of Pep-Au on the QD surface must also be considered. The two simplest space filling models of attachment are presented in Figure 91. The parallel conformation orients the Pep-Au flat across the QD surface, where as the perpendicular conformation places the Pep-Au sticking straight out of the surface. A parallel conformation would reduce the steric hinderance between adjacent Pep-Au compared to the parallel orientation. In practice the inherent flexibility offered by the peptide chain is likely to provide a more disordered layer structure lying between the two space filling models (Figure 91c). In a disordered state, there may be a preference towards one space filling model as a function of Pep-Au:QD ratio, where at low Pep-Au:QD ratio the need to minimise surface energy favours a parallel conformation. At higher Pep-Au ratios, steric hinderance and competition for binding sites would favour a more perpendicular conformation.

An estimation of the number of Pep-Au on the surface of QDs can be made from the reduction in effective conjugate electron density. From equation 2.13 the particle fromfactor and hence differential scattering cross-section is proportional to volume fraction and $\triangle\rho^2$. For the assembly of Pep-Au:QDs in a ratio of 100:1, under constant QD concentration a conjugate diameter of 95Å and a volume fraction of $3.7 \times 10^{-7}$is obtained. As a control, the QDs alone demonstrate a diameter of 58.4 Å and a volume fraction of 1.5×10^{-6}. With conjugate formation, the conjugate volume (based on diameter) increases by a factor of 4.4, whilst the volume fraction decreases by a factor of 0.25. The effective scattering length density ($\Delta\rho^2 = \left(\rho_{sample} - \rho_{H_2O}\right)^2$) of

CdSe and Au with respect to water are 1078 and 1.487×10^4 (table 3), hence the contrast of Au in water is 13.8 times greater than CdSe. The approximate volume of a QD (63Å diameter) is $131nm^3$ and the conjugate (diameter 103Å) is $572nm^3$ yields an estimated shell volume of $441nm^3$. For the conjugate, the overall measured scattering length density is the sum of the contributions of constituent materials averaged over the particle volume. The shell is expected to consist primarily of buffer solution (which has been subtracted out) and Pep-Au averaged over the spherical volume. The volume of a single AuNP (1.3nm diameter) is $1.15nm^3$, and the calculated volume of Au in the shell at a contrast of 1.487×10^4 is estimated at $81nm^3$ yielding approximately 70 AuNPs joined to the conjugated at a Pep-Au:QD ratio of 100:1.

5.5 ENZYMATIC DISPERSION OF PEP-AU/QD CONJUGATES

The addition of uPA to the Pep-Au:QD conjugates results in the hydrolysation and cleavage of the substrate peptide, resulting in the conjugate dissociation. Enzymatic dispersion experiments were characterised using SAXS for four different Pep-Au:QD ratios (5:1, 15:1, 30:1 and 50:1). As for assembly experiments, the dispersion experiments were performed under either constant QDs concentration or constant Pep-Au concentration. Assembled conjugates were incubated with 7.5mg/mL uPa for four hours at 38°C prior to characterisation. The experimental results are presented in Figure 92 and Tables 18, 19, 21 and 22. As the enzyme experiments were performed twice, the averaged results are presented in Figure 92. The conjugate mean sizes are observed to remain at ~63Å, indicating complete disassembly upon incubation with uPA for all Pep-Au:QD ratios. Despite complete conjugate disassembly, only a limited recovery of 40-60% of the original luminescence is obtained upon enzyme incubation.

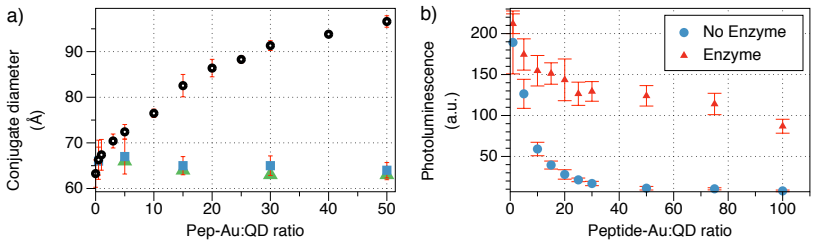


Figure 92: Conjugate size and photoluminescence with and without uPA. a) Diameters for conjugates incubated with uPa under constant QD concentration (■) and constant Pep-Au concentration (▲) for Pep-Au:QD ratios of 5:1, 15:1, 30:1 and 50:1. The dispersion experiments were performed twice, with presented diameters representing averages from both experiments. The averaged conjugate diameters from assembly experiments (○) are overlaid as a reference. b) Photoluminescence measurements of conjugates incubated with (△) and without uPa (●).

To determine whether the limited recovery in luminescence is due to QD precipitation, the volume fractions of Population 1 are compared. When the conjugates are assembled Pop 1 describes the conjugate, whereas when dispersed it represents the QDs. Figure 93a displays the volume fractions of Pop 1 (QDs) for conjugate assembly (○) and enzymatic dispersion (●) under constant QDs concentration; the ho-

rizontal dashed line (- - -) represents the initial QDs volume fraction. A reduction in solution QDs concentration is observed for enzyme dispersion, with the QDs concentration falling to 75% of its original value at a Pep-Au:QDs ratio of 50:1. As a comparison, the Pop 1 (conjugate) volume fraction for assembly experiments is plotted; the volume fraction decreases more rapidly reflecting the incorporation of solvent into the conjugate shell. It should be noted that for conjugate assembly experiments, measurements were taken after 20min of reaction initiation, whereas for disassembly experiments SAXS measurements were taken after four hours. Hence there is considerably more time for conjugates to precipitate under enzyme experiments than under assembly measurements.

Figure 93b compares the QDs volume fraction and photoluminescence for conjugates assembled under constant QD concentration and then incubated with uPa. The results are presented as a percentage of original value (prior to conjugation). Whilst the QDs concentration falls to 75% of its original value (at Pep-Au:QDs 50:1), a far faster fall in photoluminescence recovery (~50%) is witnessed. As the conjugates are observed to completely disassemble, this suggests that there may be other effects responsible for the incomplete recovery.

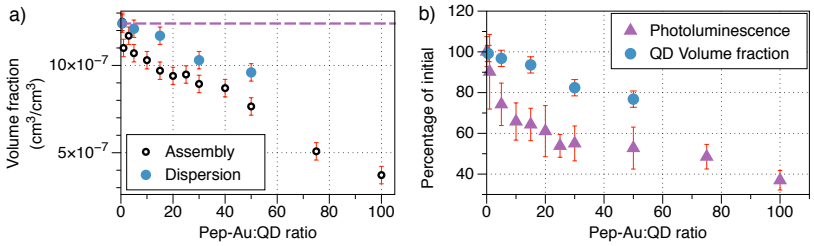


Figure 93: Assessment of sample precipitation a) Pop 1 volume fractions for conjugate assembly (○) and enzymatic dispersion (●) under constant QDs concentration; the horizontal dashed line (- - -) represents the initial QDs volume fraction. b) Comparison of percentage change in volume fraction (●) and photoluminescence (Δ) for enzymatic disassembly under constant QDs concentration.

Small gold nanoparticles (20Å<) are known to act as excellent catalysts as a result of their high surface area and curvature of surface [98][236]. It is possible that the Pep-Au may interact catalytically with QDs when conjugated, preventing full luminescence recovery. Oxidation of QDs leads to a reconstruction of their surface leading to the formation of a electron and hole traps[91][32][182]. Possible oxidation routes involve the production of $CdSeO_2$, $CdSeO_3$ or SeO_2 [237][51], with QDs in aqueous solvents particularly susceptible to degradation. As SAXS measurements indicate full removal of Pep-Au from QD surface, steric hinderance is thought not to be the cause of limited photoluminescence recovery.

5.6 CONTROL MEASUREMENTS

To support conjugate assembly and enzymatic dispersion several control experiments were performed under constant QD concentration and are described bellow.

5.6.1 *Imidazole dispersion*

Imidazole is commonly used to prevent binding of His-taged proteins during purification [206][226][259] and is applied here as a non-enzymatic control for dispersing the Pep-Au:QD conjugates. Mixtures of 200mM and 20mM Imidazole were added to conjugates with Pep-Au:QD ratios of 15:1 and left to equilibrate for four hours prior to analysis. A slight decrease in mean conjugate diameter (~2Å) at 20mM is observed and a larger decrease (8Å) for 200mM Imidazole indicating partial removal of Pep-Au from the QD surface (Table 11).

Population 1: Conjugate		Population 2: Pep-Au
Imidazole concentration	Mean diameter (Å)	Mean Diameter (Å)
0	80.8	13.1
20mM	79	13.1
200mM	73	13.1

Table 11: Imidazole disassembly of conjugates

5.6.2 *Pep-Au with control substrate peptide*

To test the specificity of uPa for the substrate peptide, a control peptide is used with an enzyme recognition sequence specific to MMP7 (Table 6). Monomaleimide functionalized AuNPs were conjugated to the control peptide (ctrl-Pep-Au) and conjugates were allowed to form with ctrl-Pep-Au:QD ratios of 15:1. The ctrl-Pep-Au:QD conjugates form mean diameters of 75Å matching those obtained from Pep-Au:QD conjugates (Table 12).

Assembled control conjugates were then incubated with 7.5 mg/mL uPa for four hours at 38°C prior to characterisation. No change in control conjugate diameter is observed, indicating that uPa is unable to cleave the control substrate peptide.

	Population 1: Conjugate		Population 2: Ctrl-Pep-Au	
	Mean diameter (Å)	Volume fraction (cm^3 / cm^3)	Mean Diameter (Å)	Volume fraction (cm^3 / cm^3)
No uPa	75	4.1×10^{-6}	13	3.8×10^{-7}
uPa	75	4.5×10^{-6}	11	1.4×10^{-6}

Table 12: Conjugates formed using control substrate peptide. The gold substrate peptide is replaced with a control peptide specific only for MMP7. Conjugates with ctrl-Pep-Au:QD ratios of 15:1 are incubated with and without uPA.

5.6.3 *QDs with substrate peptide*

To check whether the substrate peptide has any effect on QD assembly, a control experiment was performed involving mixing quantum dots with the substrate peptide in Pep:QD ratios of 100:1. A population 1 diameter of 63Å is obtained, confirming that the QDs are not aggregated (13). The surface attachment of the substrate peptide is not visible under SAXS due to the low electron density of the peptide.

Population 1: QDs		Population 2: Pep-Au	
Mean diameter (Å)	Volume fraction (cm^3 / cm^3)	Mean Diameter (Å)	Volume fraction (cm^3 / cm^3)
63	1.8×10^{-6}	0	0

Table 13: Control measurement involving Quantum dots and substrate peptide mixed in a Pep:QD ratio of 100:1.

5.6.4 *Mixture of pre-cleaved Peptide-AuNP with QDs*

Control experiments were performed to check for non-specific interactions between cleaved Pep-Au and QDs. The Pep-Au was incubated with uPA for four hours to cleave the substrate peptide. The mixture was then added to QDs, allowed to equilibrate for 20min and characterised using SAXS. No increase in conjugate diameter or quenching in luminescence are observed, indicating no assembly between the QDs and cleaved Pep-Au (Table 14). These results are identical to those obtained from conjugate disassembly experiments, indicating that steric hinderance is not an issue for enzyme cleavage.

Population 1: Conjugate		Population 2: Pep-Au	
Mean diameter (Å)	Volume fraction (cm^3 / cm^3)	Mean Diameter (Å)	Volume fraction (cm^3 / cm^3)
63	1.3×10^{-6}	9.4	2.3×10^{-6}

Table 14: Control experiment of Pre-cleaved Pep-Au and QDs. The Pep-Au was pre-cleaved with uPA prior to addition to QDs.

5.7 CONCLUSION

We demonstrate the surface assembly of gold nanoparticles onto the surface of QDs, measuring growth in conjugate size as a function of Pep-Au:QD ratio using in-situ SAXS. The conjugate mean diameter is found to increase from 63Å to 103Å as the Pep-Au:QD ratio is gradually increased from 0:1 to 100:1. The obtained conjugate diameters reflect an electron density weighted mean.

A decrease in the electron density of the conjugate with increasing Pep-Au:QD ratio is observed, reflecting the incorporation of solvent in the particle halo. A structure factor does not need to be implemented to describe particle-particle interactions, indicating that the assembly halo is disordered. Through the application of a Langmuir isotherm, it is estimated that at a Pep-Au:QD ratio of 100:1, approximately 80% of available binding sites are occupied. These structural changes are correlated to optical properties obtained from fluorescence measurements, with complete luminescence quenching occurring at Pep-Au:QD ratios of 30:1.

Complete conjugate disassembly was observed upon the addition of uPA, however only partial QD luminescence recovery (40-60%) was observed. Whilst SAXS demonstrates complete removal of the gold particles from the quantum dots surface, the fluorescence does not completely return, suggesting that other effects may result in the permanent quenching of QDs.

The use of QDs in aqueous environment is essential for application of their unique optical properties in bioassays and biological imaging. The phase transfer, stabilisation and reversible biomaterial conjugation of QDs in aqueous media modifies their surface. The multi-step nature and complexity of these processes leads to many possible routes for the loss of QD luminescence through the degradation of the QDs surface, introduction of surface carrier trap sites or non specific adsorption of energy acceptors. The work presented here, through the use of synchrotron radiation demonstrates that Pep-Au is fully removed from the surface of QDs and does not limit QD luminescence recovery, via incomplete peptide cleavage or non-specific adsorption of free AuNPs. The work demonstrates that uPA cleavage of Pep-Au is an effective route for the proximal attachment and subsequent complete removal of AuNPs from the QDs surface.

The work presented here can thus act as a guide in the synthesis of general principles for assembly of AuNP-QD conjugates through biomolecular mediated bridging, whilst contributing to the fundamental understanding of the assembly process..

5.8 CHAPTER APPENDIX

5.8.1 *Characterisation of CdSe/ZnS QDs by Dabbousi et al*

Dabbousi et al performed complementary SAXS measurements, observing the ZnS layer to smooth the form factor minima, thereby resulting in an overestimate of the core polydispersity [48]. Their SAXS scattering data and TEM distributions are reproduced in the appendix (Figure 94 and Table 15). The bare CdSe core's display a Gaussian distribution, whilst the ZnS coated core's approach a Log-Normal. This suggests that the use of a Log-Normal distribution better represents the particles' true size distributions.

5.8.2 *Conjugate assembly fits*

Reproduced here are plots and tables detailing bimodal spherical form factor fits applied to conjugate assembly experiments. The experiments were performed under either constant QD concentration or constant Pep-Au concentration.

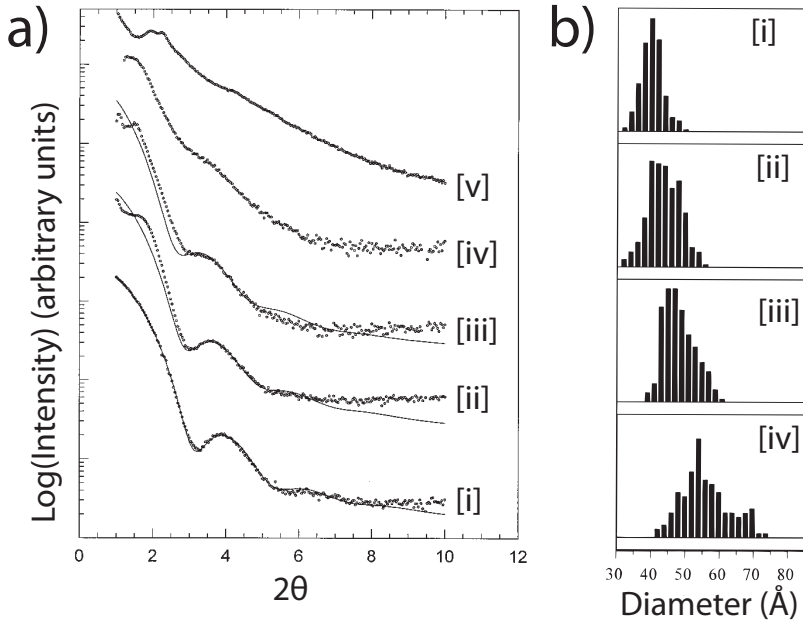


Figure 94: Characterisation of CdSe/ZnS QDs reproduced from Dabbousi et al [48] paper. a) SAXS of bare CdSe QDs and QDs coated with layers of ZnS. The core CdSE diameter is observed to be 42Å±10% [i]. The QDs are coated in ZnS layers of thickness [ii] 2Å, [iii] 4Å, [iv] 8Å, [v] 16Å. b) Corresponding TEM size distributions.

ZnS coverage (TEM)	TEM Diameter	SAXs Diameter
bare CdSe	39Å±8.2%	42Å±10%
2Å	43Å±11%	46Å±13%
4Å	47Å±10%	50Å±18%
8Å	55Å±13%	
16Å	72Å±19%	

Table 15: Summary of the QDs sizes from TEM and SAXS presented by Dabbousi et al [48]. The SAXS particle diameters for 8Å and 16Å ZnS coats are not presented in the paper.

Conjugate assembly under constant QDs concentration

Under constant Pep-Au concentration

5.8.3 *Conjugate disassembly fits*

Reproduced here are tables detailing bimodal spherical form-factor fits applied to enzymatic conjugate dispersion experiments. The experiments were performed under either constant QD concentration or constant Pep-Au concentration.

Constant QDs concentration

Constant Pep-Au concentration

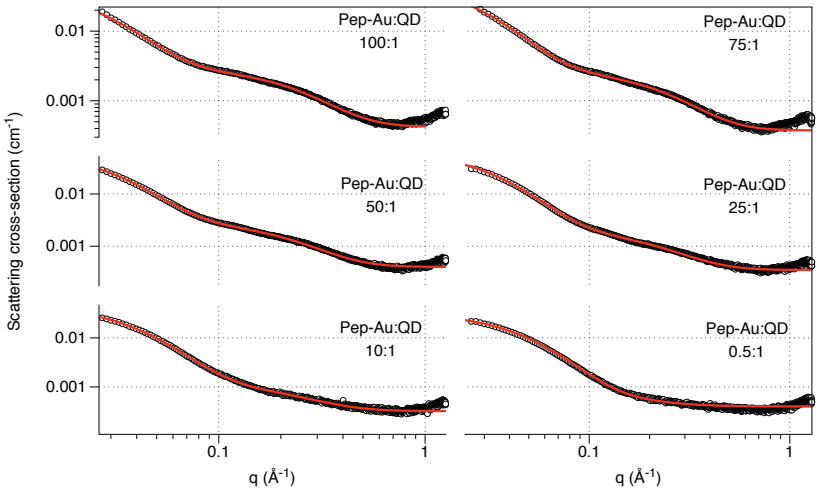


Figure 95: SAXS scattering curves (black) and model fits (red) to conjugate assembly under constant QD concentration.

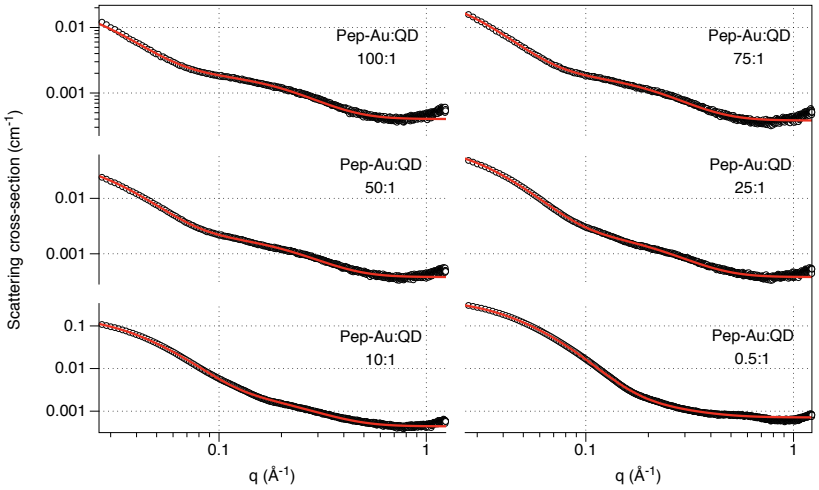


Figure 96: SAXS scattering curves (black) and model fits (red) to conjugate assembly under constant Pep-Au concentration.

Population 1: Conjugate					Population 2: Pep-Au	
Pep-Au:QDs ratio	Median Diameter (Å)	Volume fraction (cm^3 / cm^3)	Mean diameter (Å)	Standard deviation on mean (Å)	Mean Diameter (Å)	Volume fraction (cm^3 / cm^3)
0	58.4±2	1.5E-06	63.3±2	26	13.1±2	0
0.5	58.4±2	1.3E-06	63.3±2	26	13.1±2	7.00E-08
1	60±2	1.1E-06	65.0±2	27	13.1±2	1.00E-07
3	64±2	1.2E-06	69.3±2	29	13.1±2	1.50E-07
5	65.8±2	1.1E-06	71.3±2	30	13.1±2	1.77E-07
10	70±2	1.0E-06	75.8±2	32	13.1±2	2.80E-07
15	74.6±2	9.7E-07	80.8±2	34	13.1±2	3.63E-07
20	78.5±2	9.4E-07	85.0±2	35	13.1±2	4.46E-07
25	81±2	9.5E-07	87.7±2	37	13.1±2	5.70E-07
30	83.6±2	8.9E-07	90.6±2	38	13.1±2	6.50E-07
40	86.2±2	8.7E-07	93.4±2	39	13.1±2	7.60E-07
50	86.5±2	7.7E-07	95.7±2	39	13.1±2	8.73E-07
75	93.7±2	5.1E-07	101.5±2	42	13.1±2	9.06E-07
100	95±2	3.7E-07	102.9±2	43	13.1±2	1.00E-06

Table 16: Conjugate assembly at constant QDs concentration

Population 1: Conjugate					Population 2: Pep-Au	
Pep-Au:QDs ratio	Median Diameter (Å)	Volume fraction (cm^3 / cm^3)	Mean diameter (Å)	Standard deviation on mean (Å)	Mean Diameter (Å)	Volume fraction (cm^3 / cm^3)
0.5	64	1.50E-05	69.3	29	13.1	5.56E-07
1	64.4	1.40E-05	69.8	29	13.1	6.00E-07
3	66	1.00E-05	71.5	30	13.1	7.20E-07
5	67.9	8.20E-06	73.6	31	13.1	8.60E-07
10	71.2	4.40E-06	77.1	32	13.1	7.50E-07
15	77.8	2.40E-06	84.3	35	13.1	7.90E-07
20	81	1.70E-06	87.7	37	13.1	7.45E-07
25	82	1.49E-06	88.8	37	13.1	7.30E-07
30	85	1.10E-06	92.1	38	13.1	7.07E-07
40	87	8.90E-07	94.2	39	13.1	6.90E-07
50	90	6.07E-07	97.5	41	13.1	6.70E-07
75	94.8	3.46E-07	102.7	43	13.1	6.00E-07
100	95	2.27E-07	102.9	43	13.1	6.20E-07

Table 17: Conjugate assembly at constant Pep-Au concentration

Population 1: Conjugate					Population 2: Pep-Au	
Pep-Au:QDs ratio	Median Diameter (Å)	Volume fraction (cm^3 / cm^3)	Mean diameter (Å)	Standard deviation on mean (Å)	Mean Diameter (Å)	Volume fraction (cm^3 / cm^3)
0.5	59±2	1.2E-06	64±2	27	7.7±2	2.3E-06
5	59±2	1.2E-06	64±2	27	8.1±2	2.1E-06
15	58±2	1.2E-06	63±2	26	8.4±2	2.3E-06
30	58±2	1.0E-06	63±2	26	9.2±2	2.3E-06
50	58±2	9.6E-07	63±2	26	9.7±2	2.4E-06

Table 18: Enzymatic dispersion of conjugates under constant QD concentration, experiment 1.

Population 1: Conjugate					Population 2: Pep-Au	
Pep-Au:QDs ratio	Median Diameter (Å)	Volume fraction (cm^3 / cm^3)	Mean diameter (Å)	Standard deviation on mean (Å)	Mean Diameter (Å)	Volume fraction (cm^3 / cm^3)
0.5	63±2	1.1E-06	68±2	28	13.0±2	3.2E-07
5	64±2	1.0E-06	69±2	29	13±2	3.7E-07
15	61±2	1.1E-06	66±2	28	10.0±2	1.0E-06
30	61±2	9.3E-06	66±2	28	10.0±2	1.3E-06
50	61±2	8.5E-06	66±2	27	10.6±2	1.5E-06

Table 19: Enzymatic dispersion of conjugates under constant QD concentration, experiment 2 (repeat).

Population 1: Conjugate					Population 2: Pep-Au	
Pep-Au:QDs ratio	Median Diameter (Å)	Volume fraction (cm^3 / cm^3)	Mean diameter (Å)	Standard deviation on mean (Å)	Mean Diameter (Å)	Volume fraction (cm^3 / cm^3)
0.5	58±2	1.14E-6	63±2	26	8±2	2.7E-6
5	60±2	1E-6	65±2	27	8±2	2.7E-6
30	58.8±2	1E-6	64±2	27	8±2	3.7E-6

Table 20: Enzymatic dispersion of conjugates under constant QD concentration, experiment 3 (repeat).

Population 1: Conjugate					Population 2: Pep-Au	
Pep-Au:QDs ratio	Median Diameter (Å)	Volume fraction (cm^3 / cm^3)	Mean diameter (Å)	Standard deviation on mean (Å)	Mean Diameter (Å)	Volume fraction (cm^3 / cm^3)
5	61±2	7.8E-06	66±2	27	8.3±2	3.2E-06
15	59±2	2.5E-06	64±2	27	8.6±2	2.8E-06
30	59±2	1.2E-06	64±2	27	9.2±2	2.3E-06
50	57±2	7.6E-07	62±2	26	9.0±2	2.4E-06

Table 21: Enzymatic dispersion of conjugates under constant Pep-Au concentration, experiment 1.

Population 1: Conjugate					Population 2: Pep-Au	
Pep-Au:QDs ratio	Median Diameter (Å)	Volume fraction (cm^3 / cm^3)	Mean diameter (Å)	Standard deviation on mean (Å)	Mean Diameter (Å)	Volume fraction (cm^3 / cm^3)
5	62±2	7.1E-06	67±2	28	7.8±2	1.7E-06
15	58±2	2.3E-06	63±2	26	7.5±2	2.4E-07
30	58±2	9.2E-07	63±2	26	7.4±2	2.4E-07
50	58±2	4.8E-07	63±2	26	9.0±2	1.5E-06

Table 22: Enzymatic dispersion of conjugates under constant Pep-Au concentration, experiment 2 (repeat).

Population 1: Conjugate					Population 2: Pep-Au	
Pep-Au:QDs ratio	Median Diameter (Å)	Volume fraction (cm^3 / cm^3)	Mean diameter (Å)	Standard deviation on mean (Å)	Mean Diameter (Å)	Volume fraction (cm^3 / cm^3)
15	60±2	2.2E-6	65±2	27	8±2	3.3E-6
30	58±2	1.3E-6	63±2	27	8±2	3.8E-6
50	59±2	7.8E-7	64±2	27	9±2	2.7E-6

Table 23: Enzymatic dispersion of conjugates under constant Pep-Au concentration, experiment 3 (repeat).

6 SUMMARY

6.1 SUMMARY OF WORK

Designing functional nanomaterials that are able to function effectively in complex environments such as physiological fluids remains a challenge for the scientific community for both in vivo and vitro applications. The goal of this thesis has been to extend and contribute to the fundamental understanding of nanoparticle assembly mediated through biological materials.

Chapter 3 describes the assembly of gold nanoparticles using complementary polypeptides. Synchrotron radiation and optical measurements are used to correlate the AuNP optical properties and assembly structure to the kinetics of assembly. Changes in particle ordering, UV-VIS plasmon shift and aggregation dynamics are observed as a function of linker concentration and particle size. These transitions are related to changes in linker mediated interaction potential, particle surface charge and mobility within the aggregates, providing an insight into the fundamental assembly process.

Further work would involve exploring improvements in assembly order through the use of AuNPs with greater mono-dispersity and shorter or more rigid peptides. Through careful control of JR2EC$_2$ and JR2KC$_2$ concentration, the bridging polypeptide can be formed into fibres, enabling for tight control of the spacing between AuNPs in assemblies. Additionally the sharp optical transition changes for 10nm AuNPs at high linker concentrations has potential in the development of binary bioassays.

The versatility of the polypeptides JR2EC and JR2KC has enabled their incorporation into a liposome-AuNP based assay for the detection of phospholipase [8]. Preliminary SAXS measurements of liposomes with and without JR2KC$_2$ were performed at the Australian synchrotron showing differences liposome morphology due to introduction of the polypeptide. Further SAXS characterisation could be used to understand and optimise the sensitivity of this liposome-AuNP assay.

Chapter 4 describes the interaction of BSA with AuNP aggregates. Bovine serum albumin (BSA) is a vital component of standard immunological assays and it is often extended for use in de-novo assays based on peptide modified metallic nanoparticles. Whilst a wide range of plasma proteins such as BSA and HSA have been shown to associate with nanoparticles, there is little work done on the effect of BSA on NP assembly. Far from being an inert component, the introduction of BSA directly alters the structure and interaction of AuNP aggregates. Temperature is observed to be a factor in these interactions with a specific affinity for hydrophobic systems. Taking account of these effects is essential for the reliable implementation of nanoparticles in environments containing serum albumin. Further work could involve investigating the interaction of serum albumin in NP systems that use peptide cross-linkers. It may also be worth investigating if serum albumin can sacrificially pacify exposed areas of metallic nanoparticles, preventing the degradation of subsequently introduced analytes.

Chapter 5 describes the synchrotron characterisation of a Quantum Dot - Gold Nanoparticle conjugate assay for the detection of urokinase plasminogen activator (uPA). The surface assembly of gold nanoparticles onto the surface of quantum dots is demonstrated, with complete conjugate disassembly upon the addition of the enzyme uPA. A limited QD luminescence recovery (~40% or original) is demonstrated upon enzyme addition. Cleaved AuNPs are demonstrated not to bind to the QDs surface non-specifically indicating the limited luminescence recovery is due to other effects. To the authors knowledge, this is the first time that the in-situ assembly of gold nanoparticles onto the surface of QDs has been monitored using small angle x-ray scattering.

The work presented in this thesis is designed to provide general principles for the biomolecular mediated assembly of metallic NPs, whilst contributing to the fundamental understanding of the assembly process.

BIBLIOGRAPHY

[1] Lego timeline, 1932-1939 http://www.lego.com/eng/info/. (Cited on page 2.)

[2] M.D. Abramoff, P.J. Magalhaes, and S.J. Ram. Image processing with imagej. *Biophotonics international*, 11(7):36–42, 2004. (Cited on page 47.)

[3] D. Aili and M. M. Stevens. Bioresponsive peptide-inorganic hybrid nanomaterials. *Chemical Society Reviews*, 39(9):3358–3370, 2010. (Cited on pages 6, 9, 45, and 46.)

[4] D Aili, FI Tai, K Enander, L Baltzer, and B Liedberg. Self-assembly of fibers and nanorings from disulfide-linked helix–loop–helix polypeptides. (Cited on pages 10, 46, 48, and 50.)

[5] D. Aili, K. Enander, J. Rydberg, I. Lundstrom, L. Baltzer, and B. Liedberg. Aggregation-induced folding of a de novo designed polypeptide immobilized on gold nanoparticles. *Journal of the American Chemical Society*, 128(7):2194–2195, 2006. (Cited on pages 7 and 58.)

[6] D Aili, K Enander, L Baltzer, and B Liedberg. Assembly of polypeptide-functionalized gold nanoparticles through a heteroassociation-and folding-dependent bridging. *Nano letters*, 8(8):2473–2478, 2008. (Cited on pages 11, 45, 46, 48, 69, and 75.)

[7] D. Aili, K. Enander, J. Rydberg, I. Nesterenko, F. Bjorefors, L. Baltzer, and B. Liedberg. Folding induced assembly of polypeptide decorated gold nanoparticles. *Journal of the American Chemical Society*, 130(17):5780–5788, 2008. (Cited on pages 13, 46, and 69.)

[8] D Aili, M Mager, D Roche, and MM Stevens. Hybrid nanoparticle-liposome detection of phospholipase activity. 2010. (Cited on pages 61, 62, 81, and 113.)

[9] A. Paul Alivisatos, Kai P. Johnsson, Xiaogang Peng, Troy E. Wilson, Colin J. Loweth, Marcel P. Bruchez, and Peter G. Schultz. Organization of 'nanocrystal molecules' using dna. *Nature*, 382 (6592):609–611, 1996. (Cited on pages 7 and 45.)

[10] A.P. Alivisatos. Semiconductor clusters, nanocrystals, and quantum dots. *Science*, 271(5251):933, 1996. (Cited on pages 3 and 85.)

[11] P.A. Andreasen, L. Kjøller, L. Christensen, and M.J. Duffy. The urokinase-type plasminogen activator system in cancer metastasis: a review. *International Journal of Cancer*, 72(1):1–22, 1997. (Cited on page 83.)

[12] J.N. Anker, W.P. Hall, O. Lyandres, N.C. Shah, J. Zhao, and R.P. Van Duyne. Biosensing with plasmonic nanosensors. *Nature materials*, 7(6):442–453, 2008. ISSN 1476-1122. (Cited on pages 3, 5, and 67.)

[13] J.A. Balmer, O.O. Mykhaylyk, S.P. Armes, J.P.A. Fairclough, A.J. Ryan, J. Gummel, M.W. Murray, K.A. Murray, and N.S.J. Williams. Time-resolved small-angle x-ray scattering studies of polymer-silica nanocomposite particles: Initial formation and subsequent silica redistribution. *Journal of the American Chemical Society*, 2011. (Cited on pages 95, 97, and 98.)

[14] L. Baltzer, H. Nilsson, and J. Nilsson. De novo design of proteins what are the rules? *Chemical Reviews*, 101(10):3153–3164, 2001. (Cited on pages 9 and 46.)

[15] HHM Balyuzi. Analytic approximation to incoherently scattered x-ray intensities. *Acta Crystallographica Section A: Crystal Physics, Diffraction, Theoretical and General Crystallography*, 31(5):600–602, 1975. (Cited on page 36.)

[16] RJ Baxter. Percus Yevick equation for hard spheres with surface adhesion. *The Journal of Chemical Physics*, 49:2770, 1968. (Cited on pages 42, 57, 77, and 98.)

[17] G Beaucage. Approximations leading to a unified exponential power-law approach to small-angle scattering. *Journal of Applied Crystallography*, 28:717–728, 1995. (Cited on pages 33 and 97.)

[18] G Beaucage. Small-angle scattering from polymeric mass fractals of arbitrary mass-fractal dimension. *Journal of Applied Crystallography*, 29:134–146, 1996. (Cited on page 33.)

[19] G. Beaucage, S. Rane, S. Sukumaran, MM Satkowski, LA Schechtman, and Y. Doi. Persistence length of isotactic poly (hydroxy butyrate). *Macromolecules*, 30(14):4158–4162, 1997. (Cited on page 33.)

[20] G. Beaucage, HK Kammler, and SE Pratsinis. Particle size distributions from small-angle scattering using global scattering functions. *Journal of applied crystallography*, 37(4):523–535, 2004. (Cited on page 33.)

[21] M.A. Behrens, K.A. Botkjaer, S. Goswami, C.L.P. Oliveira, J.K. Jensen, C.R. Schar, P.J. Declerck, C.B. Peterson, P.A. Andreasen, and J.S. Pedersen. Activation of the zymogen to urokinase-type plasminogen activator is associated with increased interdomain flexibility. *Journal of Molecular Biology*, 2011. (Cited on page 94.)

[22] D. Bendedouch and S.H. Chen. Structure and interparticle interactions of bovine serum albumin in solution studied by small-angle neutron scattering. *The Journal of Physical Chemistry*, 87(9):1473–1477, 1983. (Cited on page 72.)

[23] R. Bienert and F. Emmerling. The size distribution of 'gold standard' nanoparticles. *Analytical and Bioanalytical Chemistry*, 395(6):1651–1660, 2009. (Cited on pages 26, 38, and 61.)

[24] P. Bihari, M. Vippola, S. Schultes, M. Praetner, A. Khandoga, C. Reichel, C. Coester, T. Tuomi, M. Rehberg, and F. Krombach. Optimized dispersion of nanoparticles for biological in vitro and in vivo studies. *Particle and Fibre Toxicology*, 5(1):14, 2008. (Cited on pages 67 and 68.)

[25] KS Birdi. Handbook of surface and colloid chemistry. *Handbook of surface and colloid chemistry*, (Ed. 2), 2003. (Cited on pages 73 and 100.)

[26] V. Bloomfield. The structure of bovine serum albumin at low ph*. *Biochemistry*, 5(2):684–689, 1966. (Cited on page 68.)

[27] D.N. Bolon, C.A. Voigt, and S.L. Mayo. De novo design of biocatalysts. *Current opinion in chemical biology*, 6(2):125–129, 2002. (Cited on pages 9 and 46.)

[28] Redouane. Borsali and R Pecora. *Soft-matter characterization*. Springer. (Cited on pages 16, 18, and 34.)

[29] S.H. Brewer, W.R. Glomm, M.C. Johnson, K. Magne, and S. Franzen. Probing bsa binding to citrate-coated gold nanoparticles and surfaces. *Langmuir*, 21(20):9303–9307, 2005. (Cited on page 8.)

[30] J.J. Brown, J.A. Porter, C.P. Daghlian, and U.J. Gibson. Ordered arrays of amphiphilic gold nanoparticles in langmuir monolayers. *Langmuir*, 17(26):7966–7969, 2001. (Cited on page 7.)

[31] M. Brust, M. Walker, D. Bethell, D.J. Schiffrin, and R. Whyman. Synthesis of thiol-derivatised gold nanoparticles in a two-phase liquid–liquid system. *J. Chem. Soc., Chem. Commun.*, (7):801–802, 1994. (Cited on page 5.)

[32] C. Bullen and P. Mulvaney. The effects of chemisorption on the luminescence of cdse quantum dots. *Langmuir*, 22(7):3007–3013, 2006. (Cited on page 103.)

[33] L. Carbone, L. Manna, and C. S
"onnichsen. Self-assembly of amphiphilic nanocrystals. *Angewandte Chemie International Edition*, 48(24):4282–4283, 2009. (Cited on page 6.)

[34] D.C. Carter and J.X. Ho. Structure of serum albumin. *Advances in protein chemistry*, 45:153–204, 1994. ISSN 0065-3233. (Cited on pages 67 and 68.)

[35] V. Castelletto, M.J. Krysmann, L.A. Clifton, J. Lambourne, and L. Noirez. Structural study of bsa/poly (ethylene glycol) lipid conjugate complexes. *The Journal of Physical Chemistry B*, 111(38): 11330–11336, 2007. (Cited on page 73.)

[36] T. Cedervall, I. Lynch, S. Lindman, T. Berggård, E. Thulin, H. Nilsson, K.A. Dawson, and S. Linse. Understanding the nanoparticle–protein corona using methods to quantify exchange rates and affinities of proteins for nanoparticles. *Proceedings of the National Academy of Sciences*, 104(7):2050, 2007. (Cited on page 8.)

[37] W.C.W. Chan, D.J. Maxwell, X. Gao, R.E. Bailey, M. Han, and S. Nie. Luminescent quantum dots for multiplexed biological detection and imaging. *Current Opinion in Biotechnology*, 13(1): 40–46, 2002. (Cited on pages 4 and 83.)

[38] SH Chen, J Rouch, F Sciortino, and P Tartaglia. Static and dynamic properties of water-in-oil microemulsions near the critical and percolation points. *Journal of Physics: Condensed Matter*, 6:10855, 1994. (Cited on pages 42 and 57.)

[39] G. Cheng, V. Castelletto, CM Moulton, GE Newby, and IW Hamley. Hydrogelation and self-assembly of fmoc-tripeptides: unexpected influence of sequence on self-assembled fibril structure, and hydrogel modulus and anisotropy. *Langmuir*, 26(7):4990–4998, 2010. (Cited on page 70.)

[40] M.H. Chowdhury, A.M. Julian, C.J. Coates, and G.L. Coté. Detection of differences in oligonucleotide-influenced aggregation of colloidal gold nanoparticles using absorption spectroscopy. *Journal of Biomedical Optics*, 9:1347, 2004. (Cited on page 23.)

[41] A.R. Clapp, I.L. Medintz, B.R. Fisher, G.P. Anderson, and H. Mattoussi. Can luminescent quantum dots be efficient energy acceptors with organic dye donors? *Journal of the American Chemical Society*, 127(4):1242–1250, 2005. (Cited on pages 4 and 13.)

[42] A.R. Clapp, I.L. Medintz, H.T. Uyeda, B.R. Fisher, E.R. Goldman, M.G. Bawendi, and H. Mattoussi. Quantum dot-based multiplexed fluorescence resonance energy transfer. *Journal of the American Chemical Society*, 127(51):18212–18221, 2005. (Cited on pages 4 and 85.)

[43] D.G. Cornell, D.L. Patterson, and N. Hoban. The interaction of phospholipids in monolayers with bovine serum albumin and [alpha]-lactalbumin adsorbed from solution. *Journal of colloid and interface science*, 140(2):428–435, 1990. (Cited on page 68.)

[44] T. Cosgrove. *Colloid science: principles, methods and applications*. Wiley-Blackwell, 2010. (Cited on pages 1, 6, 16, 18, 73, 75, and 100.)

[45] D.T. Cromer and D.A. Liberman. Anomalous dispersion calculations near to and on the long-wavelength side of an absorption edge. *Acta Crystallographica Section A: Crystal Physics, Diffraction, Theoretical and General Crystallography*, 37(2):267–268, 1981. (Cited on page 36.)

[46] D.T. Cromer and JT Waber. Scattering factors computed from relativistic dirac-slater wave functions. *Acta Crystallographica*, 18 (1):104–109, 1965. (Cited on page 36.)

[47] J.R. Crowther. *The ELISA guidebook*, volume 149. Humana Pr Inc, 2001. (Cited on page 67.)

[48] BO Dabbousi, J. Rodriguez-Viejo, FV Mikulec, JR Heine, H. Mattoussi, R. Ober, KF Jensen, and MG Bawendi. (cdse) zns core-shell quantum dots: synthesis and characterization of a size series of highly luminescent nanocrystallites. *The Journal of Physical Chemistry B*, 101(46):9463–9475, 1997. (Cited on pages xvii, xviii, 4, 5, 89, 90, 106, and 107.)

[49] M.C. Daniel and D. Astruc. Gold nanoparticles: assembly, supramolecular chemistry, quantum-size-related properties, and applications toward biology, catalysis, and nanotechnology. *Chemical Reviews*, 104(1):293–346, 2004. (Cited on page 5.)

[50] CG De Kruif, PW Rouw, WJ Briels, MHG Duits, A Vrij, and RP May. Adhesive hard-sphere colloidal dispersions. a small-angle neutron-scattering study of stickiness and the structure factor. *Langmuir*, 5(2):422–428, 1989. (Cited on pages 42 and 57.)

[51] S. Dembski, C. Graf, T. Kr
"uger, U. Gbureck, A. Ewald, A. Bock, and E. R
"uhl. Photoactivation of cdse/zns quantum dots embedded in silica colloids. *Small*, 4(9):1516–1526, 2008. (Cited on page 103.)

[52] S. Doniach. Changes in biomolecular conformation seen by small angle X-ray scattering. *Chemical Reviews*, 101(6):1763–1778, 2001. ISSN 0009-2665. (Cited on pages 34, 48, and 49.)

[53] K.E. Drexler. Molecular engineering: an approach to the development of general capabilities for molecular manipulation. *Proceedings of the national Academy of Sciences*, 78(9):5275, 1981. (Cited on page 68.)

[54] M.J. Duffy, T.M. Maguire, E.W. McDermott, and N. O'Higgins. Urokinase plasminogen activator: a prognostic marker in multiple types of cancer. *Journal of surgical oncology*, 71(2):130–135, 1999. (Cited on pages 83 and 84.)

[55] R Elghanian, JJ Storhoff, RC Mucic, RL Letsinger, and CA Mirkin. Selective colorimetric detection of polynucleotides based on the distance-dependent optical properties of gold nanoparticles. *Science*, 277(5329):1078, 1997. (Cited on page 11.)

[56] K Enander, D Aili, L Baltzer, I Lundstrom, and B Liedberg. Alpha-helix-inducing dimerization of synthetic polypeptide scaffolds on gold. *Langmuir*, 21(6):2480–2487, 2005. (Cited on pages 10, 46, and 69.)

[57] E. Eteshola and D. Leckband. Development and characterization of an elisa assay in pdms microfluidic channels. *Sensors and Actuators B: Chemical*, 72(2):129–133, 2001. (Cited on page 67.)

[58] S. Eustis and M.A. El-Sayed. Why gold nanoparticles are more precious than pretty gold: Noble metal surface plasmon resonance and its enhancement of the radiative and nonradiative properties of nanocrystals of different shapes. *Chem. Soc. Rev.*, 35(3):209–217, 2005. (Cited on pages 19 and 58.)

[59] S. Eustis and M.A. El-Sayed. Why gold nanoparticles are more precious than pretty gold: Noble metal surface plasmon resonance and its enhancement of the radiative and nonradiative properties of nanocrystals of different shapes. *Chemical Society Reviews*, 35 (3):209–217, 2006. ISSN 0306-0012. (Cited on page 5.)

[60] T.A. Ezquerra, M.C. Garcia-Gutierrez, and A. Nogales. *Applications of synchrotron light to scattering and diffraction in materials and life sciences*. Springer Verlag, 2009. ISBN 354095967X. (Cited on pages 26, 40, 49, 54, and 57.)

[61] J. Ferlay, P. Autier, M. Boniol, M. Heanue, M. Colombet, and P. Boyle. Estimates of the cancer incidence and mortality in europe in 2006. *Annals of oncology*, 18(3):581, 2007. (Cited on page 83.)

[62] S Förster, A Timmann, C Schellbach, A Frömsdorf, A Kornowski, H Weller, SV Roth, and P Lindner. Order causes secondary bragg peaks in soft materials. *Nature Materials*, 6(11):888–893, 2007. (Cited on page 59.)

[63] D. Frenkel. Colloidal crystals: Plenty of room at the top. *Nature materials*, 5(2):85–86, 2006. (Cited on page 11.)

[64] Y. Gao and Z. Tang. Design and application of inorganic nanoparticle superstructures: Current status and future challenges. *Small*. (Cited on pages 6 and 9.)

[65] D Gazzillo and A Giacometti. Structure factors for the simplest solvable model of polydisperse colloidal fluids with surface adhesion. *The Journal of Chemical Physics*, 113:9837, 2000. (Cited on pages 42 and 57.)

[66] J.E. Ghadiali, B.E. Cohen, and M.M. Stevens. Protein kinase-actuated resonance energy transfer in quantum dot- peptide conjugates. *ACS nano*, 2010. (Cited on page 4.)

[67] P. Ghosh, G. Han, M. De, C. K. Kim, and V. M. Rotello. Gold nanoparticles in delivery applications. *Advanced Drug Delivery Reviews*, 60(11):1307–1315, 2008. (Cited on page 45.)

[68] C.E. Giacomelli and W. Norde. The adsorption-desorption cycle. reversibility of the bsa-silica system. *Journal of colloid and interface science*, 233(2):234–240, 2001. (Cited on page 70.)

[69] O. Glatter and O. Kratky. *Small angle X-ray scattering*, volume 69. Academic Press London, 1982. (Cited on pages 15, 26, and 32.)

[70] V. Goertz, N. Dingenouts, and H. Nirschl. Comparison of nanometric particle size distributions as determined by saxs, tem and analytical ultracentrifuge. *Particle & Particle Systems Characterization*, 26(1-2):17–24, 2009. (Cited on page 26.)

[71] R. Greene and J. Elffers. *The 48 laws of power*. Penguin Putnam, 2000. ISBN 0140280197. (Cited on page ix.)

[72] TCJ Gribnau, JHW Leuvering, and H. Van Hell. Particle-labelled immunoassays: a review. *Journal of Chromatography B: Biomedical Sciences and Applications*, 376:175–189, 1986. (Cited on page 9.)

[73] M. Grzelczak, J. Pérez-Juste, P. Mulvaney, and L.M. Liz-Marzán. Shape control in gold nanoparticle synthesis. *Chem. Soc. Rev.*, 37 (9):1783–1791, 2008. (Cited on page 5.)

[74] J.B. Guilbaud and A. Saiani. Using small angle scattering (SAS) to structurally characterise peptide and protein self-assembled materials. *Chem. Soc. Rev.*, 2010. (Cited on page 49.)

[75] A. Guinier, G. Fournet, CB Walker, and G.H. Vineyard. Small-Angle Scattering of X-Rays. *Physics Today*, 9:38, 1956. (Cited on pages 26, 39, 40, and 54.)

[76] T.H. Ha, H.J. Koo, and B.H. Chung. Shape-controlled syntheses of gold nanoprisms and nanorods influenced by specific adsorption of halide ions. *The Journal of Physical Chemistry C*, 111(3):1123–1130, 2007. (Cited on page 11.)

[77] B. Hammouda. Probing nanoscale structures the sans toolbox. *National Institute of Standards and Technology*, 2008. (Cited on pages xiv, 26, 28, and 41.)

[78] E. Hao, G.C. Schatz, and J.T. Hupp. Synthesis and optical properties of anisotropic metal nanoparticles. *Journal of Fluorescence*, 14 (4):331–341, 2004. (Cited on pages 5 and 19.)

[79] WF Harrington, P. Johnson, and RH Ottewill. Bovine serum albumin and its behaviour in acid solution. *Biochemical Journal*, 62(4):569, 1956. (Cited on page 68.)

[80] R.B. Hill, P. Daniel, A. Lombardi, and W.F. DeGrado. De novo design of helical bundles as models for understanding protein folding and function. *Accounts of chemical research*, 33(11):745–754, 2000. (Cited on pages 9 and 46.)

[81] M.A. Hines and P. Guyot-Sionnest. Synthesis and characterization of strongly luminescing zns-capped cdse nanocrystals. *The Journal of Physical Chemistry*, 100(2):468–471, 1996. (Cited on page 4.)

[82] K. Hirayama, S. Akashi, M. Furuya, and K. Fukuhara. Rapid confirmation and revision of the primary structure of bovine serum albumin by esims and frit-fab lc/ms. *Biochemical and biophysical research communications*, 173(2):639–646, 1990. (Cited on page 67.)

[83] A. Hoshino, K. Fujioka, T. Oku, M. Suga, Y.F. Sasaki, T. Ohta, M. Yasuhara, K. Suzuki, and K. Yamamoto. Physicochemical properties and cellular toxicity of nanocrystal quantum dots depend on their surface modification. *Nano Letters*, 4(11):2163–2169, 2004. (Cited on pages 5 and 13.)

[84] C.J. Huang, Y.H. Wang, P.H. Chiu, M.C. Shih, and T.H. Meen. Electrochemical synthesis of gold nanocubes. *Materials Letters*, 60 (15):1896–1900, 2006. (Cited on page 5.)

[85] TC Huang, H Toraya, TN Blanton, and Y Wu. X-ray powder diffraction analysis of silver behenate, a possible low-angle diffraction standard. *Journal of Applied Crystallography*, 26(2):180–184, 1993. (Cited on pages 29 and 47.)

[86] YY Huang, HL Chen, and T Hashimoto. Face-centered cubic lattice of spherical micelles in block copolymer/homopolymer blends. *Macromolecules*, 36(3):764–770, 2003. (Cited on pages xvii, 40, 42, 55, and 57.)

[87] A. Hullmann. Who is winning the global nanorace? *Nature Nanotechnology*, 1(2):81, 2006. (Cited on page 1.)

[88] A. Hullmann. Measuring and assessing the development of nanotechnology. *Scientometrics*, 70(3):739–758, 2007. (Cited on page 1.)

[89] S.J. Hurst, M.S. Han, A.K.R. Lytton-Jean, and C.A. Mirkin. Screening the sequence selectivity of dna-binding molecules using a gold nanoparticle-based colorimetric approach. *Analytical chemistry*, 79(18):7201–7205, 2007. (Cited on pages 11 and 45.)

[90] J. Ilavsky and P.R. Jemian. Irena: tool suite for modeling and analysis of small-angle scattering. *Journal of Applied Crystallography*, 42(2):347–353, 2009. ISSN 0021-8898. (Cited on pages 30, 33, 36, 42, 53, and 88.)

[91] T.M. Inerbaev, A.E. Masunov, S.I. Khondaker, A. Dobrinescu, A.V. Plamadă, and Y. Kawazoe. Quantum chemistry of quantum dots: Effects of ligands and oxidation. *The Journal of chemical physics*, 131:044106, 2009. (Cited on page 103.)

[92] R. Itri, W. Caetano, L.R.S. Barbosa, and M.S. Baptista. Effect of urea on bovine serum albumin in aqueous and reverse micelle environments investigated by small angle x-ray scattering, fluorescence and circular dichroism. *Brazilian journal of physics*, 34(1): 58–63, 2004. (Cited on page 72.)

[93] P Jain, K Lee, I El-Sayed, and M El-Sayed. Calculated absorption and scattering properties of gold nanoparticles of different size, shape, and .... *J. Phys. Chem. B*, 2006. (Cited on pages 58 and 74.)

[94] EM JAMES and J ALAN. Scattering from fractals. *J. Appl. Cryst*, 20:61–78, 1987. (Cited on pages 11, 12, 32, and 51.)

[95] H. Jans, X. Liu, L. Austin, G. Maes, and Q. Huo. Dynamic light scattering as a powerful tool for gold nanoparticle bioconjugation and biomolecular binding studies. *Analytical chemistry*, 81(22): 9425–9432, 2009. (Cited on page 16.)

[96] TL Jennings, MP Singh, and GF Strouse. Fluorescent lifetime quenching near d= 1.5 nm gold nanoparticles: probing nset validity. *Journal of the American Chemical Society*, 128(16):5462–5467, 2006. (Cited on page 85.)

[97] Z. Ji, X. Jin, S. George, T. Xia, H. Meng, X. Wang, E. Suarez, H. Zhang, E.M.V. Hoek, H. Godwin, et al. Dispersion and stability optimization of tio2 nanoparticles in cell culture media. *Environmental science & technology*, 2010. (Cited on page 67.)

[98] R. Jin. Quantum sized, thiolate-protected gold nanoclusters. *Nanoscale*, 2(3):343–362, 2009. (Cited on pages 3 and 103.)

[99] A.M. Kalsin, M. Fialkowski, M. Paszewski, S.K. Smoukov, K.J.M. Bishop, and B.A. Grzybowski. Electrostatic self-assembly of binary nanoparticle crystals with a diamond-like lattice. *Science*, 312(5772):420, 2006. (Cited on page 6.)

[100] J. Kaplan and WF DeGrado. De novo design of catalytic proteins. *Proceedings of the National Academy of Sciences of the United States of America*, 101(32):11566, 2004. (Cited on pages 9 and 46.)

[101] S.H. Ke, G.S. Coombs, K. Tachias, D.R. Corey, and E.L. Madison. Optimal subsite occupancy and design of a selective inhibitor of urokinase. *Journal of Biological Chemistry*, 272(33):20456, 1997. (Cited on pages 84 and 86.)

[102] M.E. kerman, W.C.W. Chan, P. Laakkonen, S.N. Bhatia, and E. Ruoslahti. Nanocrystal targeting in vivo. *Proceedings of the National Academy of Sciences of the United States of America*, 99(20):12617, 2002. (Cited on page 4.)

[103] M.Y. Khan. Direct evidence for the involvement of domain iii in the nf transition of bovine serum albumin. *Biochemical journal*, 236(1):307, 1986. (Cited on page 68.)

[104] CJ Kiely, J. Fink, M. Brust, D. Bethell, and DJ Schiffrin. Spontaneous ordering of bimodal ensembles of nanoscopic gold clusters. *Nature*, 396(6710):444–446, 1998. (Cited on page 11.)

[105] H.Y. Kim, J.O. Sofo, D. Velegol, M.W. Cole, and A.A. Lucas. Van der waals dispersion forces between dielectric nanoclusters. *Langmuir*, 23(4):1735–1740, 2007. (Cited on page 6.)

[106] T Kim, CH Lee, SW Joo, and K Lee. Kinetics of gold nanoparticle aggregation: experiments and modeling. *Journal of colloid and interface science*, 318(2):238–243, 2008. (Cited on page 60.)

[107] Y.P. Kim, Y.H. Oh, E. Oh, S. Ko, M.K. Han, and H.S. Kim. Energy transfer-based multiplexed assay of proteases by using gold nanoparticle and quantum dot conjugates on a surface. *Analytical chemistry*, 80(12):4634–4641, 2008. (Cited on pages 4 and 13.)

[108] J. Kimling, M. Maier, B. Okenve, V. Kotaidis, H. Ballot, and A. Plech. Turkevich method for gold nanoparticle synthesis revisited. *J. Phys. Chem. B*, 110(32):15700–15707, 2006. (Cited on pages 5, 19, 61, and 70.)

[109] E. Kiss. Temperature dependence of bovine serum albumin adsorption onto a poly (ethylene oxide)-grafted surface. *Colloids and surfaces. A, Physicochemical and engineering aspects*, 76:135–140, 1993. (Cited on pages 68 and 70.)

[110] C. Kittel and P. McEuen. *Introduction to solid state physics*, volume 119. Wiley New York, 1996. (Cited on pages 3 and 84.)

[111] R Klein and P Meakin. Universality in colloid aggregation. *Nature*, 339, 1989. (Cited on page 32.)

[112] V.I. Klimov. *Nanocrystal quantum dots*. CRC Press, 2010. (Cited on pages 84 and 85.)

[113] S. R. Kline. Sans model function documentation. (Cited on page 41.)

[114] Steven R Kline. Reduction and analysis of sans and usans data using igor pro. *J Appl Crystallogr*, 39(6):895–900, 2006. (Cited on pages 41 and 42.)

[115] L. Koh. *Investigations of bio-responsive peptide-inorganic nanomaterials*. Phd thesis, Faculty of Engineering and Materials, Imperial College, http://hdl.handle.net/10044/1/1376, 2008. (Cited on pages 70, 71, 72, and 74.)

[116] M. Kondon, J. Kim, N. Udawatte, and D. Lee. Origin of size-dependent energy transfer from photoexcited cdse quantum dots to gold nanoparticles. *The Journal of Physical Chemistry C*, 112(17): 6695–6699, 2008. (Cited on page 85.)

[117] U. Kreibig and C. Fragstein. The limitation of electron mean free path in small silver particles. *Zeitschrift für Physik A Hadrons and Nuclei*, 224(4):307–323, 1969. (Cited on page 20.)

[118] U. Kreibig and L. Genzel. Optical absorption of small metallic particles. *Surface Science*, 156:678–700, 1985. (Cited on page 20.)

[119] U. Kreibig and M. Vollmer. Optical properties of metal clusters. 1995. (Cited on page 20.)

[120] S. Kumar and R. Nussinov. How do thermophilic proteins deal with heat? *Cellular and molecular life sciences*, 58(9):1216–1233, 2001. (Cited on page 69.)

[121] J. Largo, JR Solana, SB Yuste, and A. Santos. Pair correlation function of short-ranged square-well fluids. *The Journal of chemical physics*, 122:084510, 2005. (Cited on page 41.)

[122] A. Laromaine, L. Koh, M. Murugesan, R.V. Ulijn, and M.M. Stevens. Protease-triggered dispersion of nanoparticle assemblies. *Journal of the American Chemical Society*, 129(14):4156–4157, 2007. (Cited on pages 23, 24, 70, 71, 72, and 74.)

[123] C.Y. Lau, H. Duan, F. Wang, C.B. He, H.Y. Low, and J.K.W. Yang. Enhanced ordering in gold nanoparticles self-assembly through excess free ligands. *Langmuir*, 2011. (Cited on page 7.)

[124] J.S. Lee, P.A. Ulmann, M.S. Han, and C.A. Mirkin. A dna-gold nanoparticle-based colorimetric competition assay for the detection of cysteine. *Nano letters*, 8(2):529–533, 2008. (Cited on pages 11 and 45.)

[125] C.T. Lee Jr, K.A. Smith, and T.A. Hatton. Photocontrol of protein folding: the interaction of photosensitive surfactants with bovine serum albumin. *Biochemistry*, 44(2):524–536, 2005. (Cited on pages 67, 68, and 73.)

[126] R. Levy. Peptide-capped gold nanoparticles: Towards artificial proteins. *ChemBioChem*, 7(8):1141–1145, 2006. (Cited on page 7.)

[127] R. Levy, N.T.K. Thanh, R.C. Doty, I. Hussain, R.J. Nichols, D.J. Schiffrin, M. Brust, and D.G. Fernig. Rational and combinatorial design of peptide capping ligands for gold nanoparticles. *Journal of the American Chemical Society*, 126(32):10076–10084, 2004. (Cited on page 7.)

[128] D. Li, A. Wieckowska, and I. Willner. Optical analysis of hg2+ ions by oligonucleotide–gold-nanoparticle hybrids and dna-based machines. *Angewandte Chemie*, 120(21):3991–3995, 2008. (Cited on pages 10, 45, and 69.)

[129] H. Li and L. Rothberg. Colorimetric detection of dna sequences based on electrostatic interactions with unmodified gold nanoparticles. *Proceedings of the National Academy of Sciences of the United States of America*, 101(39):14036, 2004. (Cited on page 10.)

[130] M. Li, S.K. Cushing, Q. Wang, X. Shi, L.A. Hornak, Z. Hong, and N. Wu. Size-dependent energy transfer between cdse/zns quantum dots and gold nanoparticles. *The Journal of Physical Chemistry Letters*, 2011. (Cited on pages 85 and 86.)

[131] D.R. Lide. *CRC handbook of chemistry and physics*. CRC Pr I Llc, 2003. (Cited on pages 1, 36, and 92.)

[132] D.M.J. Lilley. The ribosome functions as a ribozyme. *Chembiochem*, 2(1):31–35, 2001. (Cited on page 2.)

[133] MY Lin, R. Klein, HM Lindsay, DA Weitz, RC Ball, and P. Meakin. The structure of fractal colloidal aggregates of finite extent. *Journal of Colloid and Interface Science*, 137(1):263–280, 1990. (Cited on page 11.)

[134] S. Lindman, I. Lynch, E. Thulin, H. Nilsson, K.A. Dawson, and S. Linse. Systematic investigation of the thermodynamics of hsa adsorption to n-iso-propylacrylamide/n-tert-butylacrylamide copolymer nanoparticles. effects of particle size and hydrophobicity. *Nano letters*, 7(4):914–920, 2007. (Cited on page 69.)

[135] P. Lindner and T. Zemb. *Neutrons, X-rays, and light: scattering methods applied to soft condensed matter*. Elsevier North-Holland, 2002. ISBN 0444511229. (Cited on pages 26, 28, 34, 49, 50, 62, and 77.)

[136] S. Link and M.A. El-Sayed. Size and temperature dependence of the plasmon absorption of colloidal gold nanoparticles. *The Journal of Physical Chemistry B*, 103(21):4212–4217, 1999. (Cited on pages 20 and 21.)

[137] S. Link and M.A. El-Sayed. Shape and size dependence of radiative, non-radiative and photothermal properties of gold nanocrystals. *International Reviews in Physical Chemistry*, 19(3):409–454, 2000. (Cited on pages 5 and 19.)

[138] S. Linse, C. Cabaleiro-Lago, W.F. Xue, I. Lynch, S. Lindman, E. Thulin, S.E. Radford, and K.A. Dawson. Nucleation of protein fibrillation by nanoparticles. *Proceedings of the National Academy of Sciences*, 104(21):8691, 2007. (Cited on page 8.)

[139] W. Liu, M. Howarth, A.B. Greytak, Y. Zheng, D.G. Nocera, A.Y. Ting, and M.G. Bawendi. Compact biocompatible quantum dots functionalized for cellular imaging. *Journal of the American Chemical Society*, 130(4):1274–1284, 2008. (Cited on page 101.)

[140] X. Liu, M. Atwater, J. Wang, and Q. Huo. Extinction coefficient of gold nanoparticles with different sizes and different capping ligands. *Colloids and Surfaces B: Biointerfaces*, 58(1):3–7, 2007. (Cited on pages 22 and 92.)

[141] L.N. Loo, R.H. Guenther, V.R. Basnayake, S.A. Lommel, and S. Franzen. Controlled encapsidation of gold nanoparticles by a viral protein shell. *Journal of the American Chemical Society*, 128 (14):4502–4503, 2006. (Cited on page 70.)

[142] C.J. Loweth, W.B. Caldwell, X. Peng, A.P. Alivisatos, and P.G. Schultz. Dna-based assembly of gold nanocrystals. *Angewandte Chemie International Edition*, 38(12):1808–1812, 1999. (Cited on pages 70 and 76.)

[143] M. Lundqvist, J. Stigler, G. Elia, I. Lynch, T. Cedervall, and K.A. Dawson. Nanoparticle size and surface properties determine the protein corona with possible implications for biological impacts. *Proceedings of the National Academy of Sciences*, 105(38):14265, 2008. (Cited on pages 8 and 68.)

[144] I. Lynch and K.A. Dawson. Protein-nanoparticle interactions. *Nano Today*, 3(1-2):40–47, 2008. (Cited on pages 68 and 70.)

[145] R.J. Macfarlane, B. Lee, H.D. Hill, A.J. Senesi, S. Seifert, and C.A. Mirkin. Assembly and organization processes in dna-directed colloidal crystallization. *Proceedings of the National Academy of Sciences*, 106(26):10493, 2009. (Cited on page 40.)

[146] S.A. Maier. *Plasmonics: fundamentals and applications*. Springer Verlag, 2007. (Cited on pages xiv and 22.)

[147] BB Mandelbrot. *The fractal geometry of nature*. Wh Freeman, 1982. (Cited on pages 11, 12, and 32.)

[148] T. Maruyama, S. Katoh, M. Nakajima, H. Nabetani, T.P. Abbott, A. Shono, and K. Satoh. Ft-ir analysis of bsa fouled on ultrafiltration and microfiltration membranes. *Journal of Membrane Science*, 192(1-2):201–207, 2001. (Cited on pages 67 and 68.)

[149] MW Matsen. Phase behavior of block copolymer/homopolymer blends. *Macromolecules*, 28(17):5765–5773, 1995. (Cited on page 55.)

[150] P Meakin. Models for colloidal aggregation. *Annual Review of Physical Chemistry*, 39(1):237–267, 1988. (Cited on pages 12 and 32.)

[151] I.L. Medintz, H.T. Uyeda, E.R. Goldman, H. Mattoussi, et al. Quantum dot bioconjugates for imaging, labelling and sensing. *Nature Materials*, 4(6):435–446, 2005. (Cited on pages 3 and 4.)

[152] SVG Menon, C Manohar, and KS Rao. A new interpretation of the sticky hard sphere model. *The Journal of Chemical Physics*, 95: 9186, 1991. (Cited on pages 42, 57, and 77.)

[153] H.D.T. Mertens and D.I. Svergun. Structural characterization of proteins and complexes using small-angle X-ray solution scattering. *Journal of structural biology*, 172(1):128–141, 2010. ISSN 1047-8477. (Cited on pages 34, 35, 48, and 49.)

[154] M.A. Meyers, P.Y. Chen, A.Y.M. Lin, and Y. Seki. Biological materials: structure and mechanical properties. *Progress in Materials Science*, 53(1):1–206, 2008. (Cited on pages 2 and 45.)

[155] X. Michalet, FF Pinaud, LA Bentolila, JM Tsay, S. Doose, JJ Li, G. Sundaresan, AM Wu, SS Gambhir, and S. Weiss. Quantum dots for live cells, in vivo imaging, and diagnostics. *Science*, 307 (5709):538, 2005. (Cited on page 3.)

[156] G. Mie. Beitrage zur optik truber medien, speziell kolloidaler metallosungen. *Annalen der Physik*, 330(3):377–445, 1908. (Cited on page 5.)

[157] J.E. Millstone, S. Park, K.L. Shuford, L. Qin, G.C. Schatz, and C.A. Mirkin. Observation of a quadrupole plasmon mode for a colloidal solution of gold nanoprisms. *Journal of the American Chemical Society*, 127(15):5312–5313, 2005. (Cited on page 11.)

[158] Y. Min, M. Akbulut, K. Kristiansen, Y. Golan, and J. Israelachvili. The role of interparticle and external forces in nanoparticle assembly. *Nature Materials*, 7(7):527–538, 2008. (Cited on page 6.)

[159] C. Minelli, S. B. Lowe, and M. M. Stevens. Engineering nanocomposite materials for cancer therapy. *SMALL*, 6(21):2336–2357, 2010. (Cited on pages 3, 6, and 45.)

[160] C Mirkin, R Letsinger, R Mucic, and J Storhoff. A dna-based method for rationally assembling nanoparticles into macroscopic materials. *Nature*, 1996. (Cited on pages 6, 7, and 45.)

[161] AM Moulin, SJ O'Shea, RA Badley, P. Doyle, and ME Welland. Measuring surface-induced conformational changes in proteins. *Langmuir*, 15(26):8776–8779, 1999. (Cited on pages 67 and 68.)

[162] A Muratov, A MoussaÔd, T Narayanan, and EI Kats. A percusñyevick description of the microstructure of short-range interacting metastable colloidal suspensions. *The Journal of Chemical Physics*, 131:054902, 2009. (Cited on pages 42 and 57.)

[163] K. Murayama and M. Tomida. Heat-induced secondary structure and conformation change of bovine serum albumin investigated by fourier transform infrared spectroscopy. *Biochemistry*, 43(36): 11526–11532, 2004. (Cited on page 70.)

[164] CB Murray, CR Kagan, and MG Bawendi. Synthesis and characterization of monodisperse nanocrystals and close-packed nanocrystal assemblies. *Annual Review of Materials Science*, 30(1):545–610, 2000. (Cited on page 84.)

[165] K. Nakanishi, T. Sakiyama, and K. Imamura. On the adsorption of proteins on solid surfaces, a common but very complicated phenomenon. *Journal of bioscience and bioengineering*, 91(3):233–244, 2001. (Cited on page 8.)

[166] A.E. Nel, L. M
"adler, D. Velegol, T. Xia, E.M.V. Hoek, P. Somasundaran, F. Klaessig, V. Castranova, and M. Thompson. Understanding biophysicochemical interactions at the nano–bio interface. *Nature Materials*, 8(7):543–557, 2009. (Cited on page 7.)

[167] Z. Nie, A. Petukhova, and E. Kumacheva. Properties and emerging applications of self-assembled structures made from inorganic nanoparticles. *Nature Nanotechnology*, 5(1):15–25, 2009. (Cited on page 6.)

[168] B. Nikoobakht and M.A. El-Sayed. Preparation and growth mechanism of gold nanorods (nrs) using seed-mediated growth method. *Chemistry of Materials*, 15(10):1957–1962, 2003. (Cited on page 11.)

[169] W. Niu, S. Zheng, D. Wang, X. Liu, H. Li, S. Han, J. Chen, Z. Tang, and G. Xu. Selective synthesis of single-crystalline rhombic dodecahedral, octahedral, and cubic gold nanocrystals. *Journal of the American Chemical Society*, 131(2):697–703, 2008. (Cited on page 11.)

[170] W. Norde. Adsorption of proteins from solution at the solid-liquid interface. *Advances in colloid and interface science*, 25:267–340, 1986. (Cited on page 67.)

[171] W. Norde. My voyage of discovery to proteins in flatland... and beyond. *Colloids and surfaces. B, Biointerfaces*, 61(1):1, 2008. (Cited on page 67.)

[172] W. Norde and C.E. Giacomelli. Bsa structural changes during homomolecular exchange between the adsorbed and the dissolved states. *Journal of biotechnology*, 79(3):259–268, 2000. (Cited on page 69.)

[173] J.P. Novak, C. Nickerson, S. Franzen, and D.L. Feldheim. Purification of molecularly bridged metal nanoparticle arrays by centrifugation and size exclusion chromatography. *Analytical chemistry*, 73(23):5758–5761, 2001. (Cited on page 70.)

[174] D Nykypanchuk, MM Maye, D van der Lelie, and O Gang. Dna-guided crystallization of colloidal nanoparticles. *Nature*, 451 (7178):549–552, 2008. (Cited on pages 12, 40, 54, 55, and 56.)

[175] J. Oishi, Y. Asami, T. Mori, J.H. Kang, T. Niidome, and Y. Katayama. Colorimetric enzymatic activity assay based on noncrosslinking aggregation of gold nanoparticles induced by adsorption of substrate peptides. *Biomacromolecules*, 9(9):2301–2308, 2008. (Cited on pages 23 and 75.)

[176] J.R. Olivieril and A.F. Craievich. The subdomain structure of human serum albumin in solution under different ph conditions studied by small angle x-ray scattering. *European biophysics journal*, 24(2):77–84, 1995. (Cited on page 72.)

[177] G.F. Paciotti, L. Myer, D. Weinreich, D. Goia, N. Pavel, R.E. McLaughlin, and L. Tamarkin. Colloidal gold: a novel nanoparticle vector for tumor directed drug delivery. *Drug delivery*, 11(3): 169–183, 2004. (Cited on page 67.)

[178] SJ Park, AA Lazarides, JJ Storhoff, L Pesce, and CA Mirkin. The structural characterization of oligonucleotide-modified gold nanoparticle networks formed by dna hybridization. *J. Phys. Chem. B*, 108(33):12375–12380, 2004. (Cited on pages 9 and 12.)

[179] SY Park, JS Lee, D Georganopoulou, CA Mirkin, and GC Schatz. Structures of dna-linked nanoparticle aggregates. *J. Phys. Chem. B*, 110(25):12673–12681, 2006. (Cited on pages 6, 12, 22, 23, 32, 33, 51, 53, 56, and 59.)

[180] SY Park, AKR Lytton-Jean, B Lee, S Weigand, GC Schatz, and CA Mirkin. Dna-programmable nanoparticle crystallization. *Nature*, 451(7178):553–556, 2008. (Cited on pages 11, 12, 45, 54, 56, and 75.)

[181] I.P. Parkin and R.G. Palgrave. Self-cleaning coatings. *J. Mater. Chem.*, 15(17):1689–1695, 2004. (Cited on page 1.)

[182] K. Pechstedt, T. Whittle, J. Baumberg, and T. Melvin. Photoluminescence of colloidal cdse/zns quantum dots: The critical effect of water molecules. *The Journal of Physical Chemistry C*. (Cited on pages 85 and 103.)

[183] X. Peng. An essay on synthetic chemistry of colloidal nanocrystals. *Nano Research*, 2(6):425–447, 2009. (Cited on page 86.)

[184] BNJ Persson. Polarizability of small spherical metal particles: influence of the matrix environment. *Surface science*, 281(1-2): 153–162, 1993. (Cited on page 20.)

[185] BNJ Persson and ND Lang. Electron-hole-pair quenching of excited states near a metal. *Physical Review B*, 26:5409–5415, 1982. (Cited on page 85.)

[186] T. Peters Jr. Serum albumin: recent progress in the understanding of its structure and biosynthesis. *Clinical Chemistry*, 23(1):5, 1977. (Cited on pages 67 and 68.)

[187] T. Peters Jr. Serum albumin. *Adv Protein Chem*, 37(161):60065–0, 1985. (Cited on pages 68 and 73.)

[188] M.P. Pileni. Self-assembly of inorganic nanocrystals: Fabrication and collective intrinsic properties. *Accounts of chemical research*, 40(8):685–693, 2007. (Cited on page 6.)

[189] T. Pons, I.L. Medintz, K.E. Sapsford, S. Higashiya, A.F. Grimes, S. Doug, and H. Mattoussi. On the quenching of semiconductor quantum dot photoluminescence by proximal gold nanoparticles. *Nano letters*, 7(10):3157–3164, 2007. (Cited on pages 83, 84, and 85.)

[190] F. Porta, G. Speranza, Z. Krpetic, V. Dal Santo, P. Francescato, and G. Scari. Gold nanoparticles capped by peptides. *Materials Science and Engineering: B*, 140(3):187–194, 2007. (Cited on page 70.)

[191] D.E. Prasuhn, J.R. Deschamps, K. Susumu, M.H. Stewart, K. Boeneman, J.B. Blanco-Canosa, P.E. Dawson, and I.L. Medintz. Polyvalent display and packing of peptides and proteins on semiconductor quantum dots: Predicted versus experimental results. *Small*, 6 (4):555–564, 2010. (Cited on page 101.)

[192] FW Putnam. The plasma proteins. vol. 2., 1975. (Cited on page 68.)

[193] R.G. Reed, R.C. Feldhoff, OL Clute, and T. Peters Jr. Fragments of bovine serum albumin produced by limited proteolysis. conformation and ligand binding. *Biochemistry*, 14(21):4578–4583, 1975. (Cited on pages 67 and 68.)

[194] C. Regnaut and JC Ravey. Application of the adhesive sphere model to the structure of colloidal suspensions. *The Journal of Chemical Physics*, 91:1211, 1989. (Cited on pages 42 and 57.)

[195] M. Reismann, J.C. Bretschneider, G. Plessen, and U. Simon. Reversible photothermal melting of dna in dna–gold-nanoparticle networks. *Small*, 4(5):607–610, 2008. (Cited on page 11.)

[196] U. Resch-Genger, M. Grabolle, S. Cavaliere-Jaricot, R. Nitschke, and T. Nann. Quantum dots versus organic dyes as fluorescent labels. *Nature Methods*, 5(9):763–775, 2008. (Cited on pages 4, 13, and 83.)

[197] T. Rieker, A. Hanprasopwattana, A. Datye, and P. Hubbard. Particle size distribution inferred from small-angle x-ray scattering and transmission electron microscopy. *Langmuir*, 15(2):638–641, 1999. (Cited on page 26.)

[198] P. Roach, D. Farrar, and C.C. Perry. Surface tailoring for controlled protein adsorption: effect of topography at the nanometer scale and chemistry. *Journal of the American Chemical Society*, 128(12): 3939–3945, 2006. (Cited on page 69.)

[199] C Robertus, WH Philipse, JGH Joosten, and YK Levine. Solution of the percusñyevick approximation of the multicomponent adhesive spheres system applied to the small angle x ray scattering from microemulsions. *The Journal of Chemical Physics*, 90:4482, 1989. (Cited on pages 42 and 57.)

[200] S.M. Rodems, B.D. Hamman, C. Lin, J. Zhao, S. Shah, D. Heidary, L. Makings, J.H. Stack, and B.A. Pollok. A fret-based assay platform for ultra-high density drug screening of protein kinases and phosphatases. *ASSAY and Drug Development Technologies*, 1 (1):9–19, 2002. (Cited on pages 4 and 85.)

[201] A.T. Rodriguez, M. Chen, Z. Chen, C.J. Brinker, and H. Fan. Nanoporous carbon nanotubes synthesized through confined hydrogen-bonding self-assembly. *Journal of the American Chemical Society*, 128(29):9276–9277, 2006. (Cited on page 6.)

[202] N.L. Rosi and C.A. Mirkin. Nanostructures in biodiagnostics. *Chem. Rev*, 105(4):1547–1562, 2005. (Cited on pages 6 and 45.)

[203] M.G. Ryadnov, B. Ceyhan, C.M. Niemeyer, and D.N. Woolfson. "Belt and Braces": A Peptide-Based Linker System of de Novo Design. *J. Am. Chem. Soc*, 125(31):9388–9394, 2003. (Cited on page 45.)

[204] S.F. Santos, D. Zanette, H. Fischer, and R. Itri. A systematic study of bovine serum albumin (bsa) and sodium dodecyl sulfate (sds) interactions by surface tension and small angle x-ray scattering. *Journal of colloid and interface science*, 262(2):400–408, 2003. (Cited on page 72.)

[205] K.E. Sapsford, L. Berti, and I.L. Medintz. Materials for fluorescence resonance energy transfer analysis: beyond traditional donor-acceptor combinations. *Angewandte Chemie International Edition*, 45(28):4562–4589, 2006. (Cited on page 4.)

[206] K.E. Sapsford, T. Pons, I.L. Medintz, S. Higashiya, F.M. Brunel, P.E. Dawson, and H. Mattoussi. Kinetics of metal-affinity driven self-assembly between proteins or peptides and cdse-zns quantum dots. *The Journal of Physical Chemistry C*, 111(31):11528–11538, 2007. (Cited on pages 4, 88, and 104.)

[207] M. Sastry, A. Gole, and V. Patil. Lamellar langmuir-blodgett films of hydrophobized colloidal gold nanoparticles by organization at the air-water interface. *Thin Solid Films*, 384(1):125–131, 2001. (Cited on page 7.)

[208] M.L. Sauthier, R.L. Carroll, C.B. Gorman, and S. Franzen. Nanoparticle layers assembled through dna hybridization: characterization and optimization. *Langmuir*, 18(5):1825–1830, 2002. (Cited on page 70.)

[209] DW Schaefer, JE Martin, P Wiltzius, and DS Cannell. Fractal geometry of colloidal aggregates. *Physical Review Letters*, 52(26): 2371–2374, 1984. (Cited on pages 12 and 32.)

[210] G. Schmid and A. Lehnert. The complexation of gold colloids. *Angewandte Chemie International Edition in English*, 28(6):780–781, 1989. (Cited on page 70.)

[211] G. Schmid, V. Maihack, F. Lantermann, and S. Peschel. Ligand-stabilized metal clusters and colloids: properties and applications. *J. Chem. Soc., Dalton Trans.*, (5):589–595, 1996. (Cited on page 70.)

[212] J.P. Schneider, D.J. Pochan, B. Ozbas, K. Rajagopal, L. Pakstis, and J. Kretsinger. Responsive hydrogels from the intramolecular folding and self-assembly of a designed peptide. *Journal of the American Chemical Society*, 124(50):15030–15037, 2002. (Cited on page 70.)

[213] P. Schwerdtfeger, H.L. Hermann, and H. Schmidbaur. Stability of the gold (i)-phosphine bond. a comparison with other group 11 elements. *Inorganic chemistry*, 42(4):1334–1342, 2003. (Cited on page 70.)

[214] Borja Sepulveda, Paula C. Angelome, Laura M. Lechuga, and Luis M. Liz-Marzan. LSPR-based nanobiosensors. *NANO TODAY*, 4(3):244–251, JUN 2009. ISSN 1748-0132. doi: {10.1016/j.nantod.2009.04.001}. (Cited on pages 3 and 45.)

[215] S.S. Shankar, A. Rai, B. Ankamwar, A. Singh, A. Ahmad, and M. Sastry. Biological synthesis of triangular gold nanoprisms. *Nature materials*, 3(7):482–488, 2004. (Cited on page 5.)

[216] J. J. Shi, A. R. Votruba, O. C. Farokhzad, and R. Langer. Nanotechnology in drug delivery and tissue engineering: From discovery to applications. *Nano letters*, 10(9):3223–3230, 2010. (Cited on page 45.)

[217] M.P. Singh and G.F. Strouse. Involvement of the lspr spectral overlap for energy transfer between a dye and au nanoparticle. *Journal of the American Chemical Society*, 2010. (Cited on page 70.)

[218] L. Song. Sorption of bovine serum albumin on nano and bulk oxide particles. *Masters Theses*, page 391, 2010. (Cited on page 67.)

[219] R.A. Sperling, P.R. Gil, F. Zhang, M. Zanella, and W.J. Parak. Biological applications of gold nanoparticles. *Chem. Soc. Rev.*, 37 (9):1896–1908, 2008. (Cited on page 6.)

[220] M.M. Stevens and J.H. George. Exploring and engineering the cell surface interface. *SCIENCE-NEW YORK THEN WASHINGTON-*, 5751:1135, 2005. ISSN 0036-8075. (Cited on page 45.)

[221] M.M. Stevens, N.T. Flynn, C. Wang, D.A. Tirrell, and R. Langer. Coiled-Coil Peptide-Based Assembly of Gold Nanoparticles. *Advanced Materials*, 16(11):915–918, 2004. ISSN 1521-4095. (Cited on page 45.)

[222] J Storhoff, A Lazarides, R Mucic, and C Mirkin. What controls the optical properties of dna-linked gold nanoparticle assemblies. *J. Am. Chem. Soc*, 2000. (Cited on pages 6, 22, 23, and 51.)

[223] MA Stuart, GJ Fleer, J. Lyklema, W. Norde, and JM Scheutjens. Adsorption of ions, polyelectrolytes and proteins. *Advances in colloid and interface science*, 34:477, 1991. (Cited on page 6.)

[224] Samuel I. Stupp. Self-assembly and biomaterials. *Nano letters*, 10 (12):4783–4786, 2010. (Cited on page 45.)

[225] S.F. Sun. *Physical chemistry of macromolecules*. Wiley Online Library, 1994. (Cited on page 18.)

[226] R.J. Sundberg and R.B. Martin. Interactions of histidine and other imidazole derivatives with transition metal ions in chemical and biological systems. *Chemical Reviews*, 74(4):471–517, 1974. (Cited on pages 88 and 104.)

[227] M. Swierczewska, S. Lee, and X. Chen. The design and application of fluorophore–gold nanoparticle activatable probes. *Phys. Chem. Chem. Phys.*, 2011. (Cited on page 84.)

[228] D.V. Talapin. Lego materials. *ACS nano*, 2(6):1097–1100, 2008. (Cited on page 11.)

[229] T. Tamaki, N. Miyoshi, T. Uehara, and Y. Ohya. Isolation of gold nanoparticle/oligo-dna conjugates by the number of oligo-dnas attached and their formation of self-assembly. *Chemistry Letters*, 39(10):1084–1085, 2010. (Cited on page 70.)

[230] R. Tantra, J. Tompkins, and P. Quincey. Characterisation of the de-agglomeration effects of bovine serum albumin on nanoparticles in aqueous suspension. *Colloids and Surfaces B: Biointerfaces*, 75(1): 275–281, 2010. (Cited on page 67.)

[231] T.A. Taton, C.A. Mirkin, and R.L. Letsinger. Scanometric dna array detection with nanoparticle probes. *Science*, 289(5485):1757, 2000. (Cited on page 6.)

[232] JH Teichroeb, JA Forrest, and LW Jones. Size-dependent denaturing kinetics of bovine serum albumin adsorbed onto gold nanospheres. *The European Physical Journal E: Soft Matter and Biological Physics*, 26(4):411–415, 2008. (Cited on page 70.)

[233] N.T.K. Thanh and Z. Rosenzweig. Development of an aggregation-based immunoassay for anti-protein a using gold nanoparticles. *Analytical chemistry*, 74(7):1624–1628, 2002. (Cited on page 9.)

[234] D.H. Tsai, F.W. DelRio, A.M. Keene, K.M. Tyner, R.I. MacCuspie, T.J. Cho, M.R. Zachariah, and V.A. Hackley. Adsorption and Conformation of Serum Albumin Protein on Gold Nanoparticles Investigated Using Dimensional Measurements and in Situ Spectroscopic Methods. *Langmuir*, pages 536–3674, 2011. ISSN 0743-7463. (Cited on pages 8, 16, 17, 67, 68, 73, and 100.)

[235] J. Turkevich, P.C. Stevenson, and J. Hillier. A study of the nucleation and growth processes in the synthesis of colloidal gold. *Discuss. Faraday Soc.*, 11:55–75, 1951. (Cited on pages 5 and 70.)

[236] M. Turner, V.B. Golovko, O.P.H. Vaughan, P. Abdulkin, A. Berenguer-Murcia, M.S. Tikhov, B.F.G. Johnson, and R.M. Lambert. Selective oxidation with dioxygen by gold nanoparticle catalysts derived from 55-atom clusters. *Nature*, 454(7207):981–983, 2008. (Cited on page 103.)

[237] W.G. van Sark, P.L.T.M. Frederix, D.J. Van den Heuvel, H.C. Gerritsen, A.A. Bol, J.N.J. van Lingen, C. de Mello Donega, and A. Meijerink. Photooxidation and photobleaching of single cdse/zns quantum dots probed by room-temperature time-resolved spectroscopy. *The Journal of Physical Chemistry B*, 105(35):8281–8284, 2001. (Cited on page 103.)

[238] R. Vavrin, J. Kohlbrecher, A. Wilk, M. Ratajczyk, MP Lettinga, J. Buitenhuis, and G. Meier. Structure and phase diagram of an adhesive colloidal dispersion under high pressure: A small angle neutron scattering, diffusing wave spectroscopy, and light scattering study. *The Journal of chemical physics*, 130:154903, 2009. (Cited on pages 42 and 57.)

[239] H. Wang and B.M. Reinhard. Monitoring simultaneous distance and orientation changes in discrete dimers of dna linked gold nanoparticles. *The Journal of Physical Chemistry C*, 113(26):11215–11222, 2009. (Cited on page 70.)

[240] J. Wang, L. Wang, X. Liu, Z. Liang, S. Song, W. Li, G. Li, and C. Fan. A gold nanoparticle-based aptamer target binding readout for atp assay. *Advanced Materials*, 19(22):3943–3946, 2007. (Cited on pages 10, 45, and 69.)

[241] L. Wang, X. Liu, X. Hu, S. Song, and C. Fan. Unmodified gold nanoparticles as a colorimetric probe for potassium dna aptamers. *Chemical communications*, (36):3780–3782, 2006. (Cited on pages 10, 45, and 69.)

[242] Q. Wang, H. Wang, C. Lin, J. Sharma, S. Zou, and Y. Liu. Photonic interaction between quantum dots and gold nanoparticles in discrete nanostructures through dna directed self-assembly. *Chem. Commun.*, 46(2):240–242, 2009. (Cited on page 9.)

[243] R.D. Waniska, J.K. Shetty, and J.E. Kinsella. Protein-stabilized emulsions: effects of modification on the emulsifying activity of bovine serum albumin in a model system. *Journal of Agricultural and Food Chemistry*, 29(4):826–831, 1981. (Cited on page 68.)

[244] M.J. Weber. *Handbook of optical materials*. CRC, 2003. (Cited on page 17.)

[245] K.M. Weigandt, D.C. Pozzo, and L. Porcar. Structure of high density fibrin networks probed with neutron scattering and rheology. *Soft Matter*, 5(21):4321–4330, 2009. (Cited on page 32.)

[246] DA Weitz, JS Huang, MY Lin, and J Sung. Limits of the fractal dimension for irreversible kinetic aggregation of gold colloids. *Physical Review Letters*, 54(13):1416–1419, 1985. (Cited on page 51.)

[247] K.A. Willets and R.P. Van Duyne. Localized surface plasmon resonance spectroscopy and sensing. *Annu. Rev. Phys. Chem.*, 58:267–297, 2007. (Cited on pages 5, 19, and 20.)

[248] SA Wise and RL Watters. Certificate of analysis, standard reference material 927d. *National Institutes of Standards and Technology*, pages 1–5, 2006. (Cited on page 67.)

[249] Z. Xia, Y. Xing, M.K. So, A.L. Koh, R. Sinclair, and J. Rao. Multiplex detection of protease activity with quantum dot nanosensors prepared by intein-mediated specific bioconjugation. *Analytical chemistry*, 80(22):8649–8655, 2008. (Cited on page 86.)

[250] B.C. Ye and B.C. Yin. Highly sensitive detection of mercury (ii) ions by fluorescence polarization enhanced by gold nanoparticles. *Angewandte Chemie International Edition*, 47(44):8386–8389, 2008. (Cited on pages 11 and 45.)

[251] H. Yin, J.S. Slusky, B.W. Berger, R.S. Walters, G. Vilaire, R.I. Litvinov, J.D. Lear, G.A. Caputo, J.S. Bennett, and W.F. DeGrado. Computational design of peptides that target transmembrane helices. *Science*, 315(5820):1817, 2007. (Cited on pages 9 and 46.)

[252] W.W. Yu, E. Chang, R. Drezek, and V.L. Colvin. Water-soluble quantum dots for biomedical applications. *Biochemical and biophysical research communications*, 348(3):781–786, 2006. (Cited on page 4.)

[253] F. Zhang, G.G. Long, P.R. Jemian, J. Ilavsky, V.T. Milam, and J.A. Lewis. Quantitative measurement of nanoparticle halo formation around colloidal microspheres in binary mixtures. *Langmuir*, 24 (13):6504–6508, 2008. (Cited on pages 95, 96, and 97.)

[254] G. Zhang, D. Wang, and H. M
"ohwald. Patterning microsphere surfaces by templating colloidal crystals. *Nano letters*, 5(1):143–146, 2005. (Cited on page 2.)

[255] W. Zhao, W. Chiuman, J.C.F. Lam, M.A. Brook, and Y. Li. Simple and rapid colorimetric enzyme sensing assays using non-crosslinking gold nanoparticle aggregation. *Chemical Communications*, (36):3729–3731, 2007. (Cited on pages 10 and 45.)

[256] W. Zhao, M.M. Ali, S.D. Aguirre, M.A. Brook, and Y. Li. Paper-based bioassays using gold nanoparticle colorimetric probes. *Analytical chemistry*, 80(22):8431–8437, 2008. (Cited on page 9.)

[257] W. Zhao, M.A. Brook, and Y. Li. Design of gold nanoparticle-based colorimetric biosensing assays. *ChemBioChem*, 9(15):2363–2371, 2008. (Cited on pages 69 and 75.)

[258] W. Zhao, J.C.F. Lam, W. Chiuman, M.A. Brook, and Y. Li. Enzymatic cleavage of nucleic acids on gold nanoparticles: a generic platform for facile colorimetric biosensors. *Small*, 4(6):810–816, 2008. (Cited on page 10.)

[259] M. Zhou and I. Ghosh. Quantum dots and peptides: A bright future together. *Peptide Science*, 88(3):325–339, 2007. (Cited on pages 4, 83, 88, and 104.)

DECLARATION

Put your declaration here.

London, 12th March 2012

Piotr Gryko